



Title	Semi-Analytic Approach to Galaxy Formation in the Hierarchical Clustering Scenario
Author(s)	Nagashima, Masahiro
Citation	大阪大学, 1999, 博士論文
Version Type	VoR
URL	https://doi.org/10.11501/3155130
rights	
Note	

The University of Osaka Institutional Knowledge Archive : OUKA

<https://ir.library.osaka-u.ac.jp/>

The University of Osaka

Semi-Analytic Approach to Galaxy Formations in a Hierarchical Clustering Scenario

Masahiro Nagashima

Department of Earth and Space Science, Graduate School of Science,
Osaka University, Toyonaka, Osaka 560-0043, Japan
Email: masa@vega.ess.sci.osaka-u.ac.jp

ACKNOWLEDGMENTS

I would like to thank Prof. N. Gouda for his valuable discussion and continuous encouragement. I also thank Prof. S. Ikeuchi, Prof. M. Sasaki, Prof. F. Takahara for their fruitful suggestions, and Mr. T. Yano and Mr. N. Sugiura for stimulated discussion, as collaborators. Moreover I would like to thank Dr. K. Okoshi, Dr. Y. Fujita, Dr. K. Miyahata, Prof. N. Arimoto, Prof. M. Umemura, Prof. M. Chiba, Dr. R. Nishi, Dr. H. Susa, Ms. Y. Tajiri, for valuable suggestions, and also thank Prof. N. Arimoto and Prof. S. Charlot for permitting me to use their spectral evolution codes. I am also very grateful to colleagues at my institute for advice and continuing encouragement. This work was supported in part by Research Fellowships of the Japan Society for the Promotion of Science for Young Scientists (No. 2265). The calculations were performed in part on VPP300/16R and VX/4R at the Astronomical Data Analysis Center of the National Astronomical Observatory, Japan.

ABSTRACT

The galaxy formation is one of the most important problems in astrophysics. Recent observations by the *Hubble Space Telescope* (HST) and the Keck telescope have revealed many aspects of galaxy formation and evolution. It is needed to construct a theoretical model for the galaxy formation which has the same quality as such observations.

In order to analyze the galaxy formation process, we first investigate the merging history of dark haloes in the *hierarchical clustering scenario*. We evaluate the effect of the spatial correlation of initial density fluctuations on the merging history of dark haloes. We find that mass functions obtained by the merging history models are affected by the spatial correlation.

Next, we apply a *semi-analytic model* of galaxy formation to two important problems on the galaxy formation, namely, the effect of photoionization by the UV background radiation and the colour-magnitude relation of elliptical galaxies in clusters of galaxies. The semi-analytic model includes some physical processes connected with the galaxy formation, such as merging histories of dark haloes, gas cooling, star formation, supernova feedback, mergers of galaxies, and so on. Therefore it is easier to investigate how the galaxy formation and evolution depend on these physical processes by using the semi-analytic model rather than N-body and hydrodynamical simulations. Since the galaxy formation process is very complicated, analysis by using the semi-analytic model is effective. We particularly investigate both the effect of the UV background on the luminosity function and the colour distribution of galaxies, and the effect of the supernova feedback and the UV background on the formation and evolution of elliptical galaxies.

When the UV background exists, the UV photons penetrate the galactic gas clouds and heat up the gas. So star formation is suppressed. We find that the number of faint galaxies decreases by the UV background. This result gives a possible way to solve the problem that the observed number of faint galaxies is smaller than that expected by theoretical models based on the hierarchical clustering scenario. We also find that the luminosity function becomes closer to the observational one, when we adopt an evolution model of intensity of the UV background, $J \propto (1+z)^\gamma$ with $\gamma = -1$ for $z \geq 2$ and $\gamma = 4$ for $z \leq 2$, where J is the intensity of the UV background. This model of the UV background evolution is suggested by observation.

To discuss the origin of the colour-magnitude relation of elliptical galaxies, we introduce a chemical evolution process model and an identification model of galactic morphologies. It is suggested by observation that the colour-magnitude relation reflects the metallicity-luminosity relation of galaxies, and that for reproducing the colour-magnitude relation it is important to suppress the chemical enrichment of stars in faint galaxies. For suppressing the chemical enrichment, we propose some solutions. One is assuming a strong supernova feedback. Another is introducing the effect of the UV background radiation. These solutions degenerate, but they

may be distinguished by studying other properties of galaxies, like the luminosity function, colour distribution, etc.

Contents

1	General introduction	1
2	The effect of spatial correlations on merger trees	9
2.1	INTRODUCTION	9
2.2	ANALYTIC APPROACH TO MASS FUNCTIONS	11
2.2.1	Press-Schechter formula	11
2.2.2	Jedamzik formula	12
2.3	MODELS OF MERGER TREES	13
2.3.1	Merging Cell model	13
2.3.2	Block model	15
2.3.3	Extension of the PS formalism	15
2.4	RESULTS	17
2.4.1	Mass spectrum	17
2.4.2	MCM cumulative multiplicity functions	17
2.4.3	Block model multiplicity functions	18
2.4.4	Overlapping effect	19
2.5	CONCLUSIONS & DISCUSSION	20
3	Semi-analytic model	31
3.1	INTRODUCTION	31
3.2	MERGING HISTORIES OF DARK HALOES	32
3.3	GAS COOLING	32
3.4	STAR FORMATION	34
3.5	SUPERNOVA FEEDBACK	35
3.6	MERGERS OF GALAXIES	35
3.7	STELLAR POPULATION SYNTHESIS AND IDENTIFICATION OF MOR- PHOLOGIES	36
4	Effects of the UV background radiation	39
4.1	INTRODUCTION	39
4.2	MODEL	40
4.2.1	Semi-analytic model	40
4.2.2	Photoionization and mass fraction of neutral core	41
4.2.3	UV background radiation	42

4.3	RESULTS	43
4.3.1	Luminosity function	43
4.3.2	Colour distribution at $z = 0$	45
4.3.3	Evolution of colour distributions	46
4.4	CONCLUSIONS AND DISCUSSION	46
5	Colour-magnitude relation	59
5.1	INTRODUCTION	59
5.2	MODEL	60
5.2.1	Merging history of dark haloes	60
5.2.2	Cooling, star formation, and feedback	61
5.2.3	Mergers of galaxies	61
5.2.4	Chemical evolution	61
5.3	RESULTS	61
5.3.1	Colour-magnitude relations	62
5.3.2	Evolution of mean stellar metallicity	63
5.4	DISCUSSION	64
5.4.1	Feedback and yield	64
5.4.2	Slope of colour-magnitude relation	65
5.4.3	Effect of the UV background radiation	66
5.4.4	Metal recycling	66
5.5	CONCLUSIONS	67
6	Summary and prospects	79
A	Effects of spatial correlations on mass function	83
A.1	THE PS FORMALISM	83
A.2	JEDAMZIK FORMALISM	85
A.3	SPATIAL CORRELATION	87
A.4	PEAK CONDITION	91
B	Mass function of block model	97
C	Formalism of mass function	101
C.1	CONDITIONAL PROBABILITY DISTRIBUTION FUNCTION	101
C.2	OVERLAPPING EFFECT	104

List of Figures

- 1.1 Schematic description of galaxy formation process in the hierarchical clustering scenario. The circles denote the dark haloes. The hatched circles mean that the baryonic gas in the dark haloes does not shrink because the radiative cooling is not effective. The symbols painted out with black show the galaxies. Since the evolution of the dark haloes is dominated by the gravity, the clustering continues throughout. The baryonic component, by contrast, the radiative cooling becomes effective when the density and temperature exceed a threshold, so that the gas loses the internal energy and shrink, then the density increases and stars are formed. 5
- 1.2 Cooling function from Sutherland & Dopita (1993). The solid and the dashed lines denote the cooling function of the primordial gas and that of the gas with solar abundance, respectively. 6
- 1.3 Cooling diagram. This figure is essentially the same as Fig.1 in Rees & Ostriker (1977). The solid line denotes the line on which $\tau_{cool} = \tau_{dyn}$ when τ_{cool} is estimated by the cooling function of primordial gas. The long-dashed line is the same as the solid line, but for solar abundance gas. If a halo collapses with a density and temperature below the lines, gas in the halo will lose the internal energy and forms a galaxy. The short-dashed straight lines are estimated from eq.(1.3) by the fixed Jeans mass. The Jeans masses are $10^9 M_\odot$, $10^{10} M_\odot$, $10^{11} M_\odot$, and $10^{12} M_\odot$, from left to right. 7
- 1.4 Example of merging paths of dark haloes. The halo finally formed has the mass M_0 at $z = z_0$. The branches denote the progenitors of the halo. The progenitors merge together at the ‘nodes’ of the branches. The mass of progenitors evolves by the mergers of progenitors and accretion of diffuse matter. 8
- 2.1 Scheme of averaging density fluctuations demonstrated in 2 dimensions (after Rodrigues & Thomas 1995). Lower grid represents i -th level. Upper grids represent $i + 1$ -th level with one of the overlapping grids displaced by half a block-length. The hatched region in the lower grid is averaged to make a block at the $i + 1$ -th level and indicated as the region marked as a thick square in the upper grid. Blocks in the offset grid are averaged from the lower level in the same way. 23

2.2	The overlapping criterion. The thick squares show haloes and the dashed squares show investigating regions. (a)The block can collapse and is merged into the halo because the overlapping region is larger than half of the lesser of the regions of the halo and the investigating region. (b)The block cannot collapse because the overlapping region is not larger than half of the lesser of the regions of the halo and the investigating region. (c)The linking criterion. In the case shown here, the block cannot collapse because we would like to prevent the growth of the long filamentary structure (see text). Note that it is equivalent to consider either regions or masses for the overlapping criterion.	24
2.3	Mass spectrum: (a)spectral index $n = 0$, (b) $n = -2$. The crosses show the standard deviations on each smoothing mass scale in the MCM. The solid lines show the scale-free spectra which are adopted to calculate the mass functions by using Jedamzik formalism.	25
2.4	Cumulative multiplicity function: (a)spectral index $n = 0$, (b) $n = -2$. The solid lines, the short-dashed lines, the dotted lines and the long-dashed lines show the cumulative multiplicity functions given by the MCM averaged over four realizations, the YNG formula, the PS formula and the Block model averaged over five realizations, respectively.	26
2.5	Block Model: (a) $n = 0$, (b) $n = -2$. Crosses, solid squares and open squares show the multiplicity functions averaged over five realizations of the Block model with the largest box size $M_0 = 10^5 M_*, 10^3 M_*$ and $10 M_*$ in the case of $n = 0$ and $10^7 M_*, 10^5 M_*$ and $10^3 M_*$ in the case of $n = -2$, respectively. The solid lines and the dotted lines show the predictions by using the Jedamzik formula and the PS formula, respectively.	27
2.6	The linking criterion. The thick squares show haloes and the dashed square shows an investigating region. We consider the case of $x = 1/4$. The investigating region can collapse in the case of $y = 1/2$, while it cannot collapse in the case of $y = 1/4$ because the investigating region has $1/4$ of its mass contained in <i>two</i> pre-existing haloes.	28
2.7	Effects of overlapping in the case of $y = 1/2$: (a) $n = 0$, (b) $n = -2$. The solid lines, dotted lines and long-dashed lines show the multiplicity functions averaged over four realizations given by the MCM with the overlapping criterion defined by $x = 1/2, 1/4$ and $1/8$, respectively. The short-dashed lines show the multiplicity functions given by the YNG formula.	29
2.8	Same as Fig.2.6, but for $y = x$	30
4.1	Mass fraction of neutral core. The horizontal axis shows the total mass including dark matter. The solid lines denote the ratio r_{UV}/r_{cool} in the case of $J_{-21} = 0.1$ at $z = 5, 4, 3, 2, 1$ and 0 from upper to lower, respectively. Note that the curve at $z = 0$ is almost the same as the horizontal axis. The dash-dotted line and the dashed line show the ratio in the case of $J_{-21} = 0.01$ and 1 at $z = 2$, respectively.	48

4.2	Evolution of UV background intensity. The thick lines and the thin lines denote the strong condition and the weak condition, respectively. The dotted lines, the short-dashed lines, and the long-dashed lines show cases (2) UV radiation exists in $0 \leq z \leq 5$, (3) $2 \leq z \leq 5$, and (4) $J \propto (1+z)^\gamma$, $\gamma = 4$ for $z \leq 2$ and $\gamma = -1$ for $z \geq 2$	49
4.3	(a) B-band luminosity functions. (b) K-band luminosity functions. The solid lines, the dotted lines, the short-dashed lines, and the long-dashed lines show cases (1) no UV, (2) UV radiation exists in $0 \leq z \leq 5$, (3) $2 \leq z \leq 5$, and (4) $J \propto (1+z)^\gamma$, $\gamma = 4$ for $z \leq 2$ and $\gamma = -1$ for $z \geq 2$. In all cases the weak condition is used. The filled circles with errorbars denote the luminosity functions from (a) Loveday et al. (1992) and (b) Mobasher et al. (1993).	50
4.4	B-band luminosity functions in galaxies' rest frame at various redshifts. (a) $z=0$, (b) $z=0.4$, (c) $z=1$, and (d) $z=2$. The types of lines are the same as Figs.4.3. In all cases the weak condition is used.	51
4.5	Same as Figs.4.3, but for the strong condition.	52
4.6	Same as Figs.4.4, but for the strong condition.	53
4.7	Colour distributions in the weak condition. The solid lines, the dotted lines, the short-dashed lines, and the long-dashed lines show cases (1) no UV, (2) UV radiation exists in $0 \leq z \leq 5$, (3) $2 \leq z \leq 5$, and (4) $J \propto (1+z)^\gamma$, $\gamma = 4$ for $z \leq 2$ and $\gamma = -1$ for $z \geq 2$. The histograms of the dash-dotted lines are from Mobasher et al.(1986), which are divided by the total number of galaxies. . . .	54
4.8	Same as Figs.4.7, but for the strong condition.	55
4.9	Colour distributions at various redshifts in galaxies' rest frame. (a) Colour distributions of galaxies selected by $-19.5 \leq M_B \leq -17$. (b) Colour distributions of galaxies selected by $M_B \leq -19.5$. The solid lines, the dotted lines, the short-dashed lines, and the long-dashed lines denote the distributions at $z = 0, 0.4, 1$, and 2 , respectively. The thin lines and the thick lines show cases (1) no UV, and (4) continuously evolved UV intensity. In all cases the weak condition is used. .	56
4.10	Same as Figs.4.9, but for the strong condition.	57
5.1	Schematic description of gas and metal recycling in star formation. f is a fraction of ejected mass from evolved stars into hot gas directly.	69
5.2	Colour-magnitude diagram of model A and B. (a) M_V v.s. $U - V$ in the model A. (b) Same as (a), but for the model B. (c) M_V v.s. $U - V$ in the model A. (d) Same as (c), but for the model B. The models are characterized in Table 1. The open circles denote galaxies identified as ellipticals. The solid lines show the observed CMRs (Bower et al. 1992).	70
5.3	Same as Fig.5.2, but for model C and D.	71
5.4	Upper panels: age-magnitude diagram. (a) Model A. (b) Model B. Lower panels: metallicity-magnitude diagram. (c) Model A. (d) Model B. The open circles denote elliptical galaxies.	72
5.5	Same as Fig.5.4, but for model C and D.	73

5.6	Evolution of mass-weighted mean stellar metallicity. Each symbol shows the mean metallicity of a progenitor at the time. The open circles denote progenitors in the <i>elliptical state</i> , and the dots the <i>spiral state</i> . These states are defined in the text. (a) A luminous elliptical in model A. $M_V = -24.1, U - V = 1.49, V - K = 3.12$. (b) A luminous elliptical in model B. $M_V = -23.9, U - V = 1.61, V - K = 3.23$. (c) A faint elliptical in model A. $M_V = -19.8, U - V = 1.02, V - K = 2.82$. (d) A faint elliptical in model B. $M_V = -20.5, U - V = 1.14, V - K = 3.10$. . .	74
5.7	Same as Fig.5.6, but for model C and D. (a) $M_V = -24.4, U - V = 1.51, V - K = 3.15$ in model C. (b) $M_V = -24.0, U - V = 1.62, V - K = 3.24$ in model D. (c) $M_V = -19.9, U - V = 0.90, V - K = 2.66$ in model C. (d) $M_V = -20.4, U - V = 1.39, V - K = 3.18$	75
5.8	Same as Fig.5.2, but for model E and F. Both models have a short star formation timescale, $\tau_*^0 = 2$ Gyr. Model E: $V_{hot} = 600$ km s ⁻¹ . Model F: $V_{hot} = 100$ km s ⁻¹ . . .	76
5.9	Same as Fig.5.2, but for model G and H. The effect of the UV background radiation is considered. Both models have a short star formation timescale, $\tau_*^0 = 2$ Gyr. Model G: $V_{hot} = 280$ km s ⁻¹ . Model H: $V_{hot} = 100$ km s ⁻¹	77
A.1	The normalized mass function, which is estimated numerically including the effect of the spatial correlation, is shown by the solid line in the case of the power index $n = 0$. Dotted line represents the PS mass function.	92
A.2	Same as Fig.A.1, but for $n = -2$	93
A.3	The normalized mass function, which is estimated numerically by taking into account the additional necessary condition that <i>isolated</i> objects should have maximum peak density, is shown by the solid line in the case of the power index $n = 0$. Dotted line represents the PS mass function.	94
A.4	Same as Fig.A.3, but for $n = -2$	95

List of Tables

5.1	Parameters for models.	62
-----	--------------------------------	----

Chapter 1

General introduction

Recent observations by the *Hubble Space Telescope* (HST) and the Keck telescope have rapidly increased the number of available observational data of faint, high redshift galaxies, providing us with significant new information about the birth and evolution of galaxies. In order to take full advantage of these data, it is very important to understand theoretically the physical processes underlying galaxy formation.

In the standard picture, it is considered that dark matter dominates in our Universe and that galaxies and clusters of galaxies have formed by the gravitational growth of small initial density fluctuations. It is usually considered that the initial density fluctuation is originated by classicalization of quantum fluctuations in the epoch of inflation, and the statistical properties of the fluctuation are described by a random Gaussian distribution (e.g., Peebles 1993). The fluctuations of dark matter have collapsed and virialised through self-gravitational instability into objects which are called ‘dark matter haloes’ or ‘dark haloes’. Larger haloes are generally considered to have formed hierarchically by clustering of smaller haloes (so called ‘hierarchical clustering’).

When the mass of the baryonic gas contained in such dark haloes exceeds the Jeans mass (Jeans 1922), the baryonic gas also collapses and virialises following the collapse of the dark matter. Furthermore, in the process of galaxy formation, baryonic gas must dissipate the internal energy by radiative cooling and shrink because galaxies are much denser systems than the virialised dark haloes and stars must be formed inside the cold and dense gaseous systems. In analyzing the formation and evolution of the galaxies, we must treat various physical processes over a large dynamic range from $\sim 1 - 10^2 M_\odot$ (star formation, heating processes of gases from supernovae, dynamical and chemical evolution of gases, etc.) through $\sim 10^6 - 10^{12} M_\odot$ (mergers of galaxies, tidal interactions, etc.) to $\sim 10^{13} - 10^{16} M_\odot$ (clusters of galaxies, large-scale structure of the Universe, etc.). So it is difficult to attack the problem of formation and evolution of galaxies in a way that connects all the above complicated physical processes (Fig.1.1).

The pioneering work on the galaxy formation is, for example, Rees & Ostriker (1977) and White & Rees (1978). Rees & Ostriker remarked upon the importance of the dissipational process of baryonic gases through radiative cooling. They considered that galaxies can be formed when the cooling timescale τ_{cool} of the proto-galactic clouds is shorter than the dynamical

timescale τ_{dyn} of the clouds, because such clouds lose the internal energy rapidly, shrink and become dense enough to form stars. The cooling timescale and the dynamical timescale are expressed as

$$\tau_{cool} \simeq \frac{3kT}{n\Lambda(T)}, \quad (1.1)$$

$$\tau_{dyn} \simeq (24\pi G\rho)^{-1/2}, \quad (1.2)$$

where T is the temperature of the gas, ρ and n are the density and the number density of the gas, and $\Lambda(t)$ is a cooling function. Examples of the cooling function are shown in Fig.1.2 (Sutherland & Dopita 1993). When we consider the Jeans mass scale M_J , at which the pressure gradient of gas is equal to the self-gravity, it is represented by using both the temperature and the number density of gas in the cloud as

$$M_J \simeq \left(\frac{\pi k}{Gm_p\mu} \right)^{3/2} T^{3/2} \rho^{-1/2} \simeq 10^8 \left(\frac{T}{10^4 K} \right) n^{-1/2} M_\odot. \quad (1.3)$$

In Fig.1.3, the solid and dashed thick lines show the lines in which $\tau_{cool} = \tau_{dyn}$ for the primordial gas and the solar abundance gas, respectively. The thin dashed lines are obtained by eq.(1.3). Rees & Ostriker considered that the characteristic scale of galaxies is between $10^9 \lesssim (M/M_\odot) \lesssim 10^{12}$.

In order to discuss the statistical properties of galaxies such as the luminosity function, the above discussion must be connected with the mass function of haloes. White & Rees (1978) calculated the luminosity function of galaxies by using the Press-Schechter formula (Press & Schechter 1974; hereafter PS, *see* Appendix A) in which the mass function of dark haloes is estimated analytically. However, the status of gaseous systems and the formations of stars in each dark halo depend on the thermal history of the gaseous systems, merging of the galaxies and the merging history of the halo. So it is very important to know the merging history of each dark halo in order to evaluate the status of the gaseous systems and the formation rate of stars in the halo.

White & Frenk (1991) extended this approach to consider the *merging process* of dark haloes approximately by using an extended PS formula (Bower 1991). In this formula they take into account the probability of finding a region with mass M_1 at redshift z_1 under the condition that the region with M_1 is included in a region with mass M_0 at z_0 ($M_0 > M_1$ and $z_0 < z_1$). The extension of the PS formula is also discussed by Lacey & Cole (1993). By using the peak formula (Peacock & Heavens 1985, Bardeen et al. 1986; hereafter BBKS), Lacey & Silk (1991, 1993) also investigate the time scale of the collapse of galaxy groups after the galaxies have collapsed on the assumption that the mass ratio of groups to galaxies is constant.

After White & Frenk (1991), an approach to solving galaxy formation, namely, a semi-analytic approach is making progress as follows. In order to realize the various merging paths of galaxies, models based on the Monte Carlo method has been developed (e.g., Kauffmann, White & Guiderdoni 1993; Cole et al. 1994; Roukema et al. 1997; Somerville & Primack 1998). Their method is basically as follows (see Fig.1.1). First, the merging paths of dark haloes are realized by either the extension of the PS formalism or the block model. An example of the merging paths is shown in Fig.1.4. These paths are determined only by properties of the initial

density fluctuations in principle, but actually depend on models, e.g., the spherically symmetric collapse approximation. Note that the halo merging paths form paths of the gravitational potential wells. Next, in each step of a merging path, that is, in each gravitational potential well, evolutions of the baryonic component, namely, gas cooling, star formation, and supernova feedback, are calculated. We recognize a system consisting of the stars and cooled gas as a *galaxy*. The baryonic gas always cools when we consider only gas clouds larger than the Jeans mass, so all collapsed haloes have at least one galaxy. When two or more dark haloes merge together, there is a possibility that galaxies contained in progenitor haloes merge together. The judgment whether the galaxies merge together or not is usually determined by the dynamical friction timescale. Here we define the *lifetime* of haloes as the elapsed time between the formation time of the halo and the time at which the halo is subsumed into a larger halo. If the dynamical friction timescale is shorter than the lifetime, the galaxies will merge. If not, the galaxies will not merge and the common dark halo has two or more galaxies. This system is recognized as a group or cluster of galaxies. Moreover, we can see the colour and luminosity of each galaxy because we know the star formation history of each galaxy if we include a stellar population synthesis model. Through the above procedure, we know the properties of each galaxy, and the statistical properties like luminosity function, colour distribution, and so on. These processes are reviewed in Chapter 3. The studies in Chapters 4 and 5 are based on the model described in Chapter 3.

In contrast to the semi-analytic approach, there are approaches by N-body and hydrodynamical simulations. These solve numerically gravitational force and hydrodynamical equations. Therefore we need these simulations for quantitative analyses. However, we have a resolution limit in the restricted computer power, so the validity of the results obtained by such simulations should be investigated carefully (e.g., Kang et al. 1994). Moreover, since all calculations are performed by computers, it is difficult for us to see the complicated physical processes. In the semi-analytic model, in contrast, it is easy to understand the galaxy formation process because it includes the physical processes mentioned above, that is, star formation, feedback, and so on. Moreover, some approximated models, say, star formation, must be introduced even in the N-body/hydrodynamical simulations for the restricted computer power. We spend much less computer power for the semi-analytic model compared to such N-body/hydrodynamical simulations because the semi-analytic model includes the physical processes with the *analytic* form. Therefore the semi-analytic model is effective especially when a parameter space is vast for the process of galaxy formations because of many unknown physical processes. Thus the semi-analytic approach should be developed complementarily to the N-body/hydrodynamical simulations.

Many aspects of galaxies have been revealed by several authors through the semi-analytic models. They have succeeded in reproducing some observational results, at least qualitatively, like the luminosity function, colour distribution, Tully-Fisher relation, cold gas content as a function of luminosity, trends of galaxy colour with morphology, and so on. We believe, however, the most important contribution in the studies of galaxy formation by using the semi-analytic models is to reveal relationships between such observational quantities and physical processes such as star formation and supernova feedback. Maybe we can say that the semi-analytic models have firstly enabled us to investigate the relationships by comparing the calculations with the observations directly.

The aim of this thesis is to study the galaxy formation process in the context of the hierarchical clustering scenario. Therefore we investigate how the galaxy formation and evolution depend on these physical processes. We apply the semi-analytic model to two topics. The first is the effect of the UV background radiation on the luminosity function and the colour distribution of galaxies. In spite of many suggestions about the importance of the effect of the UV background by many authors (e.g., Dekel & Rees 1987), it has not been considered in the semi-analytic model. Therefore it is worthwhile to investigate the effect of the UV background by using the semi-analytic model.

The second topic is the origin of the colour-magnitude relation of elliptical galaxies in clusters of galaxies. It is considered that this relation is an important clue for understanding the galaxy formation. The traditional scenario of the formation of elliptical galaxies is that a monolithic protogalactic cloud collapses and then forms stars for a short timescale until blowing the galactic wind. This model of the formation of ellipticals is not based on the hierarchical clustering scenario. Recent development of the semi-analytic model enables us to analyze the origin of the colour-magnitude relation in the hierarchical clustering scenario. Then Kauffmann & Charlot (1997) investigate this relation by using their semi-analytic model, but their analysis is inadequate for understanding physical mechanisms forming the relation. Therefore we reanalyze the physical origin of this relation by using the semi-analytic model.

In this thesis, we consider only the standard CDM model as the cosmological model. Rather than the standard CDM model, recent observations suggest that the Universe has either a negative curvature or a non-zero cosmological constant. However, fixing the cosmological model, we investigate the dependence of observational quantities of galaxies on the baryonic processes such as cooling, star formation, supernova feedback, and so on. The standard CDM model is characterized as follows. The density parameter and the cosmological constant are $\Omega_0 = 1$ and $\Lambda_0 = 0$, respectively (the Einstein-de Sitter universe). The Hubble parameter h equals 0.5 ($H_0 \equiv 100h \text{ km s}^{-1} \text{ Mpc}^{-1}$). The cosmic scale factor $a(t)$ is proportional to $t^{2/3}$, where t is the time. The density contrast at a position \mathbf{x} , $\delta(\mathbf{x}) \equiv \frac{\rho(\mathbf{x}) - \bar{\rho}}{\bar{\rho}}$, $\bar{\rho}$ is the cosmic mean density) evolves as $\delta \propto a$ in the linear regime, $\delta \ll 1$.

In Chapter 2, the merging history of dark haloes is examined, because it is the foundation in the semi-analytic model. Especially, taking notice of the spatial correlation of the density fluctuations, the validity of the PS formalism and the block model is investigated. In Chapter 3, the semi-analytic model is reviewed. In Chapter 4, we discuss the possible effect of the UV background radiation on galaxy formation by using the semi-analytic model. In Chapter 5, we investigate the colour-magnitude relation of elliptical galaxies in clusters of galaxies. Chapter 6 is devoted to conclusions and prospects.

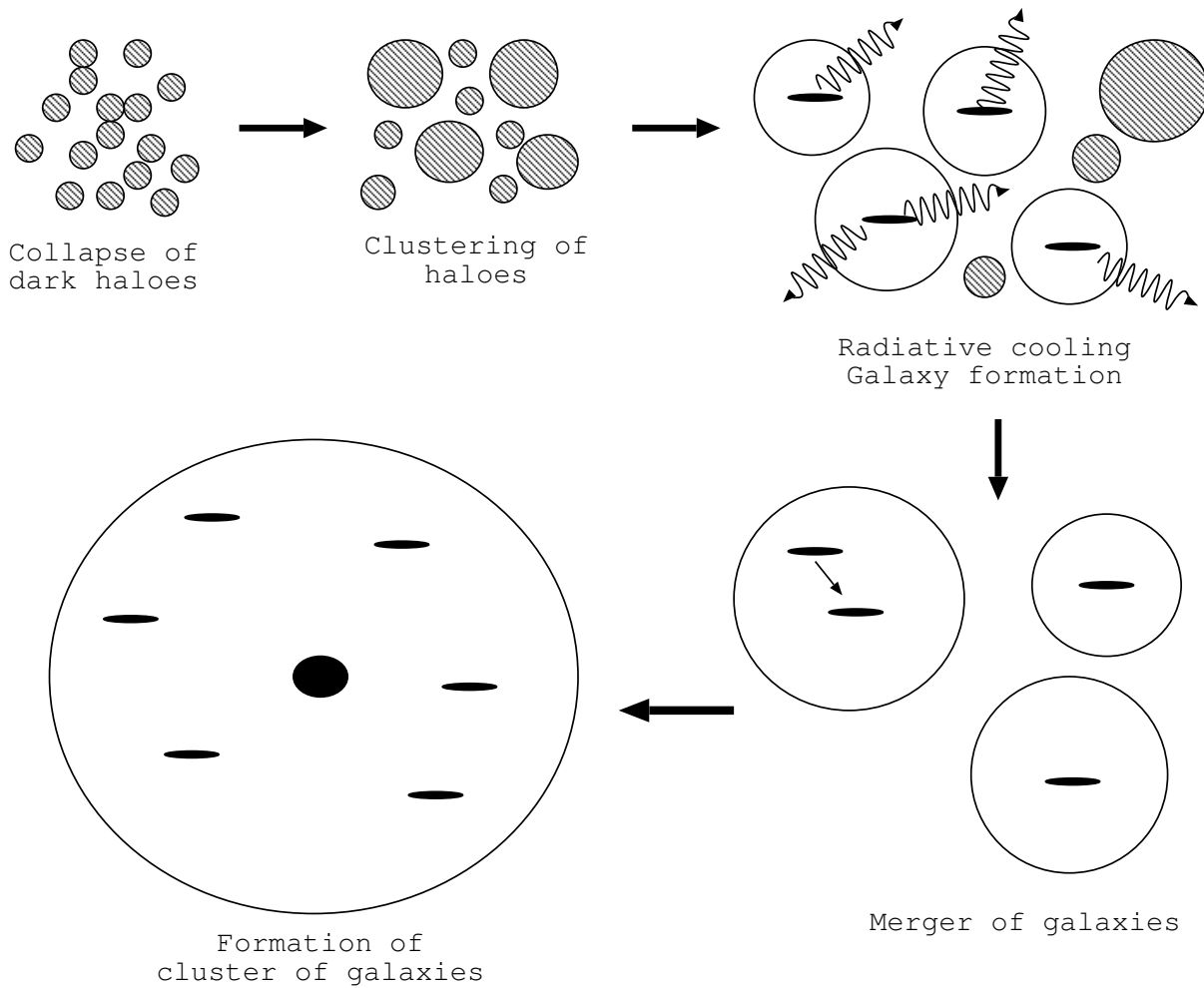


Figure 1.1: Schematic description of galaxy formation process in the hierarchical clustering scenario. The circles denote the dark haloes. The hatched circles mean that the baryonic gas in the dark haloes does not shrink because the radiative cooling is not effective. The symbols painted out with black show the galaxies. Since the evolution of the dark haloes is dominated by the gravity, the clustering continues throughout. The baryonic component, by contrast, the radiative cooling becomes effective when the density and temperature exceed a threshold, so that the gas loses the internal energy and shrink, then the density increases and stars are formed.

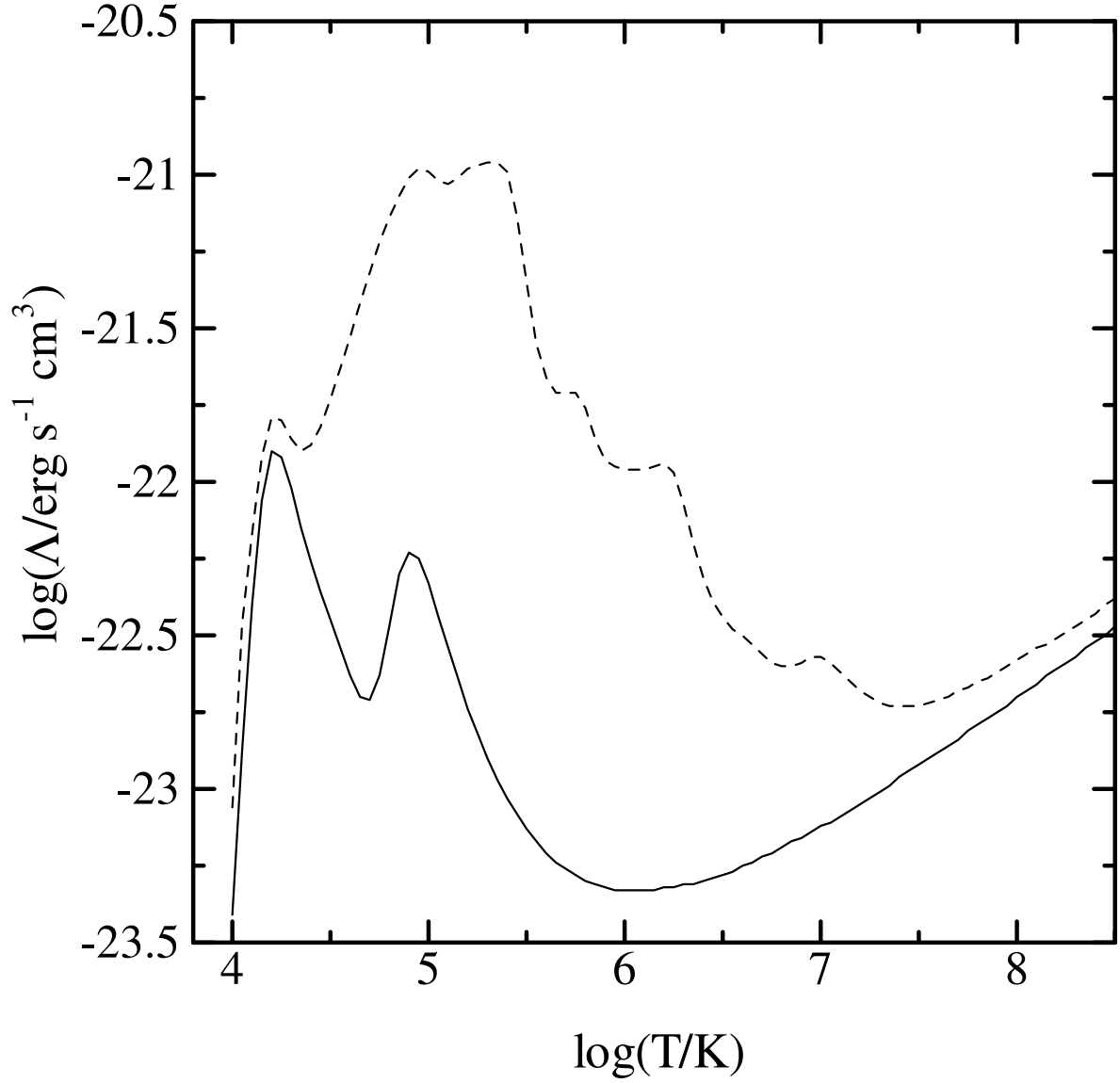


Figure 1.2: Cooling function from Sutherland & Dopita (1993). The solid and the dashed lines denote the cooling function of the primordial gas and that of the gas with solar abundance, respectively.

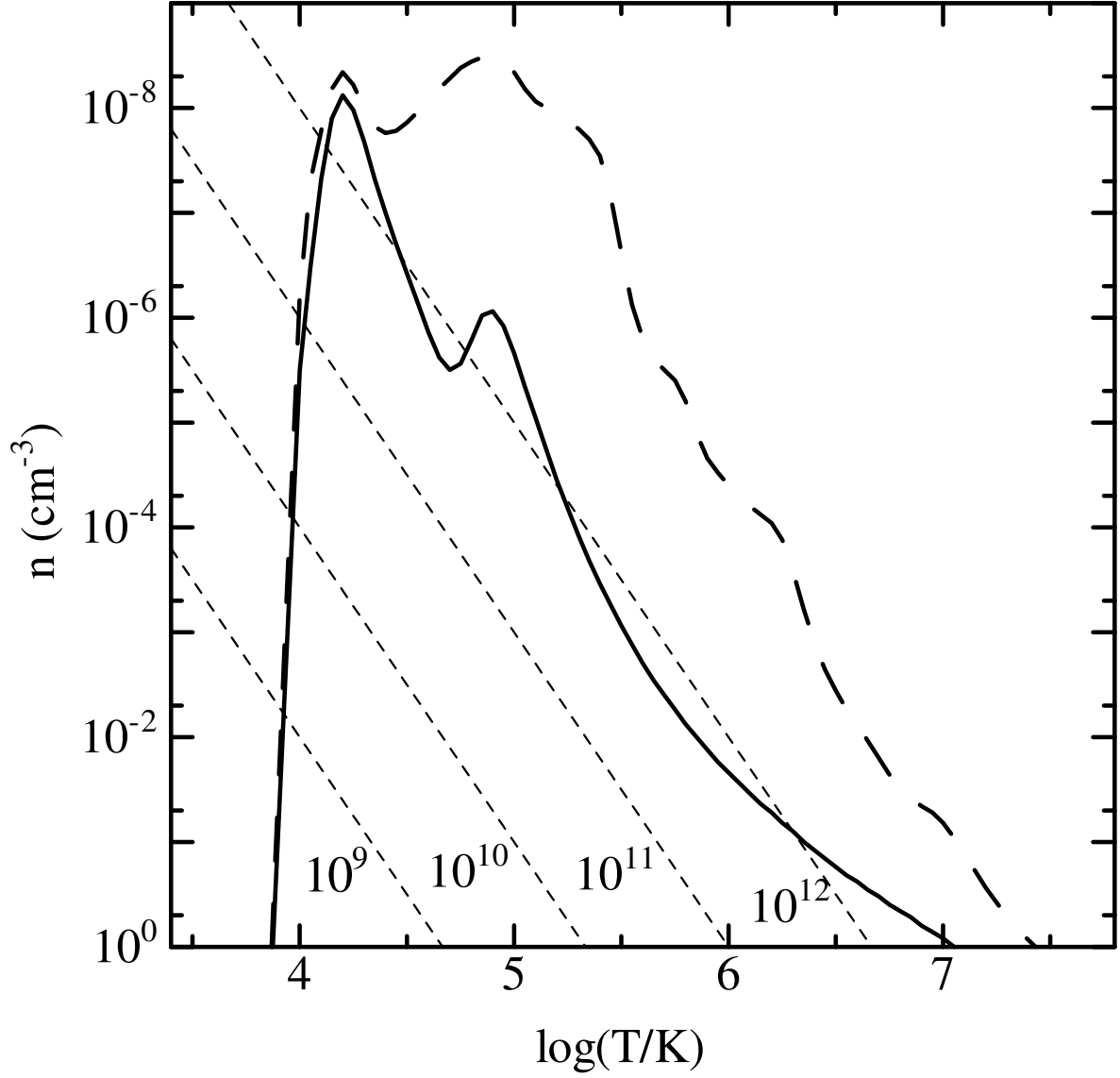


Figure 1.3: Cooling diagram. This figure is essentially the same as Fig.1 in Rees & Ostriker (1977). The solid line denotes the line on which $\tau_{cool} = \tau_{dyn}$ when τ_{cool} is estimated by the cooling function of primordial gas. The long-dashed line is the same as the solid line, but for solar abundance gas. If a halo collapses with a density and temperature below the lines, gas in the halo will lose the internal energy and forms a galaxy. The short-dashed straight lines are estimated from eq.(1.3) by the fixed Jeans mass. The Jeans masses are $10^9 M_\odot$, $10^{10} M_\odot$, $10^{11} M_\odot$, and $10^{12} M_\odot$, from left to right.

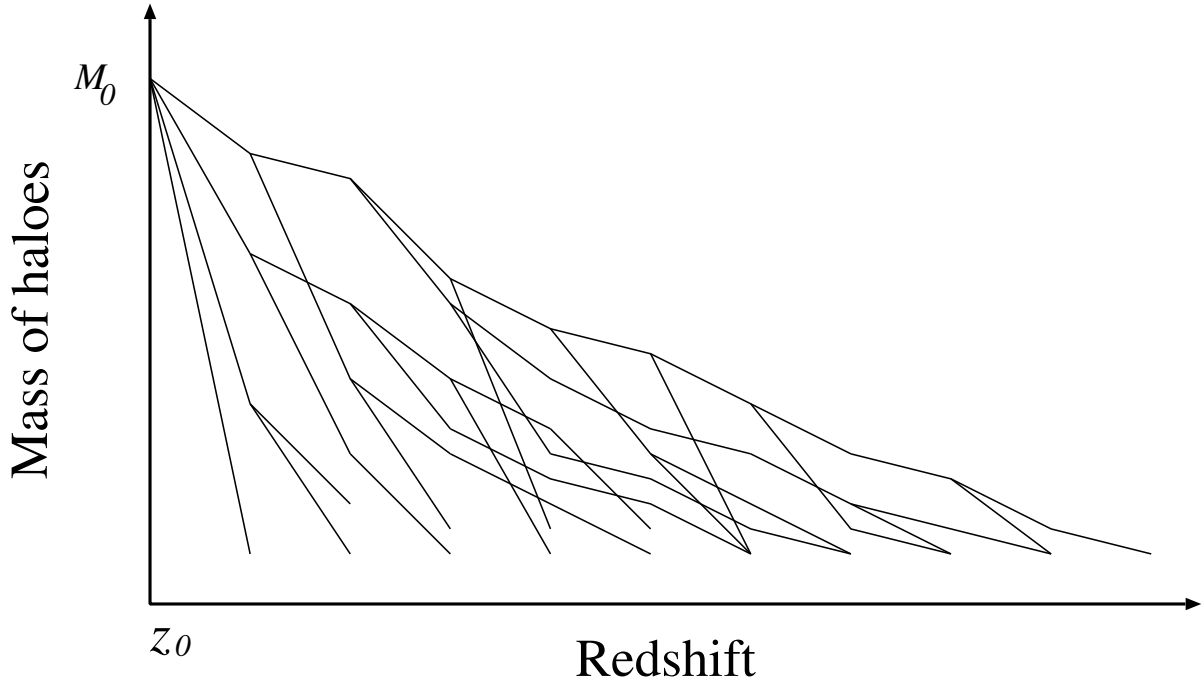


Figure 1.4: Example of merging paths of dark haloes. The halo finally formed has the mass M_0 at $z = z_0$. The branches denote the progenitors of the halo. The progenitors merge together at the ‘nodes’ of the branches. The mass of progenitors evolves by the mergers of progenitors and accretion of diffuse matter.

Chapter 2

The effect of spatial correlations on merger trees of dark matter haloes

2.1 INTRODUCTION

When we consider the galaxy formation process in the hierarchical clustering scenario, it is important to consider a set of merging paths, or *merger tree*, of each galaxy, because many varieties of properties of galaxies result from the merging paths. In this Chapter, the merging history of dark haloes is examined.

The following two models of constructing the merging history have been often used in the semi-analytic models. One of them is based on the PS formalism. This work is originally done by Kauffman & White (1993; hereafter KW). They constructed a merger tree by considering progenitors of each halo at every time by using a Monte Carlo method based on an extension of the PS formula. The PS formula gives us the number density of haloes $n(M)$, where M is mass of haloes, at an epoch, and the extended formula gives us the number density of progenitors of a halo with mass M_0 at a past epoch $n(M_1|M_0)$, where M_1 is mass of progenitors. This number density shows the ensemble average of the actual number densities of haloes, and the actual values are realized by the Monte Carlo method.

Another approach to construction of a merger tree is the Block model, which was developed by Cole & Kaiser (1988). The Block model takes the Monte Carlo procedure described as follows: First of all, the density contrast is assigned to the largest block with mass M_0 ($\sim 10^{16} M_\odot$) which has the variance of the density contrast, $\sigma^2(M_0)$. Next, the largest block is divided into two blocks with the same mass $M_1 (= M_0/2)$. The additional positive density fluctuation generated by a random Gaussian distribution with variance $\sigma^2(M_1) - \sigma^2(M_0)$ is assigned to one of the two divided blocks with mass $M_1 (= M_0/2)$ and a negative fluctuation with the same absolute value of the amplitude as the positive one is assigned to the other divided block. The same procedure is repeated for M_1, M_2, \dots down to the smallest mass scale under consideration, thereby constructing the merger tree.

Recently, a new approach to construction of merger trees has been proposed by Rodrigues & Thomas (1995) (we call this the *Merging Cell model* for convenience throughout this thesis). In their model, the random Gaussian density fluctuation field is realised on spatial grids as in

constructing initial conditions of N-body simulations, so it is expected that this model naturally includes information about the spatial correlation. Then, by finding the region of the collapsed cells or blocks with each mass scale, we can construct the merger tree (see Section 2.3.1). We expect that this model is more realistic and useful for galaxy formation although spherical collapse and random Gaussian density fluctuations are assumed.

Incidentally, it has been pointed out that the PS formula has the following crucial weak points. It is important to discuss these weak points for the following reasons. The analytic mass function such as the PS formalism is an important reference point for checking the validity of the models constructing the merger trees by comparing the analytic mass function with the mass functions given by the merger tree models. Moreover, many authors use the merger tree model based on the extension of the PS model. Therefore if the reliability of the PS formalism decreases, that of the merger tree models based on the PS formalism should decrease.

The PS formula is derived as follows: In an Einstein-de Sitter universe, spherical overdense regions collapse and virialise when their linear density contrast reaches $\delta_c = 1.69$ (Gunn & Gott 1972; see Appendix D). Then, assuming that the density fluctuations obey a random Gaussian distribution and that the collapse of the haloes is spherically symmetric, we can get the volume fraction $f(\geq \delta_c, M)$ of the regions of collapsed objects whose masses are larger than the mass M . So, the region of the dark haloes with mass scale M is equal to $\partial f / \partial M$. Thus they proposed the formula for counting the number density of objects of mass scale M . However, only overdense regions were considered in the analysis. Even if the density contrast smoothed on the mass scale M is less than δ_c , there is a possibility such that the density contrast smoothed on the larger mass scale than M is greater than δ_c . We must consider this case to count exactly the number density of the dark haloes. This problem is called the ‘cloud-in-cloud’ problem. Press & Schechter (1974) *simply* multiplied the number density by a ‘fudge factor’ of 2 without a good reason.

Peacock & Heavens (1990) and Bond et al. (1991) attempted to solve the cloud-in-cloud problem by using the peak formula. They considered the *upcrossing* probability that a density contrast which is lower than δ_c with a smoothing scale M exceeds δ_c for the first time when increasing the smoothing scale. In the case that the density field is smoothed with the sharp k -space filter, they found that the factor of 2 introduced by PS is correct. The cloud-in-cloud problem is also solved for Poisson fluctuations by Epstein (1983).

In the cloud-in-cloud problem, however, we must consider the *spatial correlations of the density fluctuations* since objects have non-zero size in reality. Yano, Nagashima & Gouda (1996; hereafter YNG, see Appendix A) analysed the cloud-in-cloud problem taking explicitly into account the spatial correlation of the density fields. They explicitly introduced the two-point correlation function in the mass function by using Jedamzik’s formula (Jedamzik 1995) in which the number density of the collapsed objects is given in the form of the integral equation which is different from the PS formula. It is also proved by YNG that the results derived from the Jedamzik formula are consistent with those derived from the PS formula on the assumption that the collapse is spherically symmetric when the spatial correlations are not taken into consideration. However, YNG showed that the spatial correlations greatly affect the mass function (see Appendix A). Therefore, there is a possibility that the merger tree is also affected by the spatial correlations whose effects have never explicitly been taken into account in the KW method and the Block model. So it is very important to analyse the effects of

spatial correlations of the density fields on the merger trees of dark haloes.

In this Chapter, we present the mass functions of dark haloes calculated using the Merging Cell model. They are compared with the mass functions given by the PS formula and the Block model. We then explicitly show that the main origin of differences between the mass functions given by the different methods is the effect of spatial correlations. We find that the mass functions given by the YNG formula which takes explicitly into account the spatial correlations are consistent with those given by the Merging Cell model and so the Merging Cell model correctly includes the effect of the spatial correlations. Furthermore, by applying the Jedamzik formula, we present an analytical expression of the mass function derived from the Block model and show quantitatively why and how the mass function given by the Block model is different from those derived from the PS formula and the Merging Cell model.

In the Merging Cell model, some haloes happen to overlap since the non-zero size of the haloes is considered explicitly. So, we must consider the criterion of collapse and merging for the overlapped haloes. We also show how the change of the criterion affects the mass function in the Merging Cell model.

In Section 2.2, we give analytical formulae for estimating the mass functions by using the Press-Schechter formula, the Jedamzik formula and the YNG formula. In Section 2.3, the Merging Cell model, the Block model and the extension of the PS formalism are reviewed briefly. In Section 2.4, it is shown that the Merging Cell model is consistent with the mass function which is derived by the analytical formula in which the spatial correlations are taken into account. The mass function given by using the Jedamzik formalism which reproduces that given by the Block model is also presented. Furthermore, we also show how the mass function is changed if the overlapping criterion is changed. We devote Section 2.5 to conclusions and discussion.

2.2 ANALYTIC APPROACH TO MASS FUNCTIONS

In this section, we present the PS formula, the Jedamzik formula and also the mass functions derived by our formula (YNG formula) which explicitly includes the effects of the spatial correlations. The details for derivation of the following mass functions are shown in Appendix A.

2.2.1 Press-Schechter formula

The probability of finding the region whose linear density contrast smoothed on the mass scale M , δ_M , is greater than or equal to δ_c is assumed to be expressed by the random Gaussian distribution given by

$$f(\geq \delta_c, M) = \frac{1}{\sqrt{2\pi}\sigma(M)} \int_{\delta_c}^{\infty} \exp\left(-\frac{\delta^2}{2\sigma^2(M)}\right) d\delta. \quad (2.1)$$

This probability corresponds to the ratio of the volume of the region above δ_c in the density contrast smoothed on the mass scale M to the total volume (in a fair sample of the Universe). Therefore, the difference between $f(\geq \delta_c, M)$ and $f(\geq \delta_c, M + dM)$ represents the volume of

the region for which $\delta_M = \delta_c$ precisely. The density contrast of an *isolated* collapsed object is precisely equal to δ_c because an object with $\delta > \delta_c$ would be eventually counted as an object of larger mass scale. The volume of each object with mass scale M is $M/\bar{\rho}$. Then we obtain the following relation,

$$\frac{Mn(M)}{\bar{\rho}}dM = -\frac{\partial f(\geq \delta_c, M)}{\partial M}dM, \quad (2.2)$$

where $n(M)$ means the number density of objects with mass M , that is, the mass function. However, the underdense regions are not considered in the above equation. Hence, Press and Schechter *simply* multiply the number density by a factor of 2,

$$\frac{Mn(M)}{\bar{\rho}}dM = -2\frac{\partial f(> \delta_c, M)}{\partial M}dM. \quad (2.3)$$

This factor of 2 has long been noted as a weak point in the PS formula (the so-called ‘cloud-in-cloud’ problem). Peacock & Heavens (1990) and Bond et al. (1991) proposed a solution to this problem by taking account of the probability P_{up} that a subsequent filtering of larger scales might result in having $\delta > \delta_c$ at some point, even when at smaller filters, $\delta < \delta_c$ at the same point. They found that the factor of 2 in the PS formula is reproduced by using the sharp k -space filter given by

$$W_i(k) = \begin{cases} 1, & k \leq k_c(M_i) \\ 0, & k > k_c(M_i). \end{cases} \quad (2.4)$$

2.2.2 Jedamzik formula

Jedamzik (1995) proposed another approach to the cloud-in-cloud problem.

Now, we consider the regions whose smoothed linear density contrasts on the mass scale M_1 are above δ_c . Each region must be included in an isolated collapsed object with mass $M_2 \geq M_1$. Therefore, we obtain the following equation,

$$f(\geq \delta_c, M_1) = \int_{M_1}^{\infty} P(M_1, M_2) \frac{M_2}{\bar{\rho}} n(M_2) dM_2, \quad (2.5)$$

where $P(M_1, M_2)$ means the conditional probability of finding a region of mass scale M_1 in which δ_{M_1} is greater than or equal to δ_c , provided it is included in an isolated overdense region of mass scale M_2 . By ‘the Jedamzik formula’ we mean the procedure in which the mass functions are estimated by solving eq.(2.5). If $P(M_1, M_2)$ is given by the conditional probability $p(\delta_{M_1} \geq \delta_c | \delta_{M_2} = \delta_c)$, $P(M_1, M_2)$ is written as follows by using Bayes’ Theorem,

$$\begin{aligned} P(M_1, M_2) &= p(\delta_{M_1} \geq \delta_c | \delta_{M_2} = \delta_c) \\ &= \frac{1}{\sqrt{2\pi}\sigma_{\text{sub}}} \int_{\delta_c}^{\infty} \exp\left\{-\frac{1}{2} \frac{(\delta_{M_1} - \delta_c)^2}{\sigma_{\text{sub}}^2}\right\} d\delta_{M_1} \\ &= \frac{1}{2}, \end{aligned} \quad (2.6)$$

$$\sigma_{\text{sub}}^2 = \sigma^2(M_1) - \sigma^2(M_2) \quad (2.7)$$

where we use the sharp k -space filter. Thus we can obtain the PS formula, naturally including the factor of 2 as can be seen from eqs.(2.5) and (2.6).

However, it is insufficient to use eq.(2.6) for more realistic estimation of the mass function because it is necessary to consider the spatial correlation of the density fluctuations due to the finite size of the objects. Therefore, we must consider the probability $P(r, M_1, M_2)$ of finding $\delta_{M_1} \geq \delta_c$ at a distance r from the centre of an isolated object of mass scale M_2 . Then we can get the probability $P(M_1, M_2)$ by spatially averaging $P(r, M_1, M_2)$.

Because we expect that the isolated collapsed objects are formed around density peaks, the constraints to obtain the above probability $P(r, M_1, M_2)$ are given as follows:

1. The linear density contrast, δ_{M_2} , of the larger mass scale M_2 , should be equal to $\delta_c = 1.69$ at the centre of the object.
2. Objects of the mass scale M_2 must contain a maximum peak of the density field, *i.e.*, the first derivative of the density contrast $\nabla\delta_{M_2}$ must be equal to 0 and each diagonal component of the diagonalized Hessian matrix ζ of the second derivatives must be less than 0 at the centre of the object.
3. The density contrast of the smaller mass scale $M_1 (\leq M_2)$ which collapsed and is included in an object of mass scale M_2 must satisfy the condition $\delta_{M_1} \geq \delta_c$ at distance r from the centre of the larger object.

The probability which we get from the above conditions is:

$$P(r, M_1, M_2|\text{peak}) = P(\delta_{M_1} \geq \delta_c | \delta_{M_2}, \text{peak}). \quad (2.8)$$

Since the detailed derivation of the above probability is complicated, we omit it here (see Appendix A). By spatially averaging eq.(2.8) in the region of M_2 , we obtain $P(M_1, M_2)$ as follows:

$$P(M_1, M_2) = \frac{\int_0^{R_2} P(r, M_1, M_2|\text{peak}) 4\pi r^2 dr}{\int_0^{R_2} 4\pi r^2 dr}, \quad (2.9)$$

where R_2 means the radius of the region M_2 , $R_2 = (3M_2/4\pi\bar{\rho})^{(1/3)}$. The cumulative multiplicity functions, which will be defined in the following sections, are estimated by using eq.(2.8) and are shown by the short-dashed lines in Fig.2.3 in the cases of the power spectrum $P(k) \propto k^n$ with $n = 0$ and -2 , respectively. We call this formula the YNG formula hereafter.

2.3 MODELS OF MERGER TREES

In this section, we briefly review the Merging Cell model (hereafter MCM), the Block model, and the extension of the PS model. The extension of the PS model is used in Chapter 5.

2.3.1 Merging Cell model

We briefly review the MCM according to the procedure and the notation shown in Rodrigues & Thomas (1995).

First, the random Gaussian density field is realised in a periodic cubical box of side L . In the random Gaussian distribution, the Fourier mode of density contrast δ is the mean density of the universe) obeys the following probability for its amplitude and phase(BBKS),

$$P(|\delta_{\mathbf{k}}|, \phi_{\mathbf{k}})d|\delta_{\mathbf{k}}|d\phi_{\mathbf{k}} = \frac{2|\delta_{\mathbf{k}}|}{P(k)} \exp \left\{ -\frac{|\delta_{\mathbf{k}}|^2}{P(k)} \right\} d|\delta_{\mathbf{k}}| \frac{d\phi_{\mathbf{k}}}{2\pi}, \quad (2.10)$$

where $\phi_{\mathbf{k}}$ is the random phase of $\delta_{\mathbf{k}}$, $\delta_{\mathbf{k}} = |\delta_{\mathbf{k}}| \exp(i\phi_{\mathbf{k}})$ and $P(k)$ is the power spectrum $\langle |\delta_{\mathbf{k}}|^2 \rangle$, where the angle brackets mean the ensemble average of the universe. Then, the density contrast at each grid ('cell') is given by the Fourier transform,

$$\delta(\mathbf{x}) = \frac{V}{(2\pi)^3} \int_0^{k_c} \delta_{\mathbf{k}} e^{i\mathbf{k} \cdot \mathbf{x}} d^3k, \quad (2.11)$$

where k_c is the cut-off wavenumber.

Next, averaging the density fluctuations within cubical *blocks* of side 2, 4, ..., L, the fluctuations of the various smoothing levels are constructed. At each smoothing level, displacing the smoothing grids by half a blocklength in each direction of each axis, eight sets of *overlapping grids* are constructed in order that a density peak will be approximately centred within one of them (see Fig.2.1).

Then, the density fluctuations within blocks and cells are combined into a single list and ordered in decreasing density. The fluctuations are investigated from the top of the list. It is decided by the following rules whether each block or cell can collapse. Note terminology that *halo* is a block or cell which has already collapsed, and an *investigating* region is a block or cell whose linear density contrast is just equal to δ_c at the reference time. We decide whether or not an investigating region can collapse at that time according to the following rules.

- (a) If an investigating region includes no haloes, the investigating region(*block* or *cell*) can collapse and can be identified as a new halo.
- (b) When an investigating region includes a part of a halo, if the *overlapping region* has at least half the minimum of the masses of the halo and the investigating region, then the investigating region can collapse (see Fig.2.2). This is the criterion of collapse of the investigating region and merging for the overlapped haloes. We call this criterion *the overlapping criterion* in this paper.
- (c) If the investigating region has half or more of its mass contained in exactly one pre-existing halo and the overlapping criterion (b) is satisfied for any overlapped haloes then merge them together as part of the new structure. This is the criterion for linking of haloes (see Fig.2.2, and also Fig.2.5 in Section 2.4.3).

These criteria are those chosen by Rodrigues & Thomas. The condition (c), the linking condition, prevents the growth of filamentary structures because galaxies that we observe are not filamentary. However, we should note that the filament structures of dark matter certainly appear as shown in numerical simulations. Then the criterion for linking is just an assumption. We will change the overlapping and linking criteria (b) and (c) later and see how the mass function is changed.

It must be noted here that in the MCM, because overlapping grids are used, the mass spectrum is close to continuous, rather than restricted to powers of two as in the Block model.

2.3.2 Block model

In this subsection, the Block model according to Cole & Kaiser (1988) is briefly reviewed. Now, we consider a large block with mass $M_0 (\sim 10^{16} M_\odot)$, divide this into two, and realize blocks with various mass scales by successively dividing smaller and smaller blocks. We obtain a set of blocks of discrete masses, $M_i = M_0/2^i (i = 1, 2, \dots, N)$ where N is an integer equal to 27 in our calculation shown later.

Here $\sigma(M_i) = \sigma_i$ means the standard deviation of the density fluctuations smoothed on a mass scale M_i . When the power spectrum is written in the power-law form $P(k) \propto k^n$, the standard deviation is given by

$$\begin{aligned} \sigma_i^2 &= \frac{4\pi V}{(2\pi)^3} \int_0^\infty W_i^2(k) P(k) k^2 dk \\ &= \left(\frac{M_i}{M_*} \right)^{-\frac{3+n}{3}}, \end{aligned} \quad (2.12)$$

where M_* is the mass on which the variance is unity, and $W_i(k)$ is the window function. We define the quantities Σ_i as follows:

$$\Sigma_0 = \sigma_0, \quad (2.13)$$

$$\Sigma_i^2 = \sigma_i^2 - \sigma_{i-1}^2, \quad i \geq 1. \quad (2.14)$$

We generate the random density fluctuations on each block as follows: First of all, a density contrast generated by the random Gaussian distribution with the variance Σ_0 is assigned to the largest block. This corresponds to the density contrast smoothed on the mass scale M_0 . Then the positive random variable generated by the random Gaussian distribution with the variance Σ_1 is added to one of the two divided blocks with the mass $M_1 = M_0/2$ and a negative one with the same absolute value of the amplitude is added to the other divided block. Repeating this procedure from $i = 0$ until $i = N$, we obtain a tree of density contrasts of the blocks with various mass scales. The condition of collapse for a block at the redshift z is that the density contrast of the block equals $\delta_c = 1.69(1+z)$ (z ; redshift). In this way, we can construct the merger tree of the dark haloes.

2.3.3 Extension of the PS formalism

Here the extension of PS formalism by Kauffmann & White (1993) and Somerville & Kolatt (1997) is reviewed.

The probability distribution function finding a point contained in a progenitor with mass $M \geq M_1$ at z_1 of a halo with M_0 collapsed at z_0 is

$$f(M_1, z_1 | M_0, z_0) = \int_{\delta_c}^\infty \frac{(1+z_1)}{\sqrt{2\pi(\sigma_1^2 - \sigma_0^2)}} \exp \left\{ -\frac{1}{2} \frac{(1+z_1)\delta_1 - (1+z_0)\delta_c}{\sigma_1^2 - \sigma_0^2} \right\} d\delta_1. \quad (2.15)$$

This is obtained from the two variate Gaussian distribution function and the Bayes' theorem. Therefore the probability distribution function finding a progenitor with mass M_1 at z_1 is obtained as follows by using the PS formalism [eq.(2.3)],

$$\begin{aligned} F(M_1, z_1|M_0, z_0)dM_1 &= -2 \frac{\partial f(M_1, z_1|M_0, z_0)}{\partial M_1} dM_1 \\ &= \frac{2\delta_c(z_1 - z_0)}{\sqrt{2\pi}(\sigma_1^2 - \sigma_0^2)^{3/2}} \frac{d\sigma_1}{dM_1} \exp \left\{ -\frac{\delta_c^2}{2} \frac{(z_1 - z_0)^2}{\sigma_1^2 - \sigma_0^2} \right\} dM_1. \end{aligned} \quad (2.16)$$

Using the above equation, the number of progenitors with mass M_1 of a halo with mass M_0 is

$$N_{\text{prog}}(M_1, z_1|M_0, z_0) = F(M_1, z_1|M_0, z_0) \frac{M_0}{M_1}. \quad (2.17)$$

Next the number of haloes are realized on the grid in $M - z$ plane according to eq.(2.17) randomly (see Fig.fig:MH). We need merging histories for a large number of haloes, $n \sim 100$. Now we consider the merging paths of haloes with M_0 at z_0 . According to eq.(2.17), the number of progenitors with mass M_i , $n \times N_{\text{prog}}(M_i, z_0 + dz|M_0, z_0)$ are estimated, where $dz \sim 0.1$. We round the value of the number to the nearest integer. This process is recursively performed for more ancient progenitors, as $[n \times N_{\text{prog}}(M_i, z_0 + dz|M_0, z_0)] \times N_{\text{prog}}(M_j, z_0 + 2dz|M_i, z_0 + dz)$. After this, we obtain discretized mass functions of progenitors at many redshifts.

Finally, we must assign these realized haloes to each parent halo. First the maximum mass progenitors are assigned to the N_{prog} parent haloes randomly. Next the second maximum mass progenitors are assigned to the parent haloes with a probability proportional to the rest of mass of the parent haloes. This process are repeated for all progenitors. Thus we obtain merger trees.

This method has some weak points. One of them is the discreteness of mass of haloes. Another one is the ambiguous process for assigning progenitors to their parents. In this process, the mass conservation is broken, and it is not trivial that the 'random assignment' procedure is consistent with the other probability processes. The formalism by Kauffmann & White (1993) is improved by Somerville & Kolatt (1997) for satisfying the mass conservation of haloes and for removing the ambiguous random assignment procedure. Next their improved formalism is reviewed.

Kauffmann & White use eq.(2.17) for estimating the number of progenitors. The probability variable in this equation is the number of progenitors. Somerville & Kolatt do not use the equation, but they treat the mass as a probability variable. Their algorithm is simple and can be quickly performed as follows.

We define the variables; $S_i \equiv \sigma_i^2$ and $\omega_i \equiv \delta_c(1+z_i)$. We consider the probability distribution function of $\Delta S = S_1 - S_0$, $p(\Delta S, \Delta\omega)d\Delta S$, where $\Delta\omega = \omega_1 - \omega_0$. When the density fluctuation fields are random Gaussian fields, this probability is simply

$$p(\Delta S, \Delta\omega)d\Delta S = \frac{1}{\sqrt{2\pi}} \frac{\Delta\omega}{(\Delta S)^{3/2}} \exp \left[-\frac{(\Delta\omega)^2}{2\Delta S} \right] d\Delta S. \quad (2.18)$$

This function is a simple Gaussian distribution, if we change the variable to $x \equiv \Delta\omega/\sqrt{\Delta S}$. After this, we interpret the variance S as the mass M .

The following procedure is based on a Monte Carlo method. First we set a mass M_0 , or S_0 , as a mass of a finally collapsing halo, e.g., a cluster scale or the ‘Milky Way’ scale, and ‘time-step’ $\Delta\omega$. By using eq.(2.18), we pick out ΔS randomly. From this ΔS , S_1 , that is, M_1 , is determined. This M_1 is interpreted as a mass of a progenitor halo of the halo with mass M_0 , collapsing at $z = z_1$ estimated by $\Delta\omega$. If $M_1 \leq M_l$, where M_l is a minimum mass for an object identified as an isolated halo at a corresponding redshift, the mass M_1 is added to a diffuse ‘accretion mass’.

The above process is repeated until the rest of mass of the halo become less than M_l . In the same way, merging paths are recursively realized by regarding the halo with mass M_1 as a starting point halo such as the halo with mass M_0 . Mass functions at various redshifts obtained by using the above procedure reproduce the Press-Schechter mass function well (Somerville & Kolatt 1997).

2.4 RESULTS

2.4.1 Mass spectrum

We have tested our code on power-law density fluctuation spectra. We assume that linear density fluctuations obey the random Gaussian distribution with a power-law power spectrum $P(k) \propto k^n$, where $n = 0$ and -2 . We consider only the Einstein-de Sitter universe ($\Omega = 1, \Lambda = 0$) in this paper. This power spectrum can be transformed into a mass spectrum of density fluctuations, $\sigma(M) \propto M^{\frac{3+n}{6}}$, which means a standard deviation when the field is smoothed on a mass scale M . In Fig.2.3, we show the scale-free mass spectrum ($n = 0$ and -2), which are adopted to calculate the mass functions by using Jedamzik formalism, and show the standard deviations on each smoothing mass scale in the box of $L=128$. A difference between the scale-free spectra and the actual calculations arises from the loss of power of waves of large wavenumber due to the finite box size. The mass spectrum in the MCM is in agreement with that of the scale-free spectrum in the case of $n = 0$ while in the case of $n = -2$ a difference between both spectra is not negligible. We will discuss about an influence of the difference between the spectra on the mass functions in the next subsection.

2.4.2 MCM cumulative multiplicity functions

We calculate the cumulative multiplicity function $P(\geq M)$, which is defined as the mass fraction of objects whose mass is larger than a mass M (in a fair sample of the Universe), by following the various methods which are mentioned in Section 2.2 and 2.3. The multiplicity function $P(M)d\ln M$ (which we define in a logarithmic interval of mass) and the cumulative multiplicity function are related to the mass function $n(M)dM$ as follows:

$$P(M)d\ln M \equiv \frac{d\rho}{\bar{\rho}} = \frac{M^2 n(M)}{\bar{\rho}} d\ln M, \quad (2.19)$$

$$P(\geq M) = \int_M^\infty P(M) \frac{dM}{M}. \quad (2.20)$$

In the MCM, we take the box size $L = 128$. M_* is defined as $\sigma(M_*) = 1$ (see eq.(2.12)) and here the mass in the block with the mass scale M_* is assigned to eight cells. In the Block model, the largest box size is assigned to the mass scales $M_0 = 10^5 M_*$ in the case of $n = 0$ and $10^7 M_*$ in the case of $n = -2$. We consider block sizes with $M_i = M_0/2^i (i = 1, 2, \dots, N = 27)$.

In Figs.2.4(a) and (b), we show the cumulative multiplicity functions derived by the MCM, the YNG formula, the PS formula and the Block model for the case of $n = 0$ and $n = -2$, respectively.

The multiplicity functions of the MCM are shown only in the mass range ($\log(M/M_*) \geq 0$) which corresponds to the range larger than or equal to eight cells. The reason is as follows: On the smallest mass scale (one-cell scale) in the numerical calculations, the power of the density fluctuations on the one cell scale cannot be correctly produced in agreement with the theoretically estimated power of the scale-free mass spectrum $\sigma(M) \propto M^{-(3+n)/6}$ due to the finiteness of the cell size in the numerical calculations.

It is found that the multiplicity functions given by the MCM are well fit by those given by the YNG formula in the case of $n = 0$. Thus the MCM naturally and correctly takes into consideration the spatial correlations. An origin of a little deviation on the mass scale $\log(M/M_*) \gtrsim 0.8$ is that haloes larger than about 50 cells have various shapes, rather than the spherical shape, so the assumption of spherically symmetric collapse fails. Apparently, however, in the case of $n = -2$ the difference between the functions of the MCM and the YNG is large. The difference results mainly from missing power of density fluctuations outside the box (see Fig.3 in Rodrigues & Thomas 1996), hence it is a numerical effect, while the effect of the missing power is negligible in the case of $n = 0$. In scale-free power spectra $P(k) \propto k^n$, the characteristic mass M_* evolves in proportion to $a^{6/(3+n)}$ (a : the cosmic scale factor) because $\sigma(M) \propto a$ and $\sigma(M_*) \equiv 1$. In the case of $n = -2$, $M_* \propto a^6$. We find that the ratio of the mass spectrum which is realised in the MCM to the ideal scale-free mass spectrum is about 0.95 at a mass scale $\log(M/M_*) \simeq 0.9$ which corresponds to 64 cells. Therefore the difference between the functions of the MCM and the YNG is about a factor of 1.4 ($\simeq 0.95^{-6}$) in the direction of horizontal axis because the mass functions are normalized by M_* in the direction of horizontal axis. It is thought that origins of the difference are the above numerical effect and nonspherically shape in the MCM. So we can say that the comment about the spatial correlation in the MCM, which is mentioned for $n = 0$, is right even for $n = -2$.

Furthermore, we will show in the next subsection that the multiplicity function given by the Block model can be reproduced by using the Jedamzik formula without consideration of the spatial correlations and thereby demonstrate that the difference between the multiplicity functions given by the Block model and the MCM results from the effect of the spatial correlations.

2.4.3 Block model multiplicity functions

Here we reproduce analytically the multiplicity function given by the Block model by using the Jedamzik formula.

Since we consider the discrete mass of the blocks ($M_i = M_0/2^i$) in the Block model, the density contrast in the blocks which are identified as isolated collapsed haloes is generally greater than δ_c . We cannot recognize the just collapsed halo whose density contrast is precisely δ_c if

we follow the procedure of the Block model. Therefore, the conditional probability $P(M_1, M_2)$ in this case must be approximately expressed as:

$$\begin{aligned}
 P(M_1, M_2) &= p(\delta_{M_1} \geq \delta_c | \delta_{M_2} \geq \delta_c) \\
 &= \frac{p(\delta_{M_1} \geq \delta_c, \delta_{M_2} \geq \delta_c)}{p(\delta_{M_2} \geq \delta_c)} \\
 &= \frac{\int_{\nu_{1c}}^{\infty} d\nu_1 \int_{\nu_{2c}}^{\infty} d\nu_2 \exp \left\{ -\frac{(\nu_1 - \epsilon' \nu_2)^2}{2(1 - \epsilon'^2)} - \frac{\nu_2^2}{2} \right\}}{\sqrt{2\pi(1 - \epsilon'^2)} \int_{\nu_{2c}}^{\infty} d\nu_2 \exp \left\{ -\frac{\nu_2^2}{2} \right\}}. \tag{2.21}
 \end{aligned}$$

It must be noticed here that we must consider the case of $\delta_{M_2} \geq \delta_c$ instead of the case of $\delta_{M_2} = \delta_c$ which appeared in eq.(2.6). In this case, of course, the spatial correlation is not taken into consideration. The detailed derivation of the above probability and notation are explained in Appendix B. Inserting the above conditional probability, eq.(2.21), into eq.(2.5), we can estimate the multiplicity function in this case.

In Fig.2.5, we show the multiplicity functions given by the above procedure (solid line) and the Block model (cross, solid square and open square). The cross, solid square and open marks in the Block model mean that the masses of the largest block M_0 equal $10^5 M_*$, $10^3 M_*$ and $10 M_*$, respectively. Here in the Block model, the multiplicity function over a large dynamic range in mass can be produced by combining the functions derived by the Block model with $M_0 = 10^5 M_*$, $10^3 M_*$ and $10 M_*$ in the case of $n = 0$ and $10^7 M_*$, $10^5 M_*$ and $10^3 M_*$ in the case of $n = -2$ and block sizes with $M_i = M_0/2^i$ ($i = 1, 2, \dots, 27$) in each case. We find that the multiplicity functions given by the Block model and the approximate analytical formula derived from the Jedamzik formula fit each other well. The difference between the cumulative functions given by the Block model and the MCM mainly results from the effect of the spatial correlations while the difference between the functions given by the Block model and the PS formula results from the difference in the identification of isolated collapsed objects.

Moreover, It is also found that the PS formula and the Block model are also in agreement with each other in the case of $n = -2$ rather than in the case of $n = 0$. Note that on the galaxy scales the spectral index n is nearly equal to -2 in the CDM model. Then in the CDM model the both functions are consistent with each other (Cole & Kaiser 1988). It must be noticed that the agreement of the Block model with the PS formula depends on the power spectrum. On the other hand, the function of the MCM deviates from those of the Block model and the PS formula in which the spatial correlations of the density fluctuations are not explicitly taken into account. From these results, we can conclude that the MCM naturally and correctly takes into consideration the spatial correlations and the deviation of the multiplicity function of the MCM from those of the Block model and the PS formula results from the effect of the spatial correlations of the density fluctuations.

2.4.4 Overlapping effect

In taking into consideration the finite size of the haloes, it appears necessary to consider the serious problem of the spatial overlapping of the dark haloes. For the overlapping criterion we must consider how we can identify the number and sizes of the haloes when some haloes

overlap. In this subsection, we show the effect of the overlapping and linking criteria (Section 2.2.1, (b) and (c)) on the multiplicity function. The overlapping criterion adopted in Rodrigues & Thomas (1996) is that the investigating region can collapse when the overlapping region has at least half of the lesser of the masses of the halo and the investigating region. Here we quantify the overlapping criterion by defining a parameter, x , as the ratio of the mass of the overlapping region to the lesser of the masses of the halo and the investigating region. Rodrigues & Thomas's criterion corresponds to $x = 1/2$. By changing the value of x we show the effect of overlapping on the multiplicity function. Moreover, we introduce another parameter y as quantifying the linking criterion. We change the criterion (c) as follows: If the investigating region has y times ($x \leq y \leq 1/2$) or more of its mass contained in exactly one pre-existing halo and the overlapping criterion (b) is satisfied for any overlapped haloes then merge them together (see Fig.2.6). We investigate two cases that $y = 1/2$ and $y = x$.

Then, Rodrigues & Thomas's criterion corresponds to $x = y = 1/2$. By changing the values of x and y we show the effect of overlapping on the multiplicity function.

In Fig.2.7, we show the multiplicity functions on scales above eight cells in the cases that $y = 1/2$ and $x = 1/2, 1/4$ and $1/8$. As the value of x decreases, the multiplicity function increases on the larger mass scales because it becomes easy for larger blocks to collapse.

In Fig.2.8, we show the same as Fig.2.6 but in the case that $x = y$ and $x = 1/2, 1/4$ and $1/8$. In this case, it is not so easy for large haloes to collapse compared with $y = 1/2$. So the number of large haloes is not so much increasing.

2.5 CONCLUSIONS & DISCUSSION

In this Chapter, we have shown that the multiplicity functions given by the MCM are consistent with those given by the YNG formula. However, the functions of the MCM do not fit those given by the PS formula and the Block model. This fact means that the MCM includes the information of the spatial correlations in the density fluctuation field, but the PS formula and the Block model do not include it. Thus the effects of the spatial correlations affect the merger trees as well as the mass functions and it is important to take into account the spatial correlations in the merger tree models.

Here it must be noted that the reason why the multiplicity functions given by the MCM are well fit by those given by the YNG formula in the case that the overlapping criterion has the value of $x = 1/2$ is as follows. When obtaining the multiplicity function from eqs.(2.8) and (2.9), we integrate the $P(r, M_1, M_2)$ with respect to r from 0 to R_2 in eq.(2.9). This condition is that the centre of the halo with M_1 is included in the region occupied by the halo with M_2 . Therefore when the nearly half mass of the halo with M_1 is included in the region occupied by the halo with M_2 , the halo with M_1 is decided to be included in the halo with M_2 . This corresponds to the case $x = 1/2$. Of course, the adoption of the integration interval $[0, R_2]$ is, strictly speaking, only justified for spherically symmetric collapse. In fact, the effects of non-spherical collapse or tidal interaction among haloes may be important. We hypothesized that changing the value of x is enough to account for these effects effectively.

We also analytically produce multiplicity functions which fit those given by the Block model, by using the Jedamzik formula. When we reproduce the multiplicity functions given by the

Block model, the approximate conditional probability eq.(2.21) is adopted instead of eq.(2.6) in the PS formula. The difference from the PS formalism is that the density contrast of the isolated object is not only equal to δ_c but also greater than δ_c . This difference results from the discreteness of block mass. In the Block model, we obtain the mass set $\{M_i\}$, $M_i = M_0/2^i$. So a halo which should have the mass M , $M_i < M < M_{i+1}$, is counted as a halo with mass M_i . Therefore, the number of larger haloes is underestimated. In contrast to larger mass scales, a life time of haloes with smaller mass is increasing because a collapse time of the larger mass haloes becomes later, so the number of smaller mass haloes is increasing. It must be noticed that the conditional probability eq.(2.21) does not include the effect of the spatial correlations of the density fluctuations. We find that the multiplicity functions reproduced in this way are consistent with those given by the Block model. This result shows that the Block model does not include the spatial correlations of the density fluctuations and so the multiplicity function given by the Block model is different from those given by the MCM.

Moreover, we have shown that when the overlapping and linking criteria are changed, the multiplicity function is affected, especially on larger mass scales. As the value of the overlapping parameter, x (defined as the ratio of the mass of the overlapping region to the lesser of the masses of the halo and the investigating region) decreases, the number density of high mass haloes increases because it becomes easy for larger blocks to collapse. This tendency is emphasized in the case of $y = 1/2$ rather than $y = x$.

We believe that the MCM is a powerful tool for constructing merger trees of dark haloes because it includes the information of spatial correlations naturally and correctly as shown in this paper. For example, we applied the MCM to estimating the angular momentum distribution of dark haloes, including the information of velocity field, which is obtained by the spatial distribution of density fluctuations (Nagashima & Gouda 1998). In the MCM, the number of high mass haloes increases, relative to the results of previous works, *e.g.*, Kauffman et al. (1993) and Cole et al. (1994), so the number of giant, red elliptical galaxies may increase. In the MCM, however, a serious problem appears, *i.e.*, it is found that in taking into consideration the overlapping of dark haloes of non-zero size, the multiplicity function is sensitive to the choice of the overlapping criterion. Therefore, we must consider a more realistic overlapping criterion for constructing merger trees. We do not know *a priori* the value of the overlapping parameter. Furthermore the value of the overlapping parameter may not be constant as time passes. It might be a function of halo mass, of separation between a halo and a block, or some other parameter. It is a very difficult problem to identify the mass and size of the collapsed halo when several haloes are overlapped. However, it is very important to precisely identify the collapsed haloes for constructing the merger trees of haloes with good accuracy. As mentioned in Section 2.1, the merger tree of the dark haloes affects the various important processes for the formation and evolution of galaxies, such as the thermal history of gases, merging between galaxies and so on. Hence, it is necessary and important to understand how the overlapping criterion influences these processes.

Furthermore, we assume spherically collapse of the dark haloes. But, in fact, there is the possibility that the collapsed objects have filament or sheet structures. We must also deal with these cases in order to correctly estimate the merger trees. We are now investigating the merger tree models in which the effects of the spatial correlation and non-spherical collapse are included and the identification of the collapsed haloes is well defined. The strongest candidate

for this may be the adhesion model (e.g., Gurbatov et al. 1989; Vergassola et al. 1994), but it is difficult in the present situation to apply it to the semi-analytic model. It is also difficult to apply the MCM to the semi-analytic model because of the ambiguity of identifying the collapsing region and because of the restricted spatial resolution in our calculation. On the other hand, in spite of many theoretical uncertainties, the difference between the Press-Schechter mass function and the mass functions given by N-body simulations is only a few factor in the number of haloes. Therefore we use the block model or the extension of the PS model in the following chapter. Still we will be able to obtain some qualitative conclusions even by using the block model or the extension of the PS formalism. The improvement of the adhesion model for applying to the semi-analytic model will be done in future work.

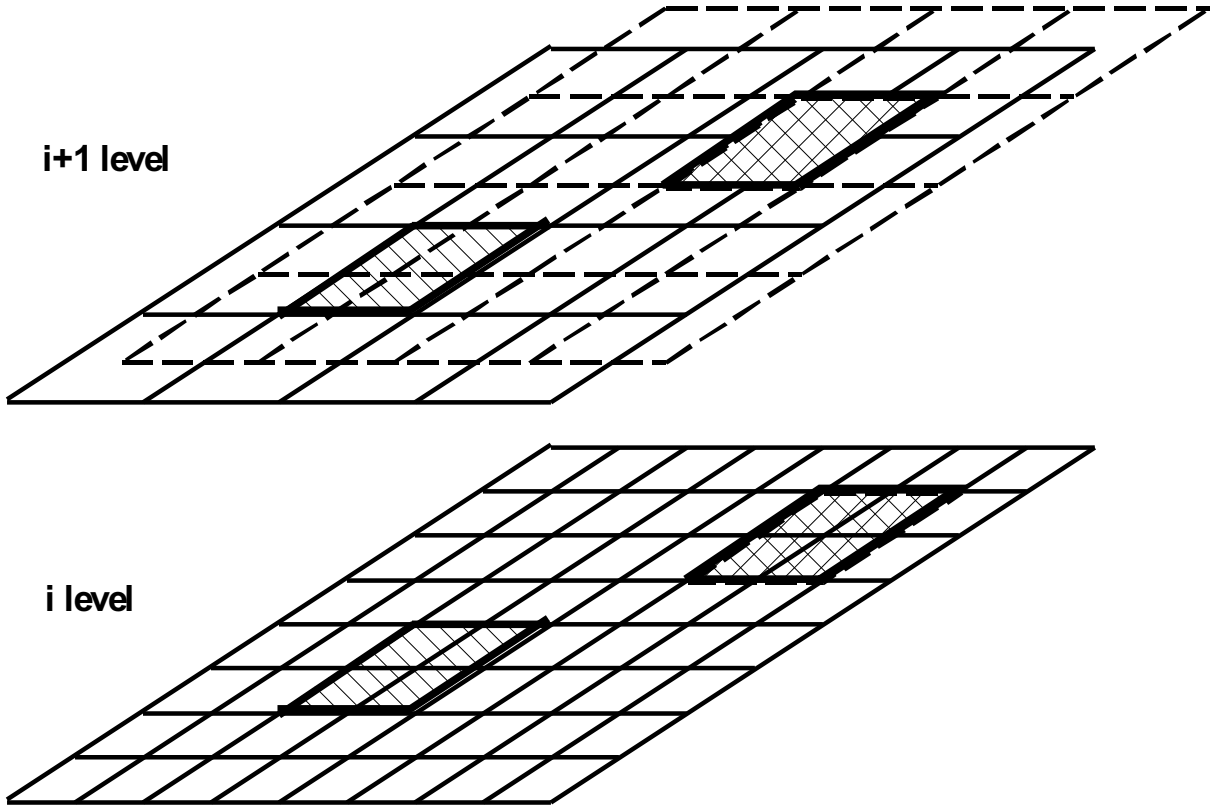


Figure 2.1: Scheme of averaging density fluctuations demonstrated in 2 dimensions (after Rodrigues & Thomas 1995). Lower grid represents i -th level. Upper grids represent $i + 1$ -th level with one of the overlapping grids displaced by half a blocklength. The hatched region in the lower grid is averaged to make a block at the $i + 1$ -th level and indicated as the region marked as a thick square in the upper grid. Blocks in the offset grid are averaged from the lower level in the same way.

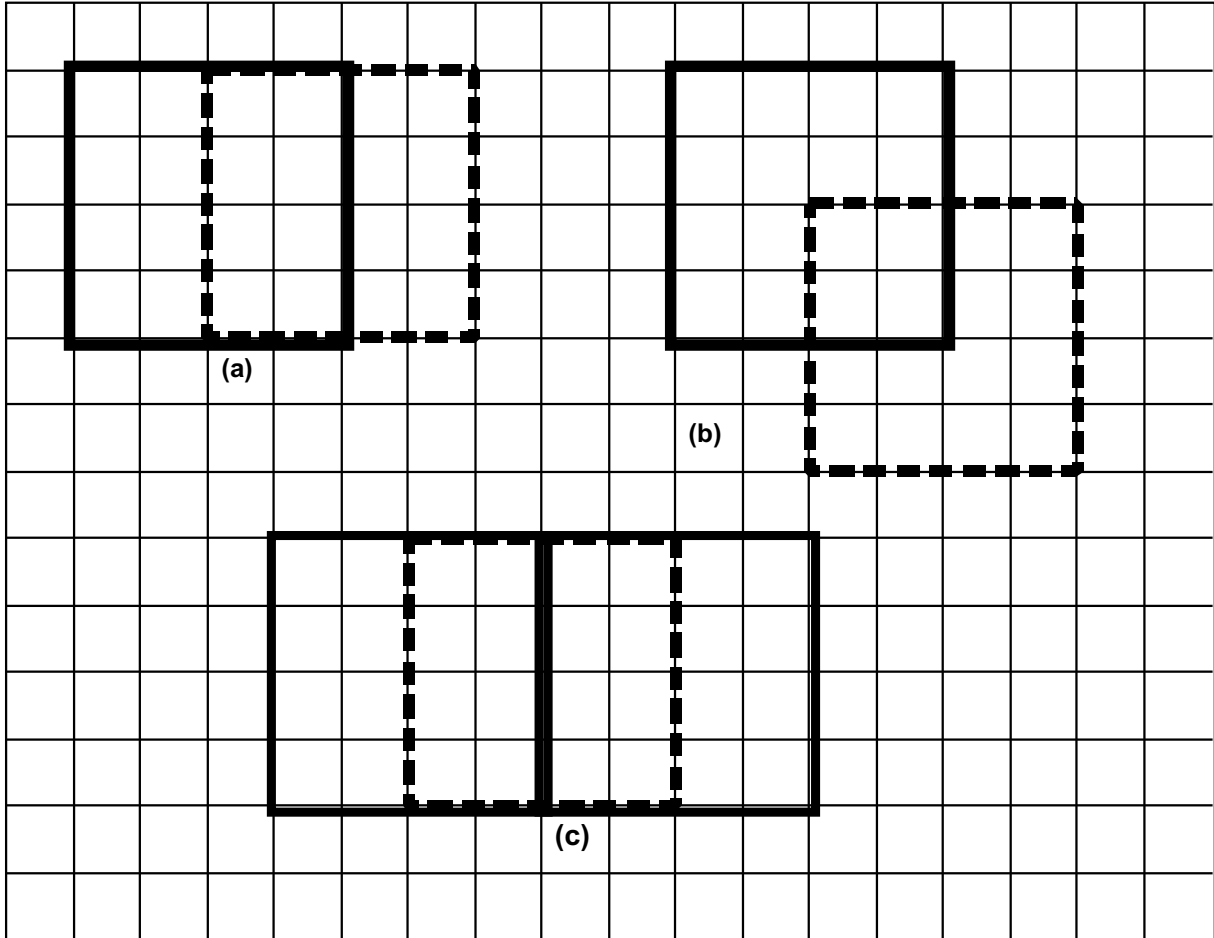


Figure 2.2: The overlapping criterion. The thick squares show haloes and the dashed squares show investigating regions. (a) The block can collapse and is merged into the halo because the overlapping region is larger than half of the lesser of the regions of the halo and the investigating region. (b) The block cannot collapse because the overlapping region is not larger than half of the lesser of the regions of the halo and the investigating region. (c) The linking criterion. In the case shown here, the block cannot collapse because we would like to prevent the growth of the long filamentary structure (see text). Note that it is equivalent to consider either regions or masses for the overlapping criterion.

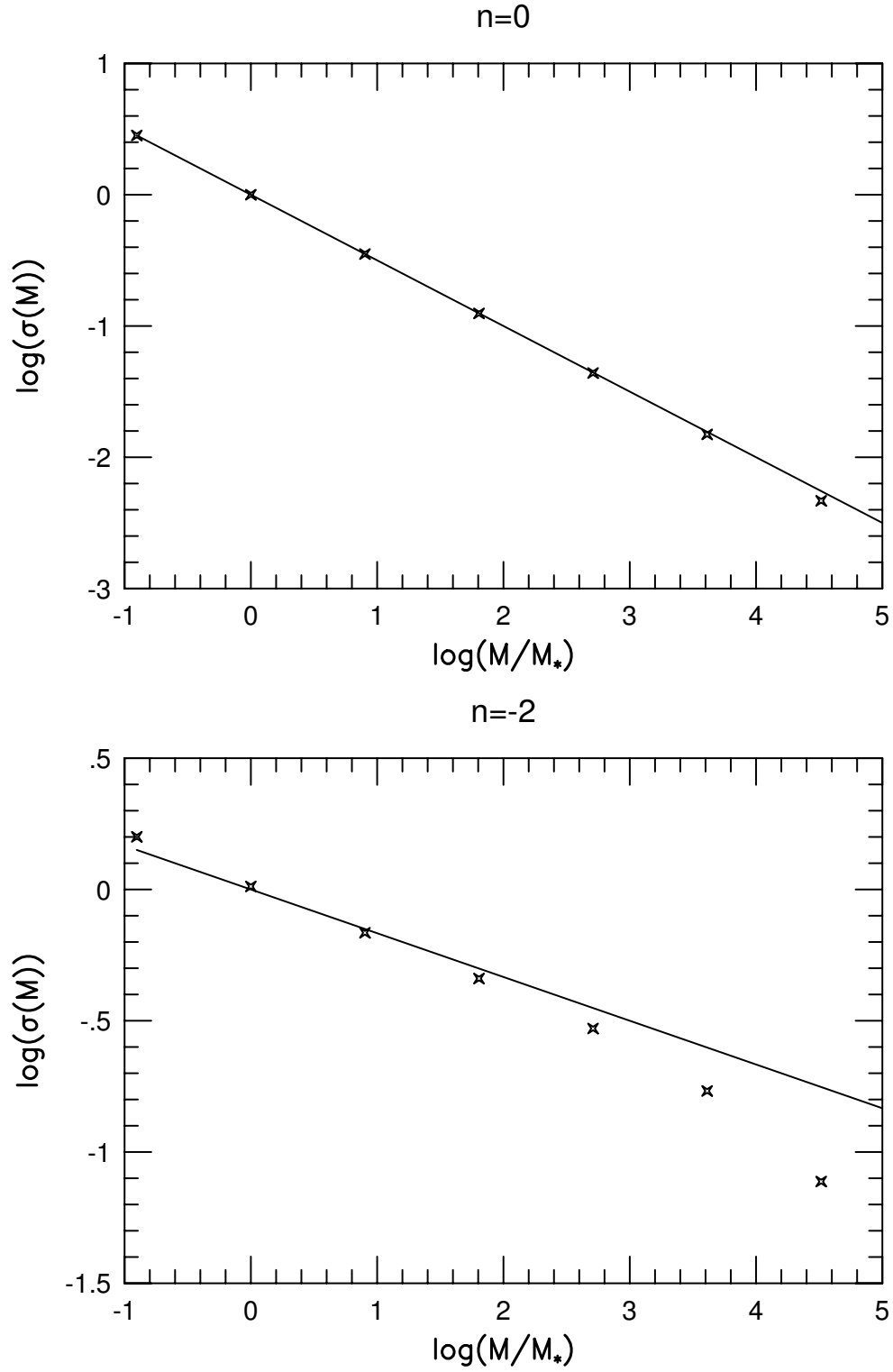


Figure 2.3: Mass spectrum: (a) spectral index $n = 0$, (b) $n = -2$. The crosses show the standard deviations on each smoothing mass scale in the MCM. The solid lines show the scale-free spectra which are adopted to calculate the mass functions by using Jedamzik formalism.

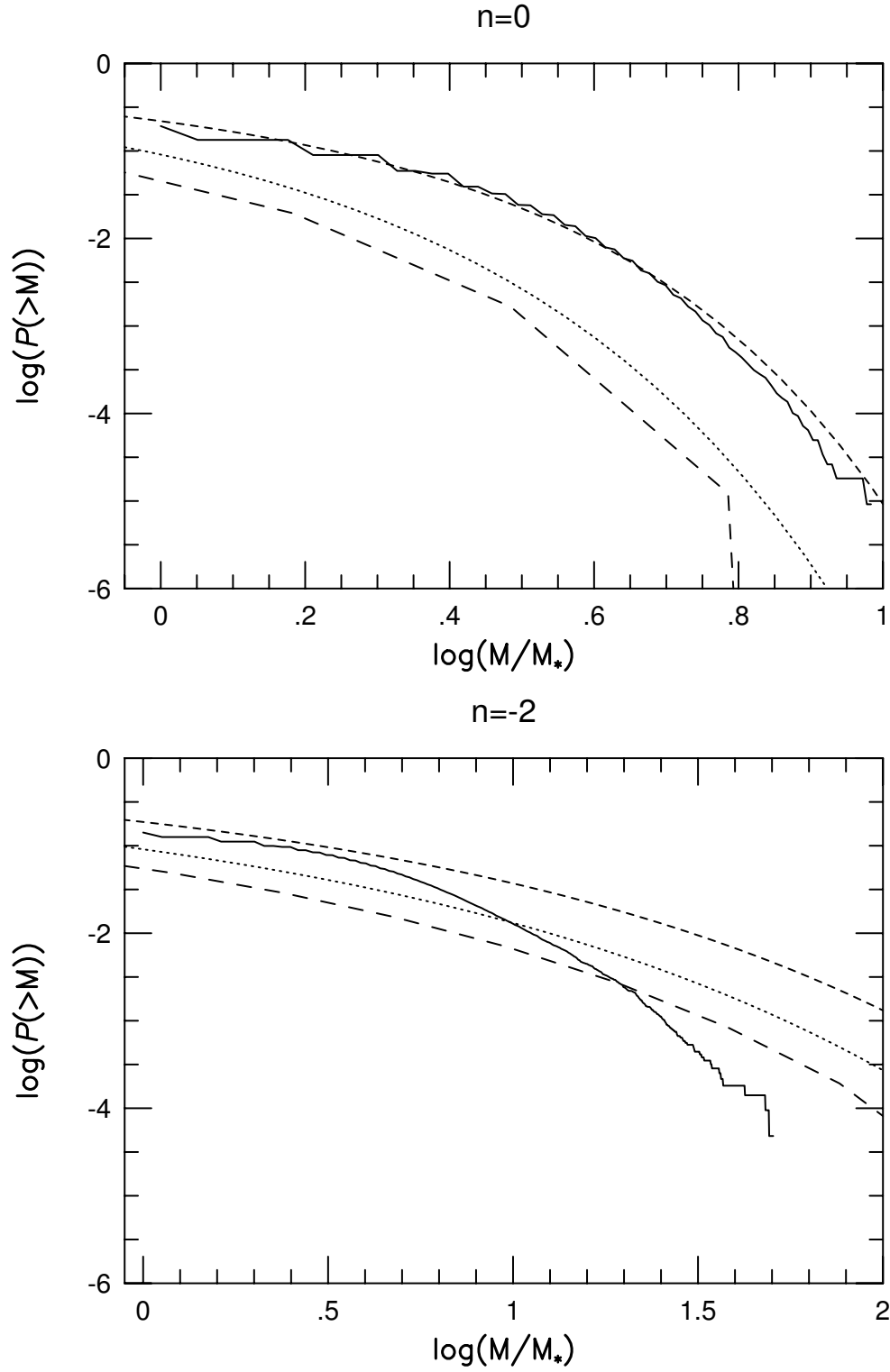


Figure 2.4: Cumulative multiplicity function: (a) spectral index $n = 0$, (b) $n = -2$. The solid lines, the short-dashed lines, the dotted lines and the long-dashed lines show the cumulative multiplicity functions given by the MCM averaged over four realizations, the YNG formula, the PS formula and the Block model averaged over five realizations, respectively.

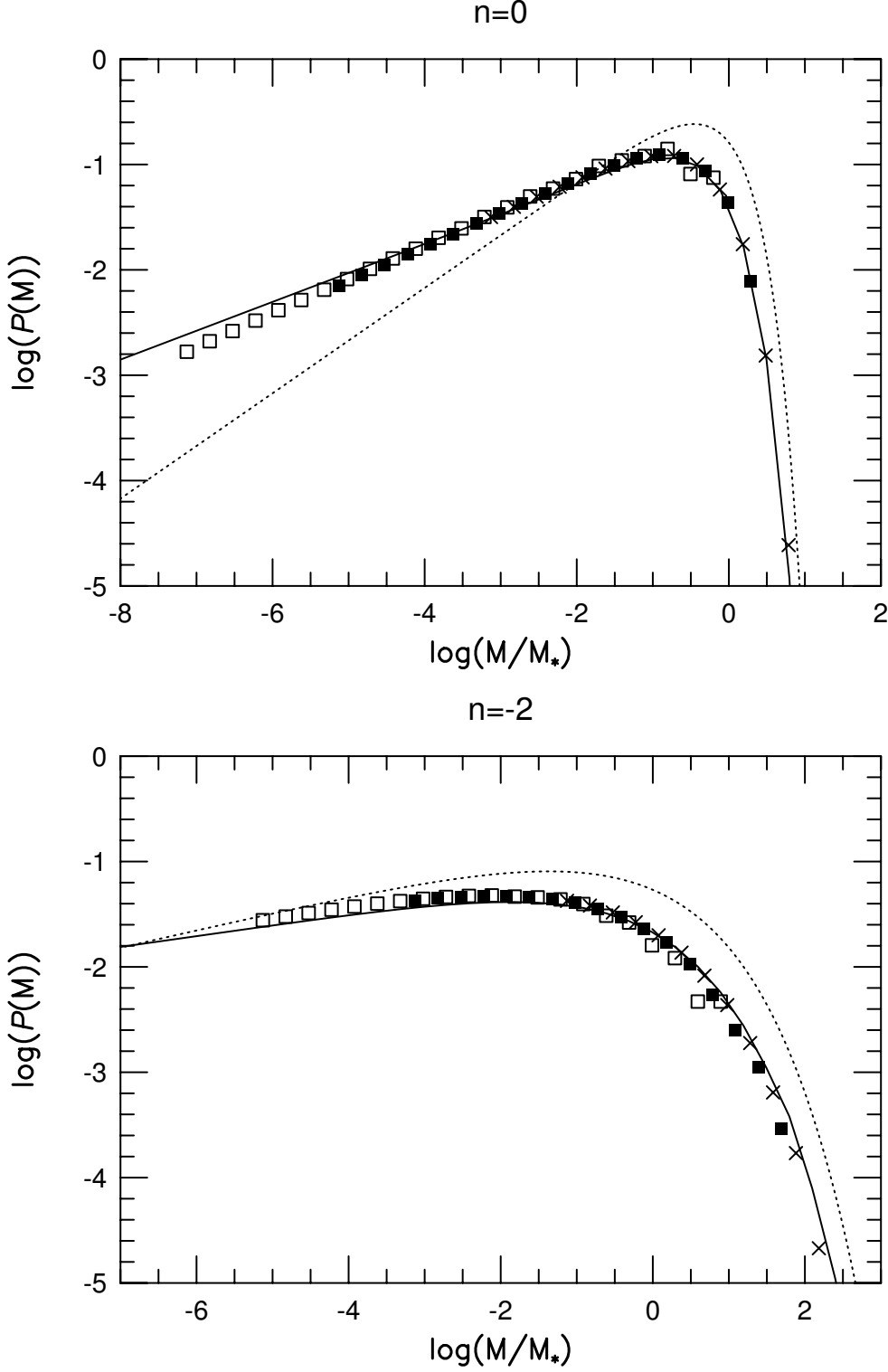


Figure 2.5: Block Model: (a) $n = 0$, (b) $n = -2$. Crosses, solid squares and open squares show the multiplicity functions averaged over five realizations of the Block model with the largest box size $M_0 = 10^5 M_*$, $10^3 M_*$ and $10 M_*$ in the case of $n = 0$ and $10^7 M_*$, $10^5 M_*$ and $10^3 M_*$ in the case of $n = -2$, respectively. The solid lines and the dotted lines show the predictions by using the Jedamzik formula and the PS formula, respectively.

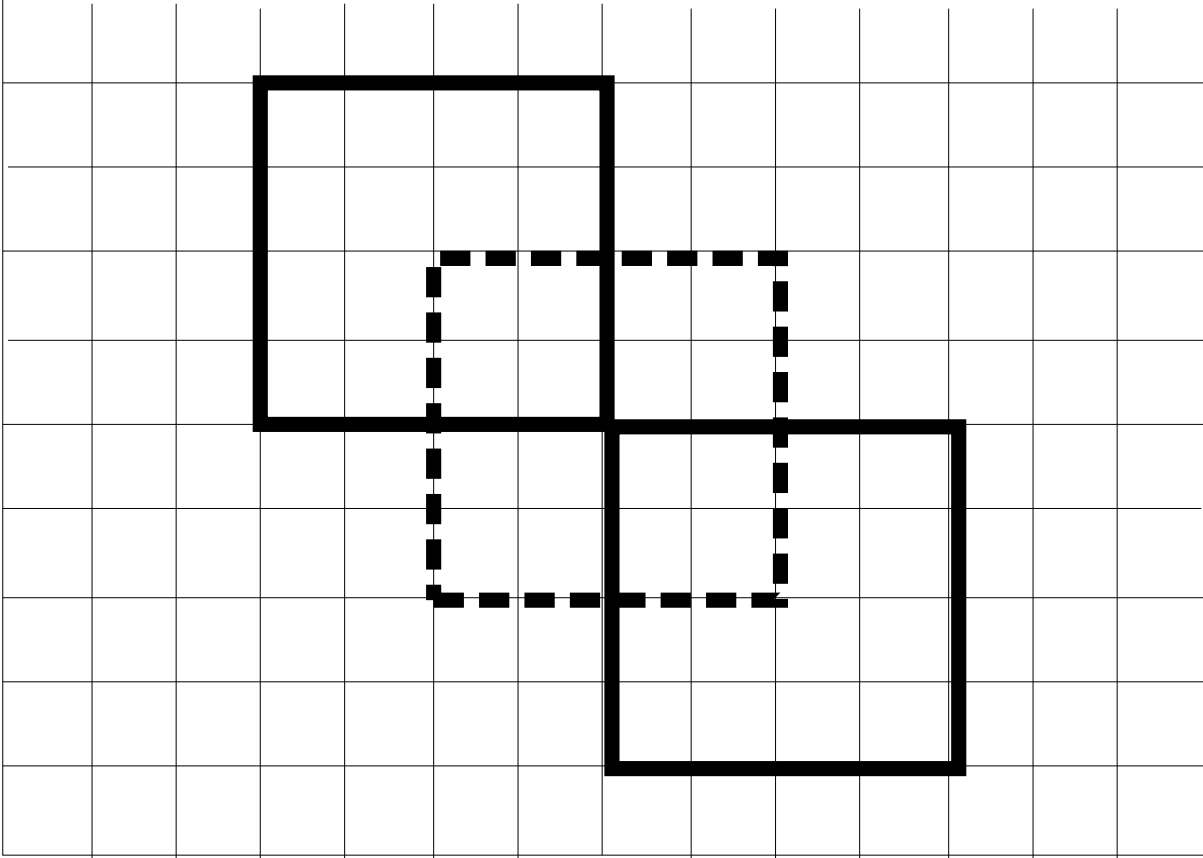


Figure 2.6: The linking criterion. The thick squares show haloes and the dashed square shows an investigating region. We consider the case of $x = 1/4$. The investigating region can collapse in the case of $y = 1/2$, while it cannot collapse in the case of $y = 1/4$ because the investigating region has $1/4$ of its mass contained in *two* pre-existing haloes.

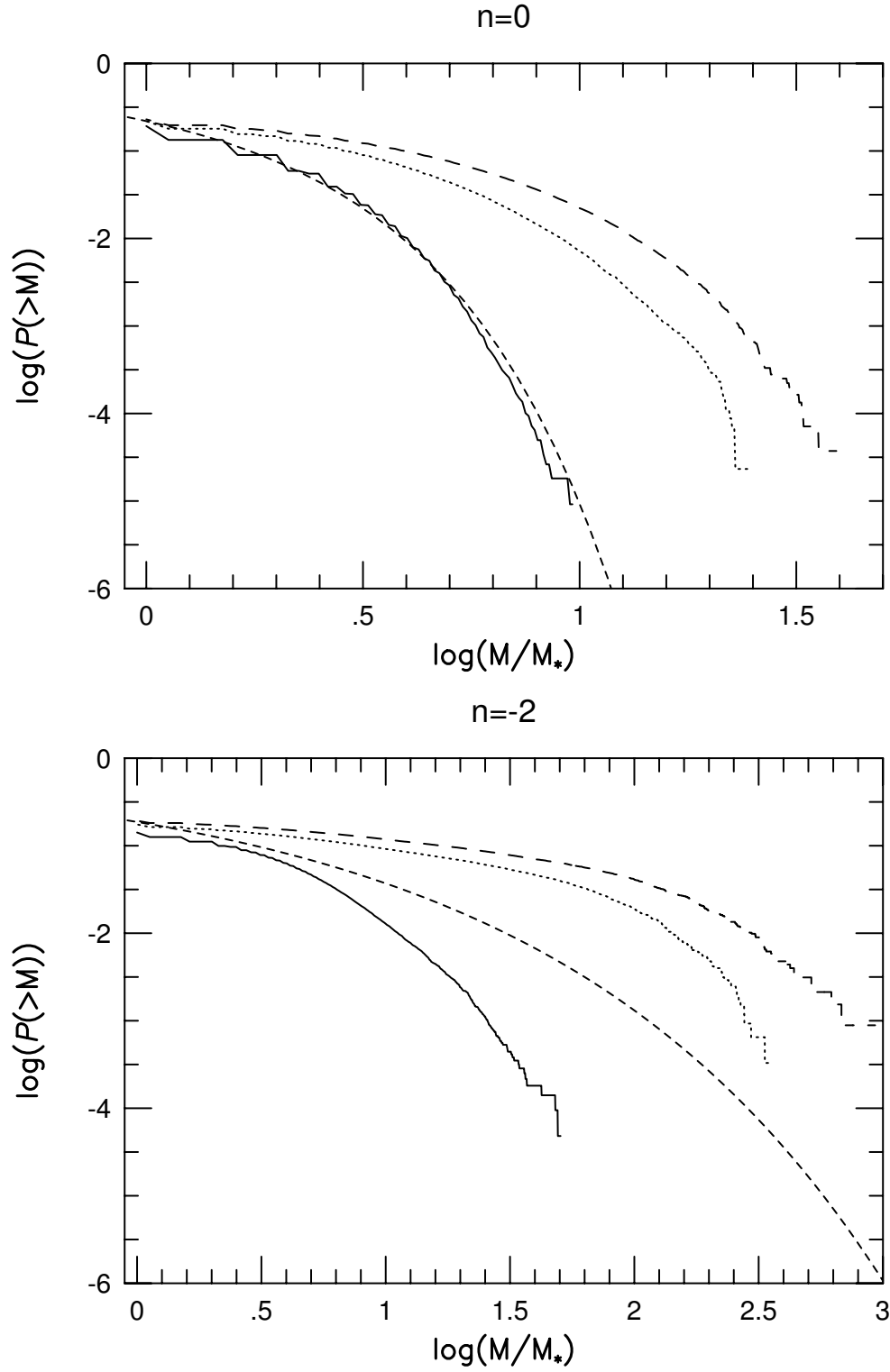


Figure 2.7: Effects of overlapping in the case of $y = 1/2$: (a) $n = 0$, (b) $n = -2$. The solid lines, dotted lines and long-dashed lines show the multiplicity functions averaged over four realizations given by the MCM with the overlapping criterion defined by $x = 1/2, 1/4$ and $1/8$, respectively. The short-dashed lines show the multiplicity functions given by the YNG formula.

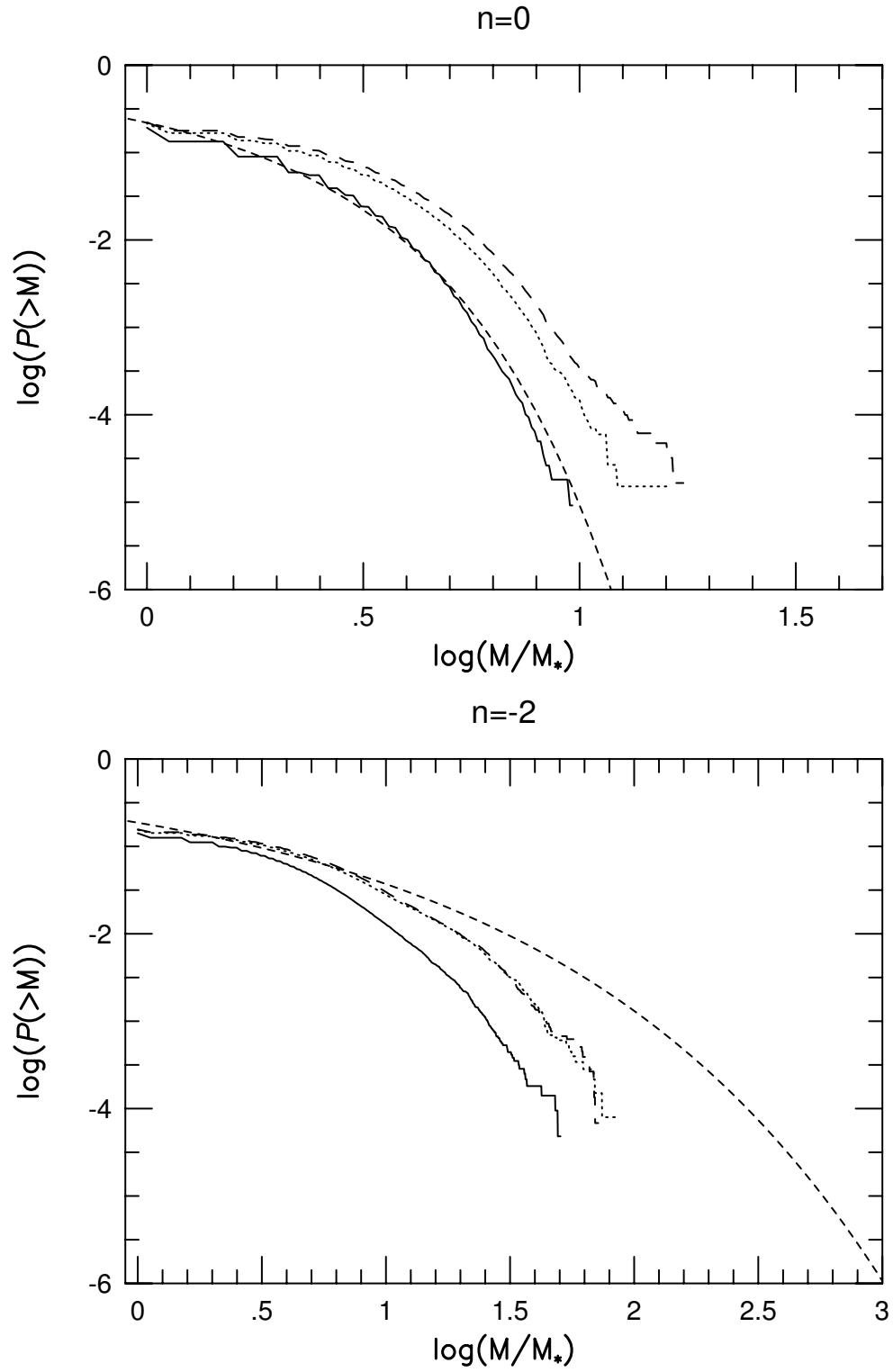


Figure 2.8: Same as Fig.2.6, but for $y = x$

Chapter 3

Semi-analytic modeling of the galaxy formation

3.1 INTRODUCTION

In this Chapter, we review some semi-analytic models.

As mentioned in Chapter 1, since the semi-analytic model includes some physical processes connected with the galaxy formation, it is easy to understand the galaxy formation process, in contrast to N-body and hydrodynamical simulations. Therefore we must include the following ingredients in our models at least: merging history of dark haloes, cooling and heating processes of baryonic gas, star formation and feedback by supernovae, mergers of galaxies, and stellar population synthesis model. The following procedure is mainly based on Kauffmann et al. (1993), Cole et al. (1994) and Somerville & Primack (1998).

The outline of the procedure is as follows. At first, the merging paths of dark haloes are realized by the extension of the PS formalism or the block model. Next, in each merging path, evolutions of the baryonic component, namely, gas cooling, star formation, and supernova feedback, are calculated. We recognize a system consisting of the stars and cooled gas as a *galaxy*. When two or more dark haloes merge together, there is a possibility that galaxies contained in progenitor haloes merge together. The judgment whether the galaxies merge together or not is usually based on the dynamical friction timescale. Here we define the *lifetime* of haloes as the elapsed time between the formation time of the halo and the time at which the halo is subsumed into a larger halo. If the dynamical friction timescale is shorter than the lifetime, the galaxies will merge. If not, the galaxies will not merge and the common dark halo has two or more galaxies. Finally, we calculate the colour and luminosity of each galaxy from the star formation history of each galaxy. Through the above procedures, we know the properties of each galaxy, and the statistical properties like luminosity function, colour distribution, and so on. The image of this procedure is shown in Fig.1.1.

3.2 MERGING HISTORIES OF DARK HALOES

The merging history models which have been used are mainly the extension of the PS formalism and the block model. As mentioned in Chapter 2, these models have some weak points. Porciani et al. (1998) consider the effect of the spatial correlation in their method for realizing merging paths approximately and phenomenologically. We are also now investigating the merger tree models in which the effect of the spatial correlation is included. However, as mentioned in Section 2.5, it is difficult in the present situation to apply them to the semi-analytic model. Moreover, in spite of many theoretical uncertainties, the difference between the Press-Schechter mass function and the mass functions given by N-body simulations is only a few factor in the number of haloes. This curiosity is reviewed by Monaco (1998). Therefore, for simplicity, we use the block model and the extension of the PS formalism in this thesis. The procedure by using the block model and the extension of the PS formalism is reviewed in Chapter 2.

In Chapter 2, we used the scale-free power spectrum, $P(k) \propto k^n$. In the following Chapter, we use the power spectrum in the CDM model in order to compare the results given by calculation with observation. This power spectrum is expressed by (Bardeen et al. 1986)

$$P(k) \propto kT^2(k), \quad (3.1)$$

$$T(k) = \frac{\ln(1 + 2.34q)}{2.34q} \left[1 + 3.89q + (16.1q)^2 + (5.46q)^3 + (6.71q)^4 \right]^{-1/4}, \quad (3.2)$$

$$q \equiv \frac{k}{\Omega h^2 \text{Mpc}^{-1}}. \quad (3.3)$$

We adopt the standard CDM model, $\Omega = 1$ and $h = 0.5$. We will study the dependence of the galaxy formation and evolution on the cosmological parameters in future work. In this thesis, fixing the cosmological model, we investigate how the galaxy formation and evolution depend on the baryonic processes.

In the following subsections, we often use circular velocity instead of mass. We know the specific gravitational energy of haloes via the circular velocity owing to the virial theorem. The circular velocity V_c of a halo with mass M is obtained by the virial theorem,

$$V_c^2 \simeq \frac{GM}{R}, \quad (3.4)$$

where R is the virial radius of the halo. When a halo forms, the relation between its mass and circular velocity is obtained by the virial theorem,

$$M = 2.35 \times 10^5 \left(\frac{V_c}{\text{km s}^{-1}} \right)^3 (1+z)^{-3/2} h^{-1} M_\odot, \quad (3.5)$$

where we use the spherical collapse model.

3.3 GAS COOLING

In each realized merging path, we evaluate the amount of cooled gas through the radiative cooling, that is a direct material for forming stars.

When a dark halo under consideration collapses, we estimate the mass of hot diffuse gas contained in the halo. The sources of the diffuse gas are hot gas contained in its progenitor haloes and in the accreting matter. The baryon fraction of the accreting matter is defined as Ω_b/Ω , where Ω_b is the cosmic mean baryon density. The density distribution $\rho(r)$ of this hot gas in the halo is assumed as the isothermal distribution. In this case, the density profile is represented by $\rho(r) \propto r^{-2}$, because the temperature $T(r) \propto M(\leq r)/r = \text{const.}$ and $M(\leq r) = \int_0^r 4\pi r'^2 \rho(r') dr' \propto r$. The absolute value of the density profile is determined by mass and collapsing redshift of haloes under the spherical collapse model.

The cooling timescale τ_{cool} is obtained as a function of the radius from the hot gas density profile, the temperature of the hot gas, and the cooling function $\Lambda(T)$ as follows,

$$\tau_{cool}(r) = \frac{3}{2} \frac{\rho(r)}{\mu m_p n_e^2(r)} \frac{kT}{\Lambda(T)}, \quad (3.6)$$

where μm_p is the mean molecular weight, $n_e(r)$ is the electron number density at the radius r , and k is the Boltzmann constant. The cooling function depends on the metallicity of the hot gas. We adopt the both cooling functions of zero-metallicity and solar-metallicity given by Sutherland & Dopita (1991), and determine the cooling efficiency depending on the metallicity of the gas from the two cooling functions by interpolation and extrapolation.

When a halo merges with another halo of comparable size (when the mass ratio of these haloes is larger than f_{reheat}), the diffuse hot gas contained in the halo is shock heated to the virial temperature of the halo. In this case, the hot gas within the *cooling* radius r_{cool} cools and the cooled gas mass is simply added to the cold gas reservoir of the galaxy. The cooling radius is a radius at which the cooling timescale equals to the time step Δt of the merging histories of dark haloes. On the other hand, when the halo merges with small haloes whose mass ratio to the halo is less than f_{reheat} , the hot gas is not shock heated and preserves its temperature, and the density profile is not disturbed. This parameter is introduced by Somerville & Primack (1998) firstly. In such a case, gas contained in the smaller haloes may remain in outer region of the new halo. Therefore, we introduce the following process when the mass ratio of the merging haloes is less than f_{reheat} . Now we define t_{elapse} as the elapsed time since the last shock heated epoch of the halo and $r_{cool}(t_{elapse})$ as a radius at which the cooling timescale equals to the elapsed time. In this case, because the density profile is maintained and the gas within $r_{cool}(t_{elapse})$ has already cooled, the cooled gas mass is estimated as

$$\Delta M_{cool} = \int_{r_{cool}(t_{elapse})}^{r_{cool}(t_{elapse} + \Delta t)} \rho(r) 4\pi r^2 dr. \quad (3.7)$$

This procedure is adopted only when $r_{cool}(t_{elapse})/R \leq 0.8$, because the hot gas may fall into the centre of haloes and cool if most of hot gas has already cooled at the previous time step, while the density profile of the dark halo will be preserved.

We can avoid the dependence of the amount of the cooled gas mass on the artificial time step of calculation by using the above procedure. In this thesis, we use $f_{reheat} = 0.2$. Of course, if we use the block model, this parameter is not required. In the extension of the PS formalism, masses of haloes are given by randomly and the time step is fixed. On the other hand, in the block model, density contrasts which determine the time step are given randomly,

while masses of haloes are divided by a factor of 2. So mass of a new collapsing halo is always twice of a maximum progenitor. Thus the mass ratio of the merging haloes are usually larger than $f_{reheat} = 0.2$.

In the case that the circular velocity of haloes exceeds 500 km s^{-1} , we prevent the cooling process by hand to suppress the formation of extremely big *monster* galaxies. If we consider only the mean density of the hot gas as discussed in Chapter 1, the maximum mass of galaxies is $\sim 10^{12} M_{\odot}$ (see Fig.1.3). In our calculation, since we adopt the isothermal distribution $\rho(r) \propto r^{-2}$, the cooling process becomes efficient in the central region of haloes. Actually this phenomenon is suggested observationally (e.g., Fabian 1994). However the number density of bright galaxies is much larger than the observed one, unless we prevent the cooling process in such large haloes. Thus we adopt the same unsatisfactory solution as Kauffmann et al. (1993). A detailed study is needed in order to understand this effect physically.

3.4 STAR FORMATION

In Kauffmann, White & Guiderdoni (1993), the star formation in disk is described by the following simple law,

$$\dot{M}_* = \frac{M_{cold}}{\tau_*}, \quad (3.8)$$

$$\tau_* = \tau_*^0 (1+z)^{-3/2}, \quad (3.9)$$

where eq.(3.8) denotes the rate of stars newly formed. This form is the same as the one adopted by Kauffmann et al. (1993), and referred as the ‘Munich model’ by Somerville & Primack (1998). The redshift dependence on the star formation timescale τ_* is obtained as follows. We adopt the simple star formation interpretation, $\tau_* \propto R/V_c$, that is, τ_* is proportional to the dynamical timescale. From this, the virial theorem and the spherical collapse model [eqs.(3.4) and (3.5)], we obtain that $\tau_* \propto (1+z)^{-3/2}$. The value of the star formation timescale at $z = 0$, τ_*^0 , is a free parameter. This parameter describes the star formation with a long timescale in a disk of spiral galaxies. Moreover we need to fit the amount of the cold gas in the ‘Milky Way’-like spiral galaxies, which have the same circular velocity as our Galaxy (Milky Way), $V_c \simeq 220 \text{ km s}^{-1}$, to the amount of the cold gas in our Galaxy. If τ_*^0 is small, all of the cold gas is transformed into the stars until the present epoch. So τ_*^0 is larger than a few Gyr.

Stars formed by the above process constitute a disk of galaxies. Star formation in a bulge occurs when two or more galaxies with comparable masses merge together (see Section 2.4). In this merging process, since the system is dynamically disturbed, star burst may occur. Then both stars formed in the burst and disk stars may fall into the central region of the galaxy and constitute the bulge. We describe this event by adopting very short star formation timescale.

Another modeling of star formation timescale, the ‘Durham model’ by Cole et al. (1993) is,

$$\tau_* = \tau_*^0 \left(\frac{V_c}{300 \text{ km s}^{-1}} \right)^{\alpha_*}, \quad (3.10)$$

where α_* is a new parameter. They adopt $\alpha_* = -1.5$ and $\tau_*^0 = 2 \text{ Gyr}$ from the result of numerical simulations by Navarro & White (1993).

Of course, the above star formation laws are oversimplified. In the present situation, stars are considered to be formed as follows. The star formation process may be determined by the local properties, such as density and temperature. If we consider only atomic cooling in our calculation, the gas cools until $\sim 10^4$ K. So we identify such gas cooled until $\sim 10^4$ K as the cold gas. However, the pressure of the gas is still too high to form stars. The cooling by molecules is needed to cool the gas lower than 10^4 K. Then the gas cools until a few K by the molecular cooling, and fragment into small clumps. These clumps evolve to stars. These processes are performed in molecular clouds, whose mass is about $10^6 M_\odot$. Therefore we must consider the processes of the molecular cooling and the fragmentation of the ‘cold’ gas ($\sim 10^4$ K). It is studied by considering the ensemble of molecular clouds to connect the star formation in molecular clouds with the global star formation properties in galaxies (Fujita 1998; Fujita & Nagashima 1998). These processes are very complicated, so we do not adopt them in our semi-analytic model, since the simplicity which is an important merit of this model will be lost.

3.5 SUPERNOVA FEEDBACK

When stars form, massive stars with short lifetime explode and heat up the surrounding cold gas. The number of supernovae per solar mass of stars formed is $\eta_{SN} \simeq 7 \times 10^{-3} M_\odot^{-1}$ for the Salpeter IMF (Salpeter 1955; see Section 3.7). The kinetic energy from a supernova, E_{SN} , is about 10^{51} erg. When a fraction ϵ of the released energy is used to heat up surrounding cold gas, the amount of this reheated gas is evaluated as

$$\Delta M_{reheat} = \epsilon \frac{4 \dot{M}_* \eta_{SN} E_{SN}}{5 V_c^2} \Delta t. \quad (3.11)$$

This feedback process has many uncertainties actually, and therefore we adopt a simple description (Cole et al. 1994),

$$\Delta M_{reheat} = \left(\frac{V_c}{V_{hot}} \right)^{-\alpha_{hot}} \dot{M}_* \Delta t \equiv \beta \dot{M}_* \Delta t, \quad (3.12)$$

where V_{hot} and α_{hot} are free parameters. Eq.(3.11), which is adopted by Kauffman et al. (1993) corresponds to $\alpha_{hot} = 2$, and Cole et al. (1994) used $\alpha_{hot} = 5.5$ in their fiducial model.

3.6 MERGERS OF GALAXIES

When two or more haloes merge together, the new common halo may have two or more galaxies. In that case, the galaxies will lose their energy due to dynamical friction, and then fall into a centre of the new common halo. Finally they may merge together as the case may be.

When a halo collapses, a central galaxy contained in the largest progenitor is identified as the central galaxy of the new common halo. The cooled gas described in Section 3.3 accretes to this central galaxy. Other galaxies are identified as satellite galaxies.

We calculate the elapsed time from the epoch at which each satellite galaxy was identified as *satellite*, namely, it was contained in a common halo not as a central galaxy but as a satellite

galaxy. When this elapsed time exceeds the dynamical friction timescale for the galaxies in the new common halo, the satellite merges with the central galaxy. The dynamical friction timescale is (Binney & Tremaine 1987)

$$\tau_{mrg} = \frac{1.17 R^2 V_c}{\ln \Lambda G M_{sat}}, \quad (3.13)$$

where R and V_c are the virial radius and circular velocity of the new common halo, respectively, M_{sat} is the total mass of a halo to which the satellite belonged as central galaxy, and $\ln \Lambda$ is the Coulomb logarithm, which is approximated as $\simeq \ln(1 + M_H^2/M_{sat}^2)$ (M_H is the mass of the common halo) (Somerville & Primack 1998). This description is used in Chapter 5.

In the 'Durham model', they adopt a simple description of the merger timescale as

$$\tau_{mrg} = \tau_{mrg}^0 \left(\frac{M_{halo}}{M_{sat}} \right)^{\alpha_{mrg}}, \quad (3.14)$$

where two new parameters τ_{mrg}^0 and α_{mrg} are introduced. In their model, τ_{mrg}^0 is a half of the age of the universe at the time when the halo forms. Furthermore $\alpha_{mrg} = 0.25$. This is adopted in Chapter 4.

In this thesis, we do not treat mergers between satellite galaxies for simplicity, which is described in Somerville & Primack (1998). There is a possibility that this effect changes some statistical properties of galaxies. This effect will be considered in future work.

When a satellite galaxy merges with a central galaxy, and moreover the mass ratio of the galaxies is larger than f_{bulge} , all stars of the satellite galaxy and disk stars of the central galaxy are incorporated with the bulge of the central galaxy. Then cold gases of both galaxies turn to stars in the bulge with a very short timescale ('star burst'). On the other hand, if the mass ratio of the galaxies is smaller than f_{bulge} , all stars of the satellite galaxy are incorporated with the disk of the central galaxy and the cold gas reservoir of the satellite merges with that of the central galaxy, and then disk stars are formed from the cold gas with the star formation timescale obtained from eq.(3.9). In this thesis, we adopt $f_{bulge} = 0.2$. This value is the same as that in Somerville & Primack (1998). They adopt this value for reproducing observational fractions of the number of galaxies of each morphology.

3.7 STELLAR POPULATION SYNTHESIS AND IDENTIFICATION OF MORPHOLOGIES

In order to compare our results with the observations such as the colour-magnitude relation for elliptical galaxies in clusters of galaxies (hereafter CMR), a stellar population synthesis model must be considered. Several groups make the stellar population synthesis code by considering the evolution of stars with various masses at almost all stages. In this thesis, the stellar population synthesis models by Bruzual & Charlot (1996) and by Kodama & Arimoto (1997) are used in Chapter 4 and 5, respectively. Luminosity and colour of stars cannot be theoretically estimated without uncertainties because the stellar evolution models themselves include the uncertainties. For example, as for the convection of stellar gas, we have only a phenomenological theory ('mixing length theory'). However, these models are adequate for

our purpose. Once we understand the properties of galaxies such as the CMR physically and qualitatively, even if the stellar population model is changed, we fit immediately our results with observations by changing parameters mentioned above.

Here we explain the initial mass function (IMF). The IMF $\phi(M)$ is defined by mass fraction of stars formed, and normalized as follows,

$$\int_{M_l}^{M_u} \phi(M) dM = 1, \quad (3.15)$$

where M_l and M_u are lower and upper limits of initial stellar mass, respectively. M_l is about $\sim 0.1M_\odot$ because nuclear burning must occur in luminous stars. M_u is determined by the condition of stability of stars. There are some uncertainties in estimating M_u , but it is usually considered as $60 \lesssim M_u/M_\odot \lesssim 120$. Moreover, to evaluate the shape of $\phi(M)$ is difficult. The models often used are proposed by Salpeter (1955), Miller & Scalo (1979), and Scalo (1986). The Salpeter's IMF is described as a single power law,

$$\phi(M) dM = AM^{-x} dM, \quad (3.16)$$

where the normalization constant A is determined by eq.(3.15), and $x = 1.35$. The other IMFs are not a single power law, but roughly the same as the Salpeter's IMF.

In the model of Bruzual & Charlot, the IMF of Scalo (1986) is adopted. They give some simple stellar populations (SSPs) with different metal abundances, but we only use the one with solar abundance in Chapter 4.

In the Kodama & Arimoto model, the IMF which we adopt is the Salpeter type with a slope of 1.35, and the mass range is $0.1M_\odot \sim 60M_\odot$. The range of stellar metallicity Z_* of SSPs is $0.0001 \sim 0.05$.

In section 3.4, we divide the stellar component into disk and bulge components. Morphology of each galaxy is determined by the B-band bulge-to-disk luminosity ratio (B/D). Simien & de Vaucouleurs (1986) showed that the Hubble type of galaxies correlates with the B-band B/D . In this paper, galaxies with $B/D \geq 1.52$ are identified as ellipticals, $0.68 \leq B/D < 1.52$ as S0s, and $B/D < 0.68$ as spirals, according to their results. It is shown that this method for classification reproduces observations well by Kauffmann et al. (1993) and Baugh, Cole & Frenk (1996).

Chapter 4

Effects of the UV background radiation on galaxy formation

4.1 INTRODUCTION

It is known that the intergalactic medium (IGM) is highly ionized through the Gunn–Peterson test (Gunn & Peterson 1965). Ultraviolet (UV) background radiation which ionizes the IGM also affects the galaxy formation processes by photoionizing gas clouds. The UV photons penetrate the gas clouds and heat up the gas, then star formation in the gas cloud is suppressed by the UV radiation. Therefore it is important to take into account the effects of the UV radiation when we consider the galaxy formation processes.

In previous work by using the semi-analytic models, the effect of the photoionization by the UV background has been neglected. In this Chapter, we show the luminosity function and the colour distribution of galaxies as the fundamental observational quantities to understand the galaxy formation process under the effect of the UV background.

The sources of the UV background radiation are considered to be mainly QSOs. From the observations of Ly α clouds and QSOs, the intensity of the UV background radiation is indirectly measured by the ‘proximity effect’ (Carswell et al. 1984; Bajtlik, Duncan & Ostriker 1988; Bechtold 1994; Kulkarni & Fall 1993; Williger et al. 1994; Giallongo et al. 1996; Lu et al. 1996). The evolution of the UV intensity at low redshifts ($z \lesssim 2$) is approximately proportional to $(1+z)^\gamma$, $\gamma \sim 4$ from the evolution of the QSO luminosity function (Pei 1995), while at high redshifts ($z \gtrsim 2$) the evolution of the UV background is not yet determined.

It has been pointed out that the UV background affects the galaxy formation (e.g., Dekel & Rees 1987). Babul & Rees (1992) and Efstathiou (1992) have discussed the suppression of star formation by the UV background in dwarf galaxies by considering the evolution of a single galactic gas cloud. Taking into account the photoionization process, the mass function of cooled objects has been calculated in the hierarchical clustering scenario by Chiba & Nath (1994). Their result is that the number density of massive galaxies decreases compared to the case of no UV background. This behavior is explained as follows. In the hierarchical clustering scenario, large clouds generally collapse later than small clouds. Since the mean density of a cloud is assumed to be about 200 times the cosmological background density at

the collapsing epoch (see, e.g., Peebles 1993), large clouds have a lower density than small clouds. Then the UV photons penetrate deeply into the large clouds and suppress the star formation, which leads to the decrease in the number density of the massive galaxies. However, mergers of galaxies actually occur in the hierarchical clustering model. If luminous galaxies are formed by the mergers of faint galaxies which could collapse at high redshift with little effects of the UV radiation, the number of such luminous galaxies is probably less affected by the UV background. Therefore, it is important to consider the merging history of galaxies in order to clarify the effects of the UV radiation.

As already mentioned in Chapter 1, the semi-analytic models including the merging history of each individual galaxy has been developed recently. It has been already confirmed that the averaged stellar age of each galaxy has an only weak correlation with the luminosity of each galaxy in the semi-analytic model (Kauffmann & Charlot 1998). This result would be inconsistent with the shape of the CDM mass spectrum unless the mergers occur, because there is a relationship determined by the mass spectrum between mass and collapsing epoch of haloes. This fact also motivates us to analyse the effects of the UV background on galaxy formation via a semi-analytic approach.

In this Chapter, we investigate the effects of the UV background radiation with a semi-analytic model, which is an extension of Cole et al. (1994) based on the block model for merging histories of dark haloes (Cole & Kaiser 1988; Nagashima & Gouda 1997, see Chapter 2) by including the photoionization process. In spite of some weaknesses in the block model as pointed out in Chapters 2 and 3, this model has an advantage, that is, the simplicity for use. Because the main aim of this Chapter is not to fit the parameters described in Chapter 3 to observations in detail but to understand the effect of the UV background on the galaxy formation, it is adequate for this aim to use the block model. We will show how the luminosity functions and the colour distributions of galaxies are changed by the UV background.

In Section 4.2, we describe our model. In Section 4.3, we show the luminosity function and the colour distribution of model galaxies, and their redshift evolution. Section 4.4 is devoted to conclusions and discussion.

4.2 MODEL

4.2.1 Semi-analytic model

We use the semi-analytic model, originally developed by Cole et al. (1994). As mentioned in Chapter 3, the model includes the following processes: merging histories of dark haloes, gas cooling and heating, star formation and feedback, mergers of galaxies, and stellar population synthesis. We include the effect of the UV background radiation in their original model. The parameters which we use are the same as the ‘fiducial’ model in Cole et al. (1994), except for the block masses and the stellar population model. The astrophysical parameters in the fiducial model are chosen by matching the bright-end of the observed B-band luminosity function. The cosmological parameters are specified as follows: $\Omega_0 = 1$, $\Lambda_0 = 0$, $H_0 = 50 \text{ km s}^{-1} \text{ Mpc}^{-1}$, $\sigma_8 = 0.67$ and $\Omega_b = 0.06$. We use two maximum block masses M_0 corresponding to $2 \times 10^{16} h^{-1} M_\odot$ and $\sqrt{2} \times 10^{16} h^{-1} M_\odot$ in order to avoid the influence of the artificial discreteness of masses of blocks, $M_i = M_0/2^i$. The number of the hierarchy is 24. We use the GISSEL96

provided by Bruzual & Charlot (1996) as the stellar population model. More details about the original model are found in Cole et al. (1994). The data we will show are averaged over 30 realizations by using each maximum block mass.

4.2.2 Photoionization and mass fraction of neutral core

The UV radiation permeates a gas cloud to a radius at which the ionization by the UV photons balances with the recombination of ions and electrons. For simplicity, we assume that the gas within the ‘cooling radius’ r_{cool} , at which the cooling time scale without UV radiation equals to the lifetime of the halo including the gas, cools and recombines rapidly. The lifetime of the halo is defined as the time between the collapse of the halo and its subsequent incorporation into a larger halo. In Cole et al. (1994), the cooled gas within r_{cool} is interpreted as the star-forming gas. When the UV background exists, however, the mass of the star-forming gas decreases by the penetration of the UV background. Then we estimate a radius r_{UV} at which the UV photons are perfectly absorbed. We assume that the intensity of the UV radiation begins to decrease at r_{cool} and vanishes at r_{UV} by absorption of the UV photons ($r_{UV} \leq r_{cool}$), and that the gas within r_{UV} is cooled and forms stars. With the ‘inverted’ Strömrgren sphere approximation, we obtain this radius r_{UV} by the following relation,

$$\int_{r_{UV}}^{r_{cool}} n_p(r) n_e(r) \alpha^{(2)}(T_{eq}) 4\pi r^2 dr = \pi (4\pi r_{cool}^2) 1.5 \times 10^5 J_{-21}, \quad (4.1)$$

where n_p and n_e are the proton and electron number densities respectively, $\alpha^{(2)}(T_{eq})$ is the recombination coefficient to all excited levels at a temperature T_{eq} , and J_{-21} is the normalized intensity of the UV radiation, $J \equiv J_{-21} \times 10^{-21}$ ergs cm⁻² s⁻¹ sr⁻¹ Hz⁻¹. Since the density distribution of the gas is assumed as isothermal ($\propto r^{-2}$), the above equation is solved as follows:

$$r_{UV} = r_{cool} \left[1 + \left(\frac{r_{cool}}{R} \right)^3 \frac{A(J_{-21}, T_{eq}, M)}{(1+z)^5} \right]^{-1}, \quad (4.2)$$

where

$$A(J_{-21}, T_{eq}, M) \equiv \frac{1.35 \times 10^6 \pi J_{-21}}{\alpha^{(2)}(T_{eq}) n_R^2 R(M)}, \quad (4.3)$$

where $R(M)$ is the virial radius of the dark halo with the mass M in the comoving coordinate, and n_R is the mean comoving baryon density within $R(M)$, which is about 200 times the cosmological background baryon density under the assumption of the spherical collapse.

In Fig.4.1, we plot the ratio r_{UV}/r_{cool} from the above function at various redshifts in the case of $J_{-21} = 0.1$, $R(M) = r_{cool}$ and $M_{baryon} = 0.06M$, where M_{baryon} is the baryon gas mass. Note that the curve at $z = 0$ almost coincides with the horizontal axis, that is, the UV photons penetrate into the vicinities of the centres of gas clouds. In our calculations shown in Section 3, r_{cool} is a function of the lifetime of haloes, which depends on their merging histories. It is assumed that $T_{eq} = 3 \times 10^4$ K. Since the mean density of clouds at the collapsing epoch, n_R , is equal to $200n_b$, where n_b is the cosmological background density, clouds are denser at high redshifts and so the UV photons are perfectly absorbed at outer region. Therefore there is little effect of the UV radiation at high redshifts. At all epochs, the smaller the gas cloud is,

the smaller the ratio r_{UV}/r_{cool} becomes, because the effect of the photoionization is enhanced in small clouds by $A(J_{-21}, T_{eq}, M) \propto J_{-21} R(M)^{-1} \propto J_{-21} M^{-1/3}$. Note that $n_R \simeq 200n_b$ is common to all mass objects which are just collapsed. We also show the cases of $J_{-21} = 0.01$ and 1 in order to see the effect of changing the intensity. It is found that the ratio r_{UV}/r_{cool} increases when J_{-21} decreases. Since the second term in the brackets of eq.(4.2) scales as $J_{-21}(1+z)^{-5}$, increasing J_{-21} corresponds to decreasing z .

It is reported that this inverted Strömgren sphere approximation is not so good when we solve the radiation transfer by including the dependence on the frequencies of the photons (Tajiri & Umemura 1998). They have found that the UV photons permeate the clouds far beyond the radius at the optical depth $\tau \sim 1$. In our calculations, we have also used a criterion which has the same dependence on mass and UV intensity as the criterion by Tajiri & Umemura (1998) as a trial. We define the critical density n_{crit} as the density corresponding to the radius r_{UV} at which UV photons are perfectly absorbed, as follows:

$$n_{crit} \simeq 10^{-2} \text{cm}^{-3} \left(\frac{M}{10^8 M_{\odot}} \right)^{-1/5} J_{-21}^{3/5}. \quad (4.4)$$

This critical density is almost the same as given by Tajiri & Umemura (1998). We have found that the results are qualitatively the same as those by using the inverted Strömgren sphere approximation. However, they assume the homogeneous density cloud instead of the isothermal sphere exposed to the UV radiation. Therefore we cannot obtain the exact criterion for the isothermal sphere from their work.

Moreover, r_{UV} may become much smaller if we consider the condition under which H_2 molecules can be formed. So the criterion that the gas temperature becomes 10^4K for forming stars may be inadequate (Susa, private communication).

Anyway, it is difficult at present to fix a reasonable criterion for star formation under the photoionization effect of UV radiation. Thus, we will proceed as follows. First, note that assuming a smaller r_{UV} corresponds to an increasing intensity of J_{-21} . Then, as a trial, we investigate the effect of the photoionization by changing the value of J_{-21} instead of changing the criterion of star formation. Hereafter we study the both cases of $J_{-21} = 0.1$ (*weak condition*) and $J_{-21} = 10$ (*strong condition*).

4.2.3 UV background radiation

There are many uncertainties in the determination of the evolution of the UV background, though it is suggested that the intensity of the UV background rapidly declines at low redshifts ($z \lesssim 2$) as mentioned in the introduction. In order to take into account possible evolutions of the UV background, we calculate the following cases: (1) no UV background exists, (2) $J_{-21} = 0.1$ or 10 for $0 \leq z \leq 5$, (3) $J_{-21} = 0.1$ or 10 for $2 \leq z \leq 5$, and (4) $J \propto (1+z)^{\gamma}$, where $\gamma = 4$ for $z \leq 2$ and $\gamma = -1$ for $z \geq 2$, and $J_{-21} = 0.1$ or 10 at $z = 2$. Case (4) is probably the most realistic among these four cases. We show these models in Fig.4.2.

4.3 RESULTS

4.3.1 Luminosity function

Weak condition

In Figs.4.3a and 4.3b, we show the B- and K-band luminosity functions of model galaxies, respectively. The solid lines, the dotted lines, the short-dashed lines, and the long-dashed lines show cases (1), (2), (3), and (4) for the weak condition. The B-band data are taken from Loveday et al. (1992) and converted from their observed b_J to Johnson B by $B = b_J + 0.2$. The K-band data are those from Mobasher, Sharples & Ellis (1993). Because these data also have been used in Cole et al. (1994), a direct comparison of our results with the results in Cole et al. (1994) becomes easier.

We also show the redshift evolution of the B-band luminosity functions in the galaxies' rest frame in Figs.4.4. The types of lines are the same as Figs.4.3. The K-band luminosity functions are not shown, because their properties of the redshift evolution are almost the same as those of the B-band luminosity functions. The output redshifts are (a) $z = 0$, (b) $z = 0.4$, (c) $z = 1$, and (d) $z = 2$. At $z = 2$, the lines for case (2) are in agreement with those for case (3) by their definitions.

The differences between luminosity functions for various cases become small at high redshifts. This is considered as follows. At high redshifts $z \gtrsim 2$, mergers of galaxies occur frequently, so that the lifetime t_{life} becomes very short. This leads to a small cooling radius r_{cool} , and so this effect results in the same effect as the reduction of the UV intensity, because the effect of the photoionization emerges via the form $(r_{cool}/R)^3 J_{-21}$ from eq.(4.2). Therefore such merging galaxies are slightly affected by the UV background at $z \gtrsim 2$.

We find that the UV background hardly affects the galaxy formation in the weak condition. The number density of faint objects decreases slightly in cases (2) and (4), because the UV background affects small galaxies more strongly. However these differences from case (1) are within the observational errors. Thus we cannot distinguish characters of the evolution of the UV background by observing the present luminosity functions when the UV intensity is weak.

Strong condition

In the strong condition, the differences between luminosity functions for various cases are larger than the observational errors (Figs.4.5 and 4.6). Here, we see the properties of luminosity functions for various cases of the UV background in the strong condition.

Merger effect of galaxies In order to investigate the effect of galaxy mergers, we compare the luminosity functions for case (1) to those for case (2). In Figs.4.5, we show the same figures as Figs.4.3, but for the strong condition. The number of faint objects ($M_B - 5 \log(h) \simeq -18$) decreases about a factor of 7.5 in case (2), compared to case (1). On the other hand, the most luminous galaxies are less affected by the UV background, although their number slightly decreases.

In Chiba & Nath (1994), the characteristics of luminosity (mass) functions when the UV background exists are opposite to ours, that is, the number of dwarf galaxies is not affected

by the UV background, while the formation of massive galaxies is much suppressed in their results. This is because in our calculation the luminous galaxies are formed in high density regions and formed by mergers of small galaxies formed at early epochs owing to the high density environments, at which there is only little effect of the UV background because of the high density of gas clouds (see Fig.4.1). On the other hand, since most of dwarf-scale galaxies at high redshifts are merged into luminous galaxies until the present epoch, dwarf galaxies at present are formed at low redshifts compared with the typical epoch estimated from the power spectrum of density fluctuations, so that such dwarf galaxies are much affected by the UV background and their number decreases.

In Figs.4.6, at all redshifts, the number of faint galaxies is small in case (2), besides the number of luminous galaxies is also small at the low redshifts. This is because the number of progenitors of such luminous galaxies at high redshift is smaller than that in case (1). Therefore even the most luminous galaxies slightly become faint. Thus the number of the most luminous galaxies seems to decrease slightly.

Delayed formation of galaxies Here we consider case (3). When the UV radiation ceases at $z = 2$, the number of galaxies at present does not change compared to the case of no UV radiation. Therefore if the UV background vanishes at $z = 2$, we cannot distinguish the types of the evolution of the UV background from the luminosity function at $z = 0$ (Figs.4.5).

After the UV background vanishes at $z=2$ in case (3), the number of galaxies increases rapidly and its luminosity function shows good agreement with case (1) at $z \lesssim 0.4$ (Figs.4.6). This increase occurs similarly over the entire range of magnitudes. This means that the epoch of galaxy formation is delayed as a whole by the UV background (Babul & Rees 1992).

Effect of mass dependence of photoionization Now we consider case (4). In this case, the intensity of the UV background evolves continuously, so that the epoch when clouds become free from the effect of the UV background at low redshifts depends on their mass, and the epoch when massive clouds become free from the UV background is earlier than that of small clouds (see Fig.4.1).

It is interesting that the number density of faint galaxies in case (4) is in agreement with that in case (2), while the number density of luminous galaxies in case (4) is in agreement with that in case (1) (Figs.4.5). In case (4), as the UV intensity decreases after $z = 2$, massive clouds become free from the UV background and begin to form stars earlier than small clouds, so that the number of galaxies with $M_B - 5 \log(h) \lesssim -18$ increases. Thus the effect of the UV background remains only in small galaxies.

Next, we see the redshift evolution of luminosity functions (Figs.4.6), in order to investigate the effect of the mass dependence in more detail. Because in this case the UV background exists before $z = 5$ and is strong enough to ionize gas clouds at $z \geq 5$, the number of faint galaxies at $z = 2$ is smaller than that in cases (2) and (3). Note that minimum mass blocks begin to collapse at $z \sim 10$ in our model.

At $z = 2$, the number of galaxies with intermediate magnitude $M_B - 5 \log(h) \lesssim -18$ for case (4) is in agreement with that for case (2). At $z = 0.4$, the number of such galaxies for case (4) increases rapidly compared to that for case (2), although the number of faint

galaxies ($M_B - 5 \log(h) \gtrsim -18$) is nearly constant. This shows that galaxies with magnitude $M_B - 5 \log(h) \lesssim -18$ become free from the UV background and begin to form stars at $z \sim 0.4$.

Note that when the UV background vanishes completely as for case (3), the difference of the epoch at which the galaxies become free from the UV background depending on the mass of galaxies in the photoionization effect does not occur. Therefore, the mass dependence of the epoch at which clouds become free from the UV background and begin to form stars in the continuously decreasing UV field can be a physical mechanism that shallows the slope at the faint end of the luminosity function, as is favoured by observation.

From Figs.4.3~4.6, the luminosity function in case (4) seems to be closer to the observational one than in case (1) for $0.1 \lesssim J_{-21} \lesssim 10$ under the assumption that our criterion of star formation is correct.

4.3.2 Colour distribution at $z = 0$

In Figs.4.7a and 4.7b, we show the B-K colour distributions of galaxies in the weak condition for dwarf galaxies ($-19.5 \leq M_B \leq -17$) and for luminous galaxies ($M_B \leq -19.5$), respectively. The types of lines are the same as Figs.4.3. The dotted histograms are the observational data by Mobasher et al. (1986), which are normalised by the total number of observed galaxies.

In the weak condition the difference between the lines is small as for the difference between the luminosity functions for our four models shown in Figs.4.3. In case (2), the colour at the peak of the distribution of faint galaxies becomes redder slightly, because of the suppression of star formation at low redshifts. On the other hand, we cannot find any significant differences in the colour distributions of luminous galaxies.

In Figs.4.8, we show the same figures as Figs.4.7, but for the strong condition. In Fig.4.8a, the colour at the peak of the distribution in case (2) becomes redder than that in the case of no UV radiation, because star formation at low redshifts is suppressed by the photoionization. When the UV radiation ceases at $z = 2$ in case (3), the colour becomes bluer than that in the case of no UV radiation, because stars are newly formed after the UV radiation vanishes. In case (4), the colour distribution becomes much broad. This is because the epoch at which stars can be formed depends on the mass of objects when the UV intensity continuously decreases at low redshifts, as mentioned in the previous subsection (see Fig.4.1).

On the other hand, the colour distributions for luminous galaxies are not affected so much by the UV radiation, because of the mergers of galaxies as mentioned in the previous subsection (Fig.4.8b). We find, however, that the distributions have two peaks in cases (2) and (4). The reason that one of the peaks is bluer than the peak of the faint galaxies (Fig.4.8a) is that massive objects store hot gas which cannot be turned into stars in the progenitors. Such massive objects which are formed by mergers of small progenitors can form stars at low redshifts with little effect of the UV radiation. Luminous galaxies whose progenitors collapse at high redshift when the effect of the UV background is negligible make the other peak at the redder colour (see Section 4.3.1).

4.3.3 Evolution of colour distributions

In Figs.4.9 (the weak condition) and 4.10 (the strong condition), we show the redshift evolution of the colour distribution of galaxies in the galaxies' rest frame for cases (1) and (4). The solid lines, the dotted lines, the short-dashed lines, and the long-dashed lines denote the distributions at $z = 0, 0.4, 1$, and 2 , respectively. The thin lines and the thick lines show the cases (1) no UV, and (4) continuously evolving UV intensity. Figs.4.9a and 4.10a show the distributions for faint galaxies ($-19.5 \leq M_B \leq -17$), and Figs.4.9b and 4.10b for luminous galaxies ($M_B \leq -19.5$).

In Fig.4.9a, the difference between cases (1) and (4) becomes slightly larger at lower redshifts. As mentioned in Section 3.1.2.3, at high redshifts $z \gtrsim 2$, mergers of galaxies occur frequently, so that the UV intensity becomes effectively small. Therefore such merging galaxies are slightly affected by the UV background. Thus the distributions at high redshifts are those for these merging galaxies. Besides, since colours of galaxies do not depend on their luminosity but on their stellar ages, the colours of galaxies at high redshifts are little affected by the UV background, while the number of galaxies decreases when the UV background exists. On the other hand, at low redshifts, the hot gas photoionized by the UV photons at $z \sim 2$ begins to cool and form stars. Therefore, the distributions at low redshifts broaden to blue side, compared to case (1). These properties are more remarkable in the case of the strong condition (Fig.4.10a). Note that we do not consider the chemical evolution process in this Chapter, so that the colour reflects the epoch of the major star formation in each galaxy.

In Figs.4.9b and 4.10b, we also see the same properties as Figs.4.9a and 4.10a. The differences between the distributions in cases (1) and (4) for the luminous galaxies are smaller than those for the faint galaxies. The distributions for faint galaxies have longer tails toward blue side than those for luminous galaxies, because the fractions of young stars in such faint galaxies are larger than those in luminous galaxies. Thus we find that the effect of the UV background on faint galaxy formation remains until later epochs than that on luminous galaxy formation (see Section 3.1.2.3). This also arises from the fact that the UV background less affects massive haloes.

4.4 CONCLUSIONS AND DISCUSSION

We investigate the effects of the UV background radiation on galaxy formation with a semi-analytic model, which is an extension of Cole et al. (1994) by including the photoionization process. We find that the UV background radiation mainly affects low-mass objects corresponding to dwarf galaxies.

If the UV radiation field exists until the present epoch (case 2), the number of dwarf galaxies at present becomes small. In the hierarchical clustering scenario, dwarf-scale galaxies are statistically formed at high redshifts, and such galaxies are merged into luminous objects. Therefore dwarf galaxies at present are formed at low redshifts. Thus, when the effect of the UV background is strong, the star formation in such dwarf galaxies is suppressed by the UV radiation. On the other hand, luminous galaxies are less affected, because such luminous galaxies are formed in high overdensity regions and formed at high redshift owing to the high overdensity environments when the effect of the UV radiation is negligible. This represents that it is much important to consider mergers of galaxies.

When the UV radiation vanishes at $z = 2$ (case 3), the number of dwarf galaxies hardly changes but the colour becomes bluer because baryonic gas in clouds recombines and begins to form stars after the UV radiation field vanishes. These blue galaxies might be related to the ‘*faint blue galaxies*’ (e.g., Ellis 1997).

More realistically, in the case that the UV background evolves as $(1+z)^\gamma$, where $\gamma = 4$ for $z \leq 2$ and $\gamma = -1$ for $z \geq 2$ (case 4), the slope of the luminosity functions in the faint-end becomes gentler and closer to the observed one, compared to that in the case of no UV background. The reason why the slope changes is considered as follows. When the UV intensity declines after $z = 2$, large clouds become free from the effects of the UV background at relatively high redshifts, while small objects are affected until low redshifts. Therefore the number of galaxies with intermediate magnitudes ($M_B - 5 \log(h) \lesssim -18$) increases, compared to the case that the UV background exists with a constant intensity until the present epoch. Thus the effect of the UV background remains in only small galaxies. Similarly, the colour distribution becomes very broad because the epoch at which stars can be formed in the decreasing UV radiation field differs according to the mass of the haloes.

We also show the redshift evolutions of the luminosity functions and the colour distributions. If the UV intensity is sufficiently strong ($J_{-21} \gtrsim 1$), the difference between the evolutions of the UV background clearly appears in the difference between the evolutions of the luminosity function. Moreover, because the effect of the photoionization depends on the mass of galaxies, we obtain much information about the properties of the UV background from the colour distributions for different classes of absolute magnitudes of galaxies.

Although our knowledge of processes of the galaxy formation and the nature of the UV background is far from complete at present, it is certain that, when observations of evolutions of luminosity function and colour distributions are realised, as well as observations of the evolution of Ly α clouds, in the near future, they will play a significant role in investigating the evolution of the UV background and its effects on galaxy formation. Thus we believe that it is a powerful tool for investigating the evolution of the UV background to observe the redshift evolutions of the luminosity function and the colour distribution of galaxies.

It should be noted that our conclusion is contrary to the conclusion of Chiba & Nath (1994). They have reported that the number of massive galaxies becomes small by the UV radiation field. This difference results from considering the mergers of galaxies. We emphasize that we must construct a galaxy formation model including the mergers of galaxies, because the epoch of the formation of luminous galaxies is not the same as the epoch of the formation of stars in the luminous galaxies.

At the present moment, we do not know the exact criterion for forming stars with the UV radiation. In order to study the galaxy formations more quantitatively, we have to investigate the criterion for forming stars when the UV background exists in detail, and also the dependence on the merging history model and the other parameters in the model. We will also include the chemical evolution process in order to compare our results with the observations in the near future.

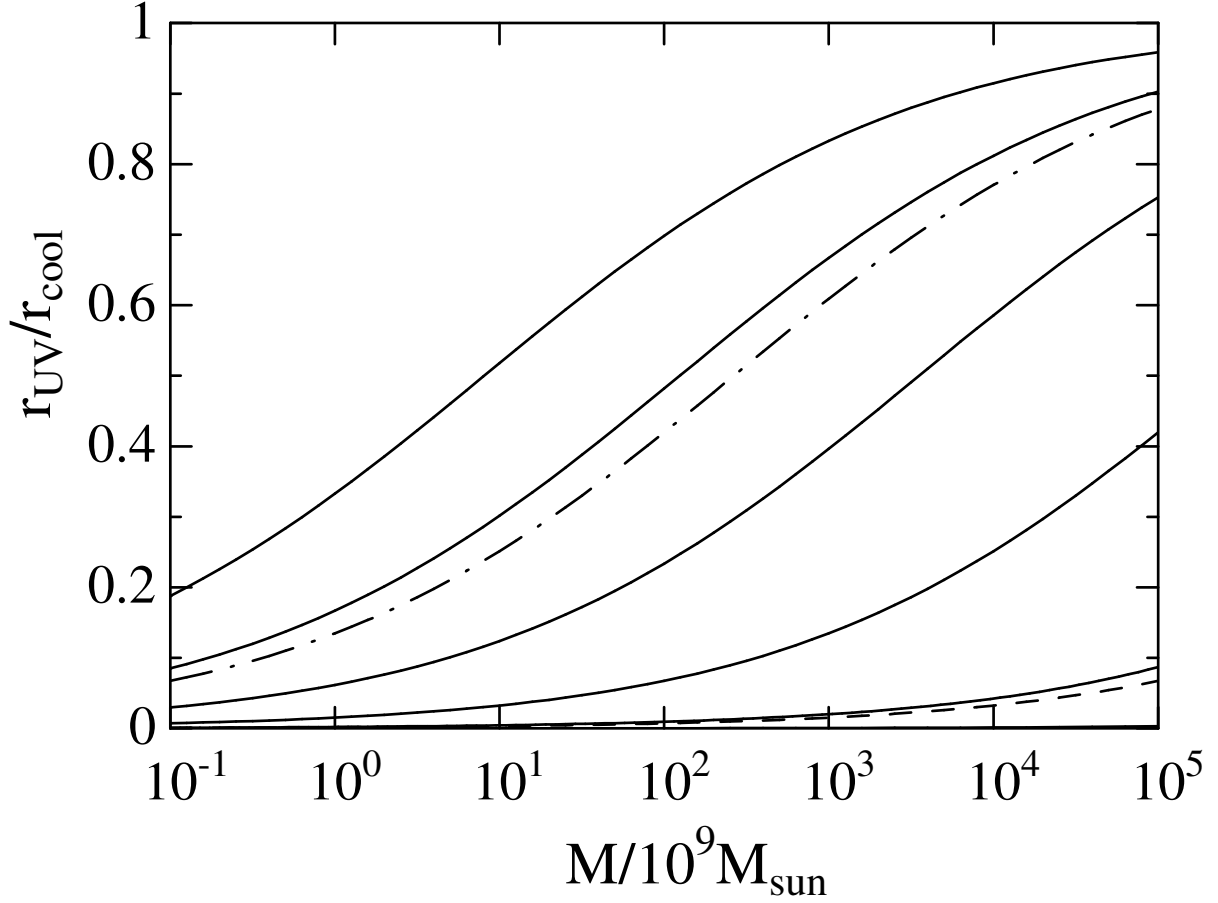


Figure 4.1: Mass fraction of neutral core. The horizontal axis shows the total mass including dark matter. The solid lines denote the ratio r_{UV}/r_{cool} in the case of $J_{-21} = 0.1$ at $z = 5, 4, 3, 2, 1$ and 0 from upper to lower, respectively. Note that the curve at $z = 0$ is almost the same as the horizontal axis. The dash-dotted line and the dashed line show the ratio in the case of $J_{-21} = 0.01$ and 1 at $z = 2$, respectively.

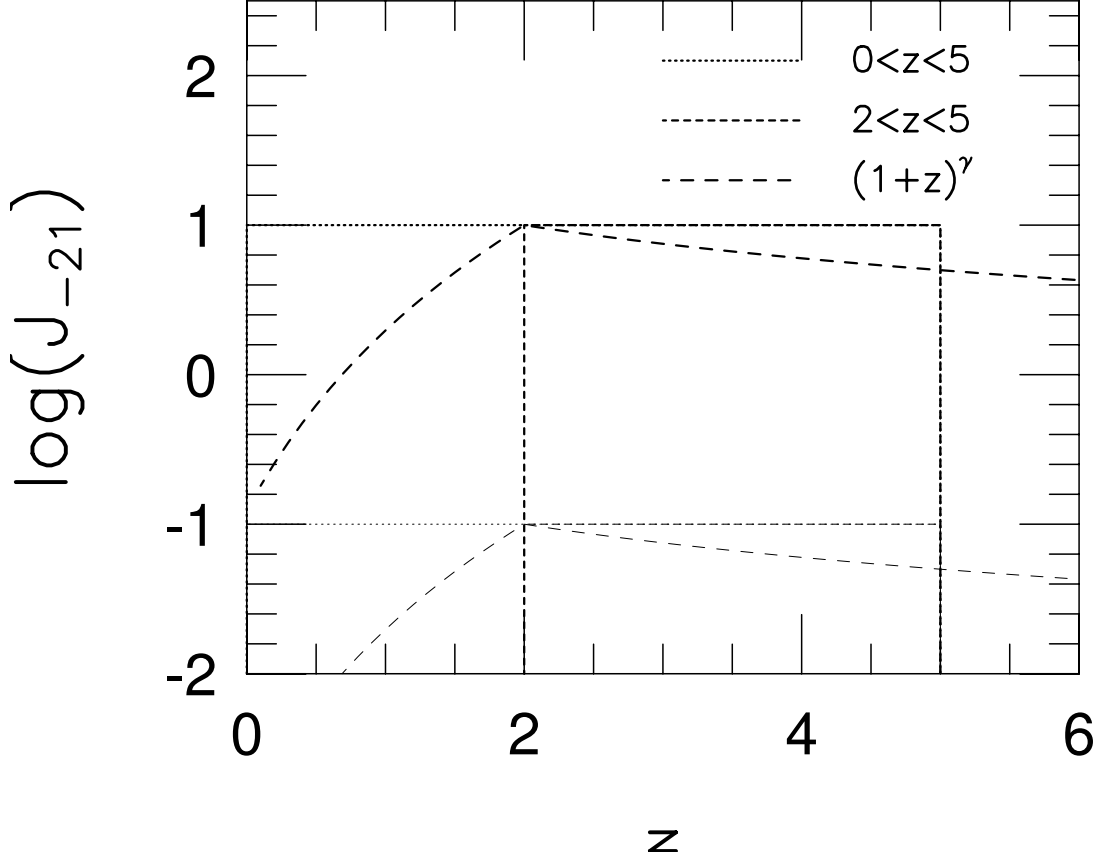


Figure 4.2: Evolution of UV background intensity. The thick lines and the thin lines denote the strong condition and the weak condition, respectively. The dotted lines, the short-dashed lines, and the long-dashed lines show cases (2) UV radiation exists in $0 \leq z \leq 5$, (3) $2 \leq z \leq 5$, and (4) $J \propto (1+z)^\gamma$, $\gamma = 4$ for $z \leq 2$ and $\gamma = -1$ for $z \geq 2$.

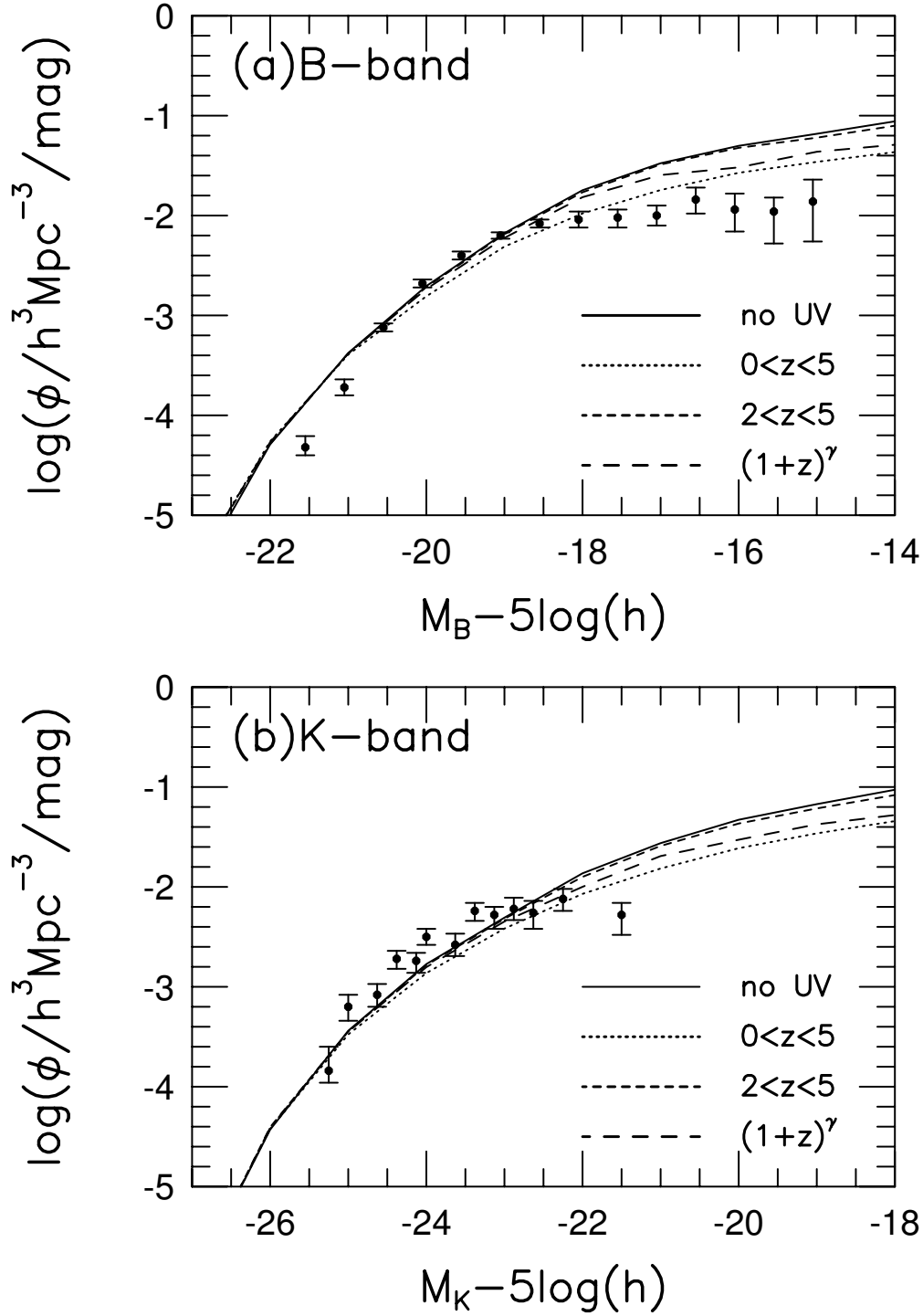


Figure 4.3: (a) B-band luminosity functions. (b) K-band luminosity functions. The solid lines, the dotted lines, the short-dashed lines, and the long-dashed lines show cases (1) no UV, (2) UV radiation exists in $0 \leq z \leq 5$, (3) $2 \leq z \leq 5$, and (4) $J \propto (1+z)^\gamma$, $\gamma = 4$ for $z \leq 2$ and $\gamma = -1$ for $z \geq 2$. In all cases the weak condition is used. The filled circles with errorbars denote the luminosity functions from (a) Loveday et al. (1992) and (b) Mobasher et al. (1993).

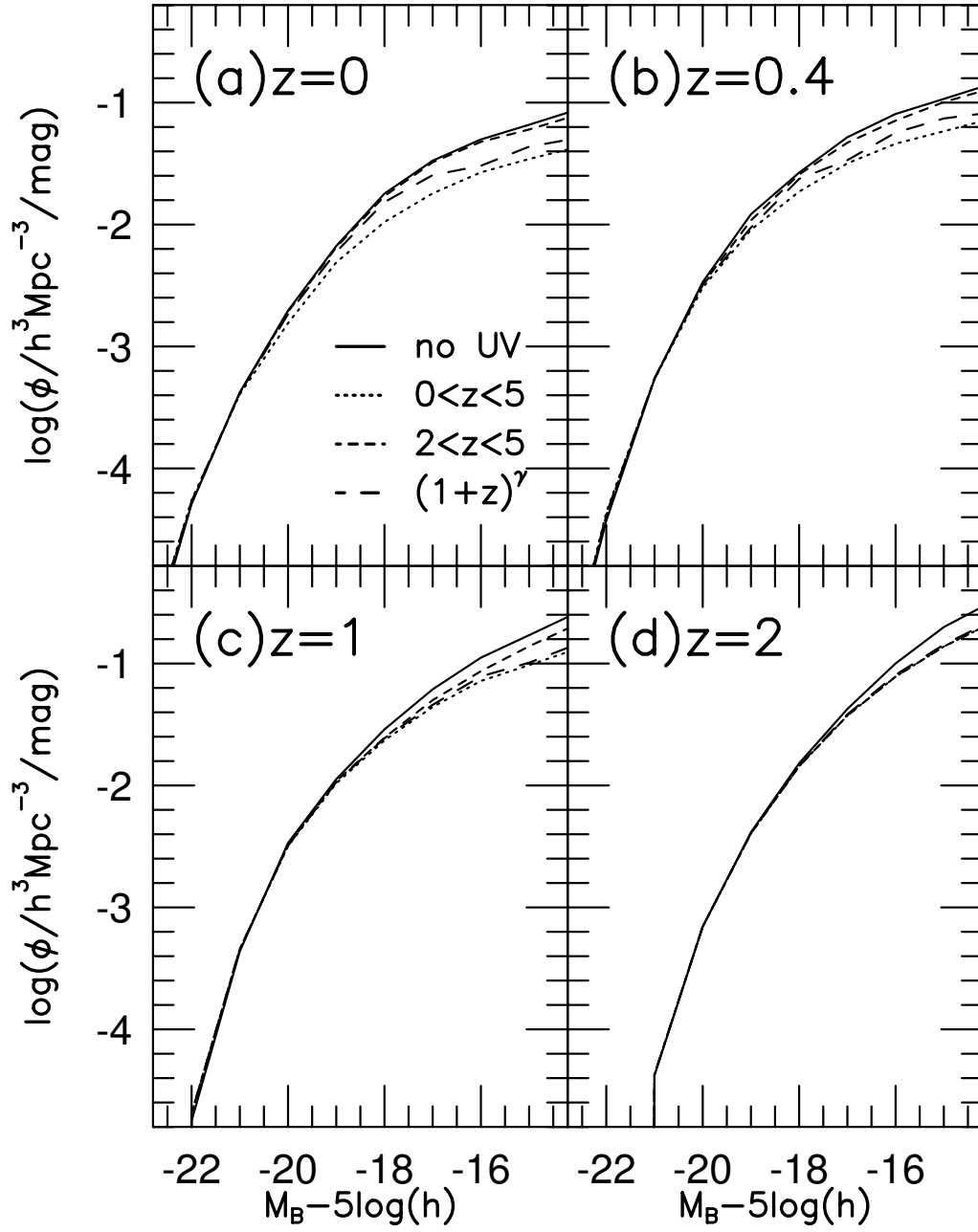


Figure 4.4: B-band luminosity functions in galaxies' rest frame at various redshifts. (a) $z=0$, (b) $z=0.4$, (c) $z=1$, and (d) $z=2$. The types of lines are the same as Figs.4.3. In all cases the weak condition is used.

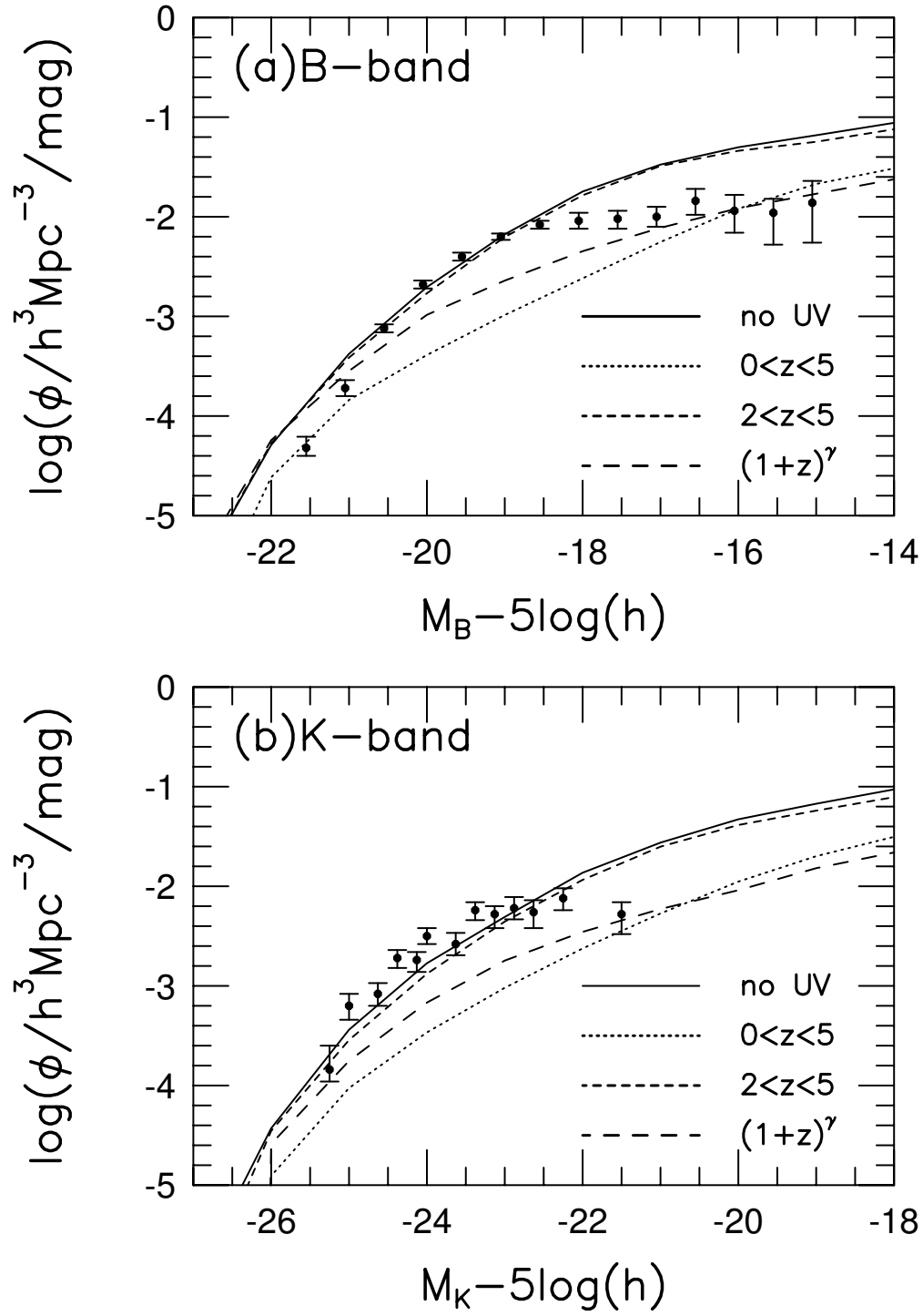


Figure 4.5: Same as Figs.4.3, but for the strong condition.

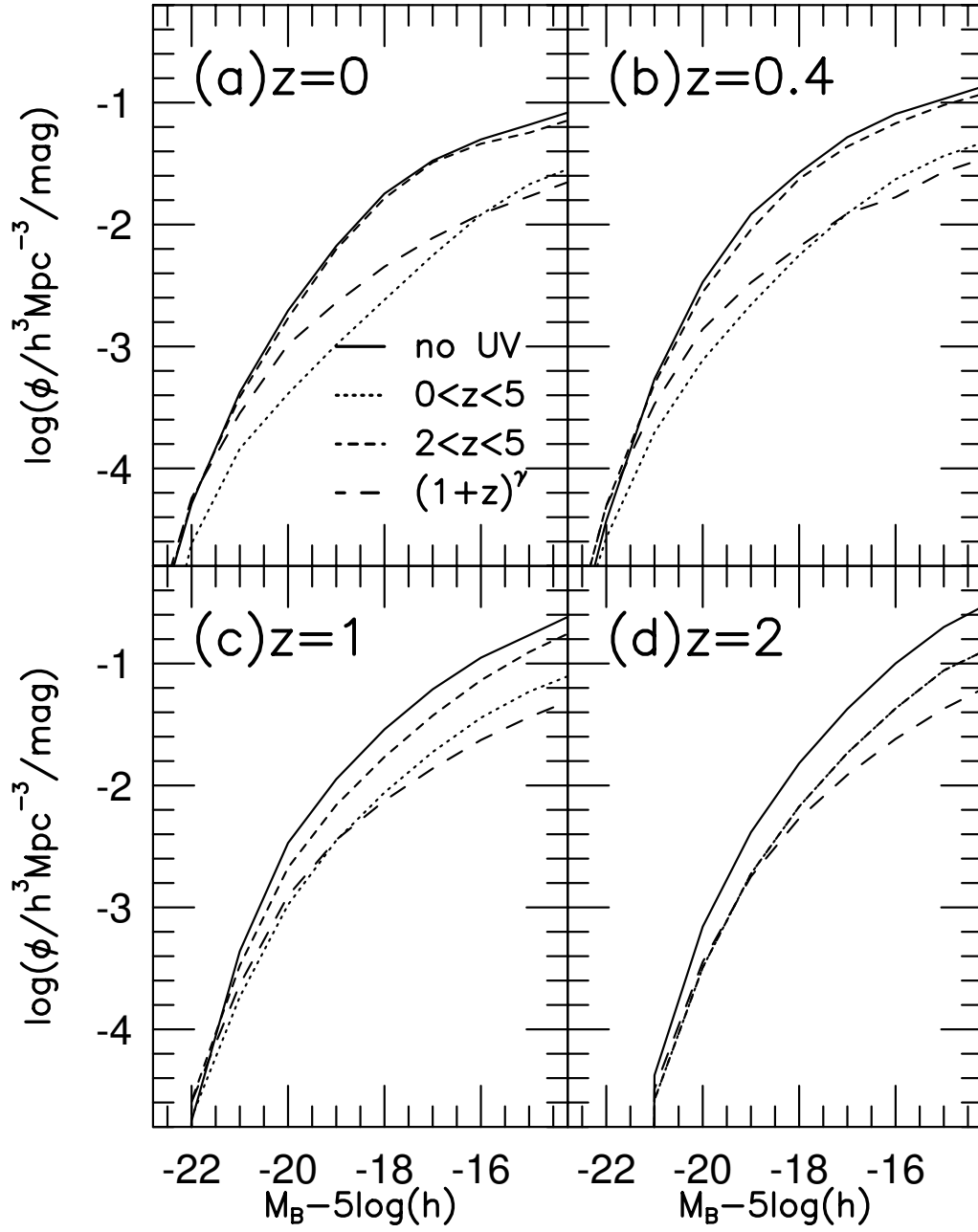


Figure 4.6: Same as Figs.4.4, but for the strong condition.

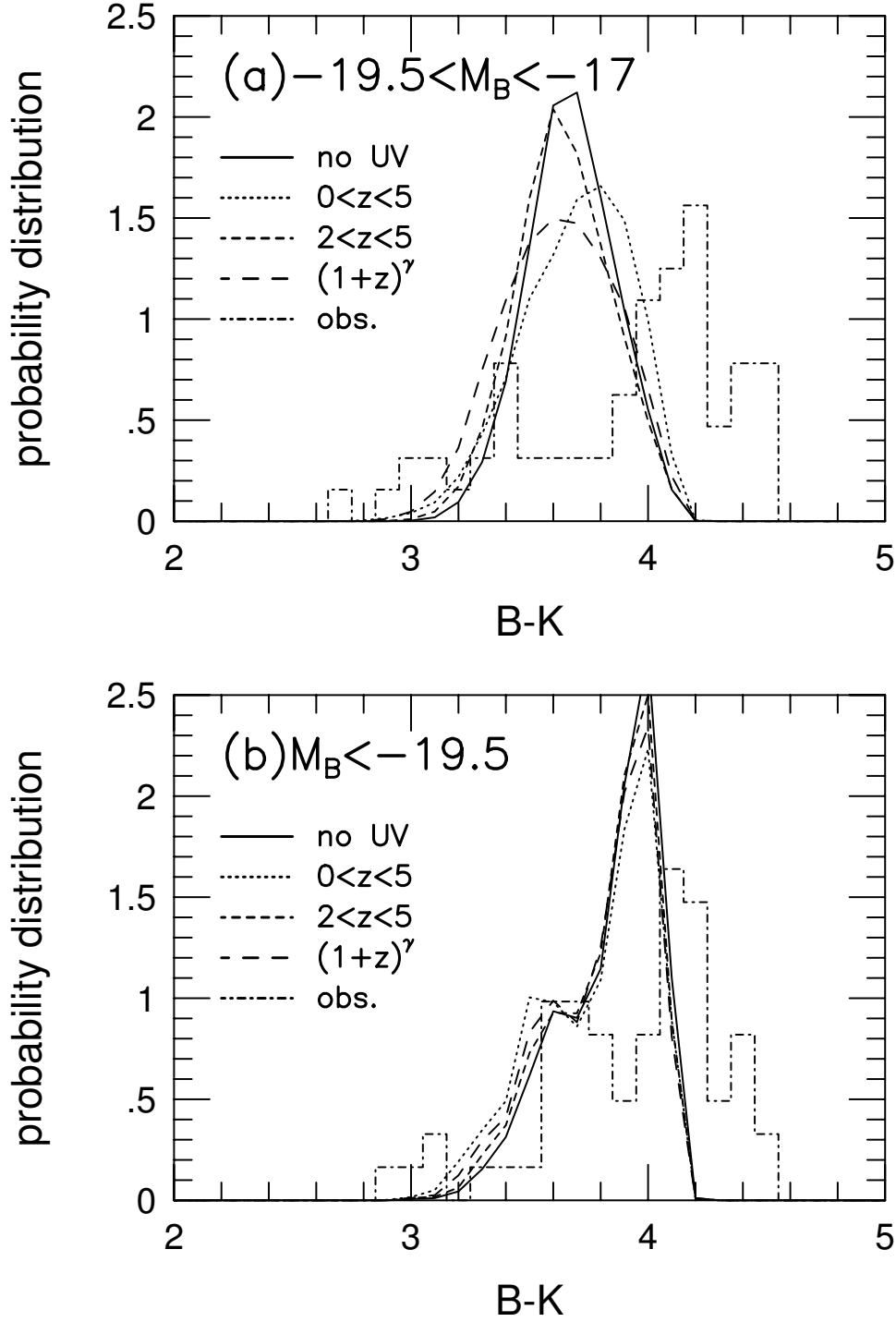


Figure 4.7: Colour distributions in the weak condition. The solid lines, the dotted lines, the short-dashed lines, and the long-dashed lines show cases (1) no UV, (2) UV radiation exists in $0 \leq z \leq 5$, (3) $2 \leq z \leq 5$, and (4) $J \propto (1+z)^\gamma$, $\gamma = 4$ for $z \leq 2$ and $\gamma = -1$ for $z \geq 2$. The histograms of the dash-dotted lines are from Mobasher et al.(1986), which are divided by the total number of galaxies.

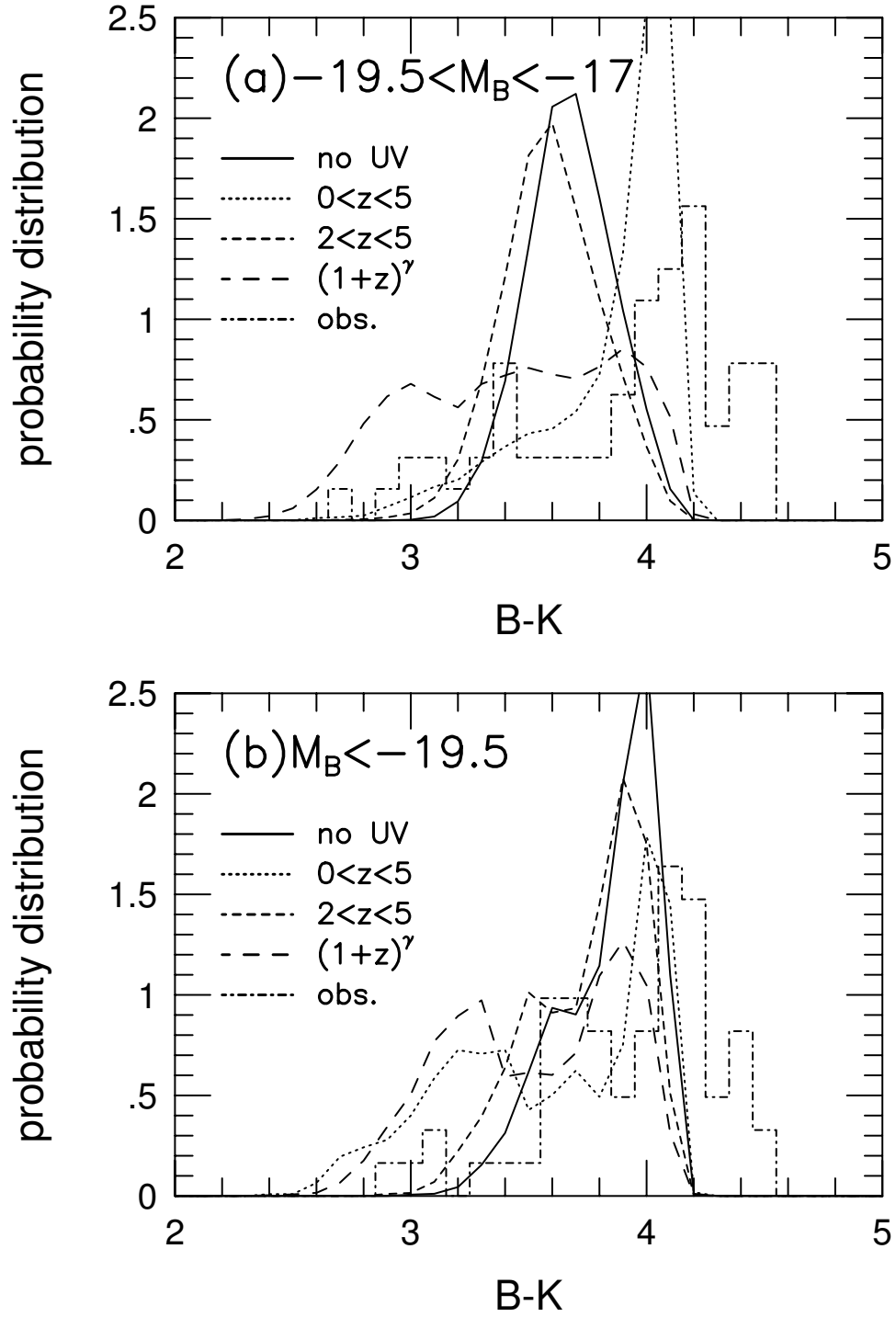


Figure 4.8: Same as Figs.4.7, but for the strong condition.

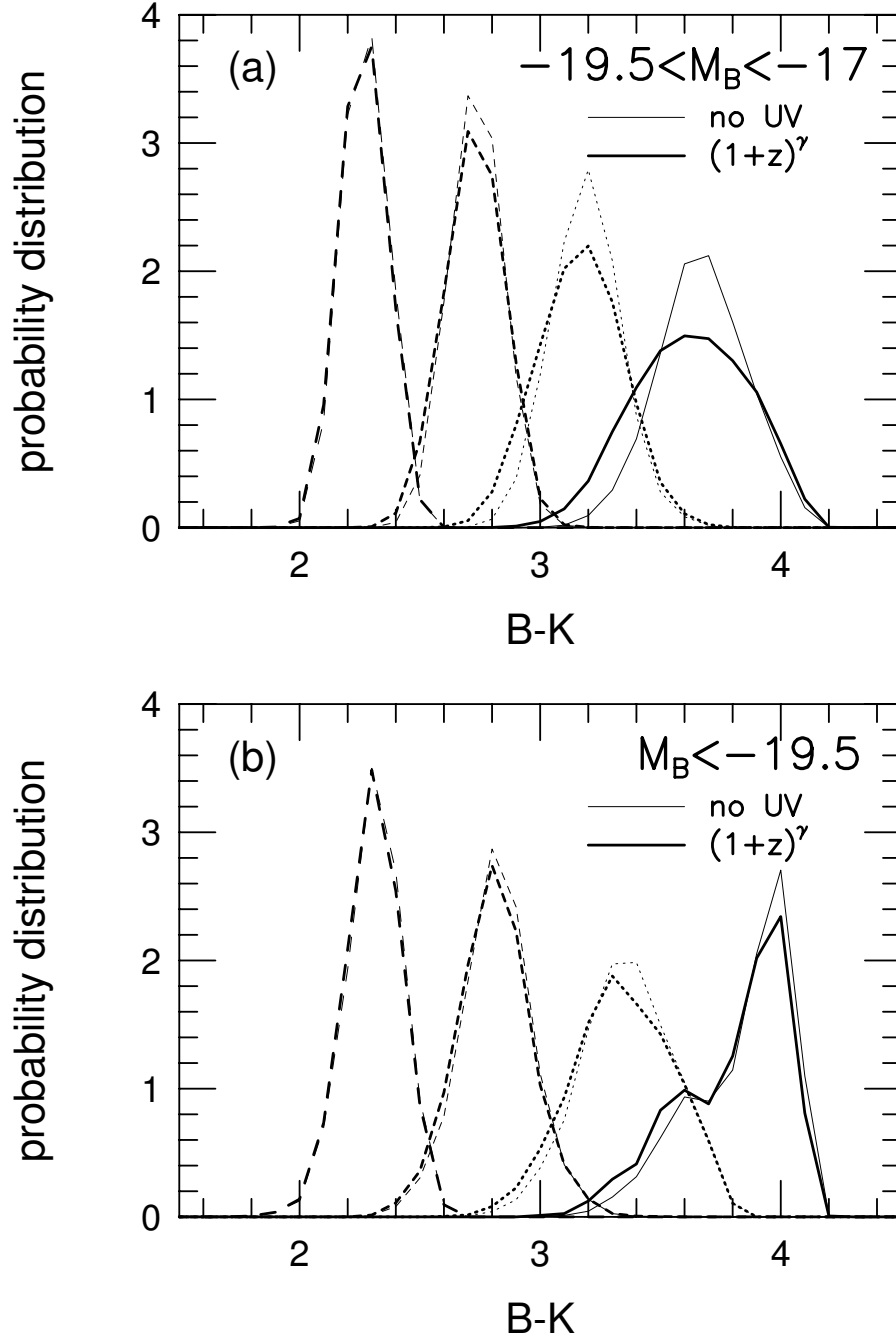


Figure 4.9: Colour distributions at various redshifts in galaxies' rest frame. (a) Colour distributions of galaxies selected by $-19.5 \leq M_B \leq -17$. (b) Colour distributions of galaxies selected by $M_B \leq -19.5$. The solid lines, the dotted lines, the short-dashed lines, and the long-dashed lines denote the distributions at $z = 0, 0.4, 1$, and 2 , respectively. The thin lines and the thick lines show cases (1) no UV, and (4) continuously evolved UV intensity. In all cases the weak condition is used.

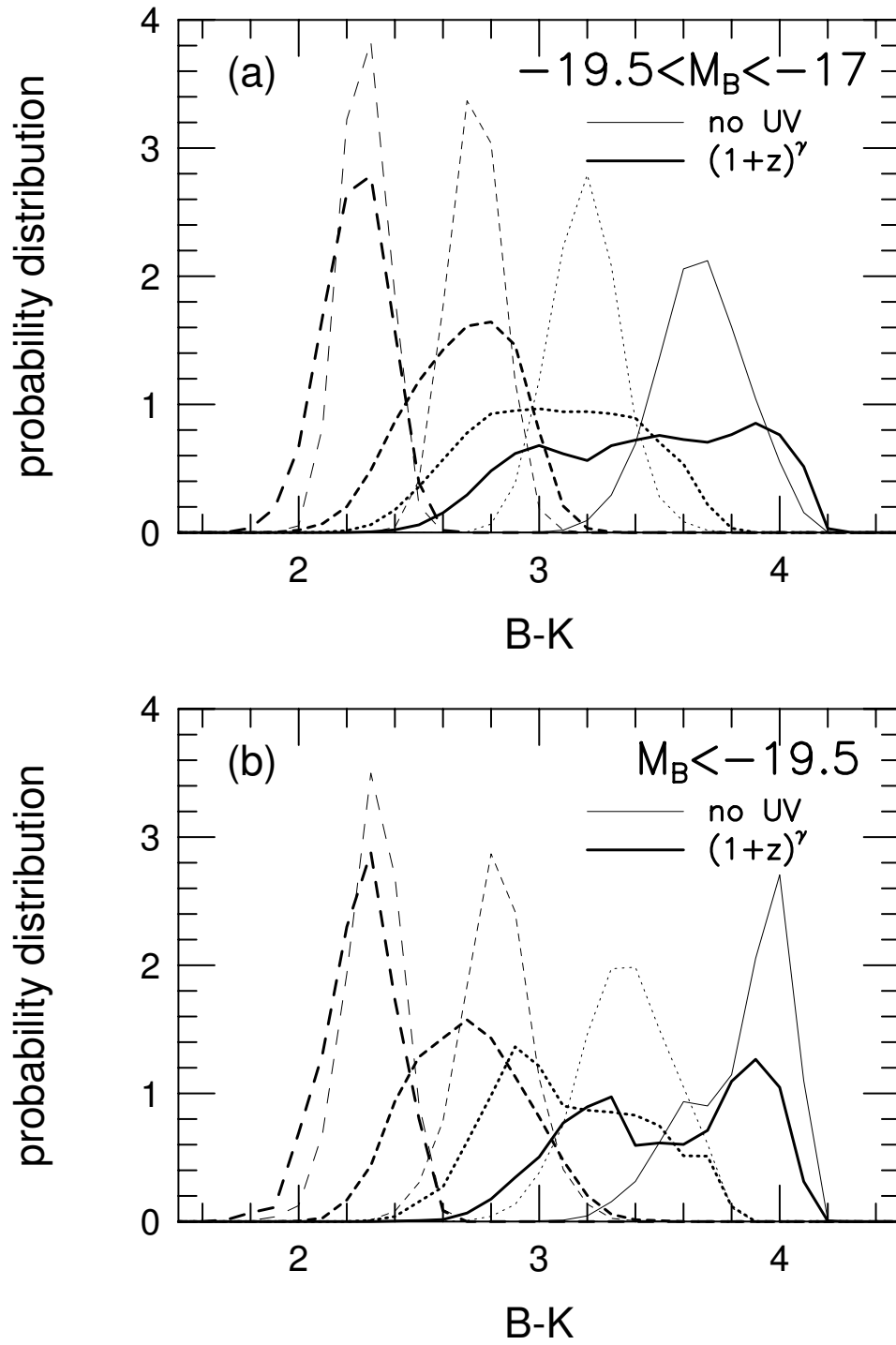


Figure 4.10: Same as Figs.4.9, but for the strong condition.

Chapter 5

The colour-magnitude relation of elliptical galaxies in the hierarchical clustering scenario

5.1 INTRODUCTION

It is well-known that elliptical galaxies in clusters of galaxies have the tight correlation between their colours and magnitudes (so-called ‘colour-magnitude relation’; hereafter CMR). For example, the rms scatter about the mean CMR is typically ~ 0.04 mag in Virgo and Coma clusters of galaxies. It is a comparable size to observational errors (Bower, Lucey & Ellis 1992). Because it is believed that this tight relation reflects the formation and evolution processes of elliptical galaxies, many people have studied this relationship in order to understand the galaxy formation process.

The traditional scenario of the formation of ellipticals is that a monolithic protogalactic cloud collapses and then forms stars for a short timescale until blowing the galactic wind (Larson 1974; Arimoto & Yoshii 1986, 1987). In this framework, the *conventional* interpretation of the CMR of ellipticals is considered as follows. Colour of each galaxy reflects its mean stellar age and metallicity, while luminosity of each galaxy reflects its mass. Therefore, there are two scenarios to make the difference of colours as follows. One is that redder luminous galaxies are formed at earlier stages of cosmological structure formation, and bluer faint galaxies are formed recently. Another scenario is that elapsed time of redder galaxies between the beginning of star formation and the epoch of galactic wind are longer than that of bluer faint galaxies, then more metal-rich stars are formed in luminous galaxies. Therefore the luminous galaxies have redder colour. These two effects, age and metallicity, for reddening the luminous galaxies degenerate (so-called ‘age-metallicity degeneracy’; Worthey 1996). This degeneracy is solved in the collapse/wind model by Kodama & Arimoto (1997) by comparing the CMRs of high redshift cluster galaxies with those of theoretical models. If the CMR reflects the *age sequence*, young faint galaxies should be very blue at high redshift, and the slope of the CMRs evolves rapidly. However, the difference between the slopes of the CMRs at the present epoch and those at high redshift is small compared to the theoretical prediction in the age sequence. This

small difference is in agreement with the prediction in the *metallicity sequence*. Moreover, they suggested that age of ellipticals is longer than $\sim 10\text{Gyr}$. Thus, they found that the CMR reflects the metallicity sequence.

In contrast to such a collapse/wind model, recent developments on both theory and observation of the cosmological structure formation are revealing that objects such as galaxies and clusters of galaxies are formed through hierarchical clustering of smaller objects, as mentioned in Chapter 1. Kauffmann & Charlot (1997; hereafter KC) applied their semi-analytic model to the problem of the CMR, and reproduced the observational properties of the CMRs, when the model includes the chemical evolution process and strong feedback to interstellar media by supernovae. Moreover, they found a tight luminosity-metallicity relation.

KC interpreted why the CMR is reproduced when the feedback process is strong as follows. They considered that bright ellipticals must be formed by mergers of larger spiral galaxies but not from progenitors of faint ellipticals. Because the feedback strength depends on the mass of galaxies, the metallicity of stars in more massive progenitors becomes higher than that in small progenitors. Therefore massive ellipticals become redder than small ellipticals. However, in the hierarchical clustering scenario, larger objects are formed by mergers of smaller objects. So such massive progenitors are formed by mergers of smaller galaxies. Thus the above conclusion may be insufficient for accounting to make the CMR, and it is needed to investigate how the metal abundance evolves in galaxies. The aim of this Chapter is, therefore, exploring what process, such as feedback and star formation, affects the CMR and the evolution of metallicity.

In Section 5.2, we describe the semi-analytic model used here briefly. In Section 5.3, we show the colour-magnitude relation in almost the same model as that of KC, and show evolutions of mean stellar metallicities of galaxies. In Section 5.4, we discuss the origin of the CMR and some effects on CMRs. Section 5.5 is devoted to conclusions.

5.2 MODEL

In this section, the model which we use here is described briefly. The details are shown in Chapter 3. This model is based on the ‘Munich model’, which is developed by Kauffmann and her coworkers. Therefore we do not need to take care of the difference between their model and ours. The model by Kodama & Arimoto (1997) is adopted as a population synthesis model.

5.2.1 Merging history of dark haloes

The merging histories of dark haloes are realized by using the method developed by Somerville & Kolatt (1997), which is described in Section 3.2. In this Chapter, we realize merging paths of progenitors of haloes with mass $5 \times 10^{14} M_{\odot}$, which corresponds to the circular velocity $V_c = 10^3 \text{ km s}^{-1}$. This is a typical size of clusters of galaxies. The time steps are fixed to $\Delta z = 0.05$. When we use a time step larger than 0.05, the mass functions at high redshifts are not in agreement with the theoretical prediction, eq.(2.17). The minimum mass for identifying as an isolated halo is $M_l = 10^{10} M_{\odot}$. Smaller objects than M_l may not be able to collapse because the mass of such objects are smaller than the Jeans mass after the reionization of intergalactic medium by the UV background radiation at $z \sim 10$, $\sim 10^{10} M_{\odot}$ (Ostriker & Gnedin 1996), and because galaxies are formed actively at $z \lesssim 5$. We find that results presented in this

Chapter does not depend on the choice of $M_l \lesssim 10^{10} M_\odot$. The power spectrum $P(k)$ of density fluctuations given by Bardeen et al. (1986) is adopted (see Chapter 3). We adopt the standard CDM model, $\Omega = 1$ and $h = 0.5$, in this Chapter.

5.2.2 Cooling, star formation, and feedback

In this Chapter, we adopt a similar treatment to the ‘Munich model’ as for the cooling, star formation, and feedback processes, which are described in Chapter 3. We set $f_{reheat} = 0.2$. The other parameters are shown in Table 5.1.

It is the conclusion of KC that this feedback process is a key parameter to determine the slope of the CMR. Therefore we also investigate the dependence of CMR on the feedback process.

5.2.3 Mergers of galaxies

The dynamical friction timescale is estimated by eq.(3.13). In this Chapter, we do not treat mergers between satellite galaxies for simplicity, which is described in Somerville & Primack (1998). There is a possibility that this effect changes the resulting CMRs. This effect will be considered in future work.

5.2.4 Chemical evolution

Chemical evolution is treated in almost the same way as described in KC. The instantaneous recycling approximation is adopted (Tinsley 1980). We show the gas and metal exchange in Fig.5.1 schematically. Metals ejected from supernovae are recycled as follows.

When two or more haloes merge together, metals contained in the hot gas is joined together. If two or more galaxies merge together, metals contained in the cold gas reservoirs of galaxies are joined together. When the hot gas cools, metals contained in the cooled gas are also joined to the cold component. Here we assume that metals in cold and hot components are well-mixed in each component. Stars formed from the cold gas have initially the same metallicity as the cold gas. This metallicity affects colours of galaxies directly.

The amount of metals ejected from supernovae is characterized by y , which is heavy element yield for each generation of stars. The fraction f of the ejecta is ejected directly into the hot gas, and the rest, $1 - f$, is incorporated with the cold gas. We adopt $f = 0.3$, which is the same value as in KC. The gas fraction returned by evolved stars R is 0.75 in this Chapter. Simultaneously, the supernovae heat up the surrounding cold gas, therefore metals contained in the cold gas are also returned to the hot gas.

5.3 RESULTS

In this Chapter, because we investigate how the CMR depends on the physical processes such as star formation, supernova feedback, and so on, we fix the cosmological parameters to the standard CDM model, that is, $\Omega = 1, \Lambda = 0, H = 50 \text{ km s}^{-1} \text{ Mpc}^{-1}$, $\Omega_b = 0.06$, and $\sigma_8 = 0.67$. We refer to the models considered by the models A, B, C and D as shown in Table 1. In this

Table 5.1: Parameters for models.

Model	V_{hot} (km s $^{-1}$)	α_{hot}	τ_*^0 (Gyr)	UV
A	280	2	20	off
B	100	2	20	off
C	220	5.5	20	off
D	100	5.5	20	off
E	600	2	2	off
F	100	2	2	off
G	280	2	2	on
H	100	2	2	on

table, we also show models E, F, G and H, which are adopted in the next section. The fifth column, UV, is explained in Section 5.4.3. The yield y is equal to $0.038 = 2Z_\odot$, in all the models. In KC, $y = 1.2Z_\odot$ in the low feedback model. However, in order to see the effects of the feedback and so on, we fix the value of the yield in all models.

In the following sections, we take notice of only the slopes of CMRs, because the luminosity of galaxies can be translated by considering the following reason. Stars are formed according to the IMF as mentioned in Chapter 3. Mass of luminous stars is larger than $\sim 0.08M_\odot$, which is determined by the criterion of nuclear burning. However, there is a possibility that invisible stars with mass smaller than $0.08M_\odot$. If there are many invisible stars in galaxies, the galaxies become faint compared to the case that all stars are luminous. The ratio of the invisible stars to the luminous stars is treated as a free parameter in the previous work. Therefore the absolute value of luminosity can be adjusted by this parameter. The suitable value of this parameter will be determined by considering other observational quantities. Thus this parameter does not affect the slope of the CMR.

5.3.1 Colour-magnitude relations

In Fig.5.2, we show the CMRs in the models A and B with $\alpha_{hot} = 2$ which is the value adopted by KC. The open circles denote galaxies identified as ellipticals, and the solid lines show the observational CMRs (Bower et al. 1992). The criterion to pick out ellipticals among all galaxies is shown in Section 3.7.

As in KC, in the model A with high feedback efficiency, the slopes of the CMRs are in roughly agreement with the observations, but the dispersion is larger than that of observations, ~ 0.04 mag. Maybe this is because the cooled gas mass is estimated by eq.(3.7). This effect suppresses a surplus cooling of hot gas. On the other hand, in the model B with low feedback efficiency, the slopes of the CMRs are nearly flat. In the model C with intermediate feedback efficiency $V_{hot} = 220$ km s $^{-1}$ but $\alpha_{hot} = 5.5$ which is the value adopted by Cole et al. (1994), the slopes of the CMRs are almost the same as those in the model A (Fig.5.3). The model D with low feedback efficiency does not reproduce the observations as well as in the model B (Fig.5.3).

Next we show the V-luminosity weighted mean stellar age and metallicity defined as follows,

$$\langle Z_* \rangle_{L_V} \equiv \frac{\int_0^{t_0} L_V(t, Z_{cold}) \dot{M}_*(t) Z_{cold}(t) dt}{\int_0^{t_0} L_V(t, Z_{cold}) \dot{M}_*(t) dt}, \quad (5.1)$$

$$\langle t \rangle_{L_V} \equiv \frac{\int_0^{t_0} L_V(t, Z_{cold}) \dot{M}_*(t) t dt}{\int_0^{t_0} L_V(t, Z_{cold}) \dot{M}_*(t) dt}, \quad (5.2)$$

where Z_{cold} is the metallicity of cold gas, $\dot{M}_*(t)$ is the star formation rate at t , and $L_V(t, Z_{cold})$ is the luminosity of stars at present, $t = t_0$, with age $t_0 - t$ and metallicity Z_{cold} . In all models, the distributions of mean stellar age are alike (upper panels of Figs.5.4 and 5.5), and the mean stellar ages spread about $5 \sim 11$ Gyr. On the other hand, in high feedback efficiency models (A in Fig.5.4c and C in Fig.5.5c), there are tight relations between the V-luminosity and the mean stellar metallicity, and their slopes are steeper than those of the model B in Fig.5.4d and D in Fig.5.5d.

From these figures, we conclude that the CMR results from the metallicity-luminosity relation, as KC concluded, and that the dispersion of the CMR results mainly from the dispersion of the mean stellar age.

The conclusion of the origin of the metallicity-luminosity relation in KC is that ellipticals are formed by mergers of gas-rich spirals, and that massive ellipticals are formed from massive spirals because the feedback efficiency of such massive galaxies is small, and so more metal-rich stars are formed (Fig.2 in KC). We will show the evolutions of mean stellar metallicity and age of each galaxy in order to investigate this process in detail.

5.3.2 Evolution of mean stellar metallicity

In this subsection, we show the evolutions of the mean stellar metallicity $\langle Z_* \rangle_{M_*}$, which are weighted by stellar mass for simplicity.

In the upper panels of Fig.5.6, we show the evolutions of stellar metallicity of luminous ellipticals picked out in the models A and B. Their final magnitudes and colours are $M_V = -24.1, U - V = 1.49, V - K = 3.12$ and $M_V = -23.9, U - V = 1.61, V - K = 3.23$, respectively. The open circles denote the mean stellar metallicities of progenitors in the *elliptical state*, which is defined as the bulge-to-disk stellar mass ratio $M_{bulge}/M_{disk} \geq 0.6$, and the dots show those in the *spiral state*, $M_{bulge}/M_{disk} < 0.6$. These two luminous galaxies are identified as galaxies experiencing the same merging path of dark haloes. Because the merging histories of dark haloes of these galaxies are the same, the difference between results in different models is caused from only parameters shown in Table 5.1. These galaxies rapidly grow in mass and the feedback effect becomes weak at early times. So the mean stellar metallicities also exceeds Z_\odot at early times. Therefore, the difference between these galaxies is small. The final metallicity of elliptical galaxy in the model A (Fig.5.6a) is smaller than the yield $y = 0.038$. The reason for this is considered as follows. One is that the feedback effect remains a little because of the shallower dependence of feedback on circular velocity, $\alpha_{hot} = 2$. Second is that the star formation timescale is very long, $\tau_*^0 = 20$ Gyr (see Chapter 3). On the other hand, the difference between faint ellipticals is large (lower panels of Figs.5.6). The ratio of the final metallicities is more than a factor of two. These faint ellipticals are also picked out in the same merging

path. Their final magnitudes and colours are $M_V = -19.8, U - V = 1.02, V - K = 2.82$ and $M_V = -20.5, U - V = 1.14, V - K = 3.10$, respectively. In the high feedback efficiency model A, the growth of the mean stellar metallicity is slow and the growth in the low feedback efficiency model B is rapid and then the final metallicity is near the value of the yield, $y = 0.038$. This shows that in the low feedback model even small galaxies can evolve chemically.

In Fig.5.7, we show the same figures but for $\alpha_{hot} = 5.5$ (the models C and D). Final magnitudes and colours of luminous galaxies are $M_V = -24.4, U - V = 1.51, V - K = 3.15$ in the model C and $M_V = -24.0, U - V = 1.62, V - K = 3.24$ in the model D. Those of faint ellipticals are $M_V = -19.9, U - V = 0.90, V - K = 2.66$ in the model C and $M_V = -20.4, U - V = 1.39, V - K = 3.18$ in the model D. In the cases of luminous ellipticals, the evolutions at early stages are similar to those in the models A and B but the final metallicities are a little different. The reason for this is that the feedback effect becomes finally negligible because of the steep dependence of feedback on circular velocity, $\alpha_{hot} = 5.5$, and because of a little weaker feedback $V_{hot} = 220 \text{ km s}^{-1}$ than that of the model A, $V_{hot} = 280 \text{ km s}^{-1}$. In the cases of faint ellipticals, the growth of the evolution of metallicity is strongly suppressed at early stages in the model C, but finally the metallicity is nearly equal to that in the model A (Fig.5.6c). The reason for this is the same as that for the luminous ellipticals. The amplitude of feedback, V_{hot} , in the model C is lower than that in the model A, while the dependence of feedback on circular velocity, α_{hot} , in the model C is steeper than that in the model A. These two effects are canceled out each other at the final stage.

From the above results, we conclude that the colour of luminous galaxies reflects the yield strongly because the effect of the feedback on such luminous galaxies is negligible. This case corresponds to the model C ($\alpha_{hot} = 5.5$). In this case, the feedback in luminous ellipticals with large circular velocity is quite suppressed [see eq.(3.12)]. But in the case of small α_{hot} , the feedback effect remains even in luminous ellipticals. So the colour of luminous galaxies is determined not only by y but also the strength of the feedback. On the other hand, in faint ellipticals, their colour reflects the feedback efficiency, $\beta [= (V/V_{hot})^{-\alpha_{hot}}$, see eq.(3.12)], directly. In other words, when the value of y is fixed, the evolution of stellar metallicity in faint galaxies is suppressed in the case of high feedback models, and the metallicity of luminous galaxies is almost determined by the yield, y , because the feedback effect becomes negligible in such luminous galaxies. Therefore, a suppression of growth of stellar metallicity is required in small galaxies for making the slope of CMRs. The relationship between the metallicity and the feedback is discussed in the next section.

5.4 DISCUSSION

5.4.1 Feedback and yield

In a chemical evolution of a simple monolithic cloud collapse model, the evolution of metallicity of cold gas for a constant star formation timescale, τ_* , is described as

$$Z_{cool}(t) = 1 - (1 - Z_{cool}^0) \exp \left[-(1 - f) \alpha y \frac{t - t_s}{\tau_*} \right], \quad (5.3)$$

where α is a locked-up mass fraction, $\alpha = 1 - R$ (R is the gas fraction returned by evolved stars), and Z_{cool}^0 is an initial metallicity of cold gas at $t = t_s$. The total star formation rate is

$$\dot{M}_*(t) = \frac{M_{cool}(t)}{\tau_*} - RM_*(t), \quad (5.4)$$

where we use the instantaneous recycling approximation. From these two equations, the mass-weighted mean stellar metallicity is obtained as

$$\langle Z_*(t) \rangle_{M_*} = 1 - F \frac{1 - \exp \left[-(1 + \beta - (R - \alpha y)(1 - f)) \frac{t - t_s}{\tau_*} \right]}{1 - \exp \left[-(1 + \beta - R(1 - f)) \frac{t - t_s}{\tau_*} \right]}, \quad (5.5)$$

where

$$F = \frac{1 - Z_{cool}^0}{1 + \frac{(1-f)\alpha y}{1+\beta-R(1-f)}}. \quad (5.6)$$

This shows that when the feedback is strong the final mean stellar metallicity becomes small, $\langle Z_*(t \rightarrow \infty) \rangle_{M_*} \rightarrow Z_{cool}^0$ as $\beta \rightarrow \infty$. Moreover, increasing y is corresponding to decreasing the feedback strength β . This effect determines the absolute value of final mean stellar metallicity, especially for faint galaxies. On the other hand, when the feedback is negligible ($\beta \ll 1$), the factor F is determined by only y . So the effect of y is remarkable in luminous galaxies rather than in faint galaxies. The results in the previous section reflect this tendency.

5.4.2 Slope of colour-magnitude relation

The mass-weighted mean stellar metallicity $\langle Z_*(t) \rangle_{M_*}$ is a monotonously increasing function about t in the description in the previous subsection. The timescale of this increase is given by the star formation timescale, τ_* . In the previous Section, we adopt $\tau_*^0 = 20$ Gyr. So the actual final mean stellar metallicity is lower than $1 - F$ because its star formation timescale is longer than the Hubble time. So if we adopt a short star formation timescale, mean stellar metallicities of galaxies increase totally and colours become redder. However, we can make the slope of the CMR by a stronger feedback even if we adopt shorter star formation timescale.

In this subsection, we use a short star formation timescale, $\tau_*^0 = 2$ Gyr. In the model E, a more efficient feedback, $V_{hot} = 600$ km s⁻¹ is adopted. This value corresponds to $\epsilon \sim 1$ in eq.(3.11). We show the CMRs in this case in the left panels of Fig.5.8. In order to compare it with a weak feedback model, we show the model F with $V_{hot} = 100$ km s⁻¹ in the right panels of Fig.5.8. The slopes of the CMRs are almost the same as Fig.5.2 in the models A and B, and the colours in the model F become redder because the mean stellar metallicity evolves rapidly due to the short star formation timescale.

Moreover, we investigate the metallicity-luminosity relations and the evolutions of the mean stellar metallicities. The results (not shown) also have almost the same trend as those of the models A and B (Figs.5.4 and 5.6).

From this result, we conclude that the metallicity-luminosity relation, which makes the CMR, is determined not only by the feedback efficiency but also by the star formation timescale. It depends on a balance of these two parameters, β and τ_*^0 . It is important for making CMR to suppress forming high metallicity stars in faint galaxies (see the discussion in the previous subsection).

5.4.3 Effect of the UV background radiation

In this subsection, we evaluate the effect of the Ultraviolet (UV) background radiation on the CMR. This effect on luminosity function of galaxies is similar to increasing feedback efficiency (see Cole et al. 1994 and Chapter 4; Nagashima et al. 1998). Therefore, we introduce the effect of the UV background in our model instead of strengthening the feedback efficiency. The method including the UV background into the semi-analytic model is described in Chapter 4. We use a model similar to the case (4) in Chapter 4, $J_{-21}(z = 2) = 1$, $J_{-21} \propto (1 + z)^\gamma$, $\gamma = 4$ at $z \leq 2$, $\gamma = -1$ at $2 \leq z \leq 5$, and $J_{-21} = 0$ at $z > 5$.

In Fig.5.9, we show the CMRs in the models G and H, with short star formation timescale, $\tau_*^0 = 2$ Gyr. The feedback strengths are $V_{hot} = 280$ and 100 km s^{-1} , respectively. The observed slopes of the CMR are reproduced well and the dispersions of the model CMRs become very small compared to the other previous models. The reason for this is considered as follows if the main origin of the dispersion is the dispersion of mean stellar age. When the effect of the strong feedback to suppress the star formation of stars is considered, the star formation is suppressed in each galaxy independently. On the other hand, when the effect of the UV background is considered, the star formation is suppressed and resumed at almost the same epoch in galaxies with the same mass. Therefore the age of stars are almost the same when the effect of the UV background. In these cases, we also confirmed that the metallicity-luminosity relations and the evolutions of the mean stellar metallicities show almost the same trend as the previous models.

The virtue of the model G is that the amount of cold gas in ‘Milky Way’-like galaxies, which belongs to a halo with circular velocity of 220 km s^{-1} , is $\sim 10^{10} M_\odot$. This value is nearly equal to that in our Galaxy. On the other hand, the model E ($V_{hot} = 600 \text{ km s}^{-1}$ and $\tau_*^0 = 2$ Gyr), the amount of the cold gas is much less than that in our Galaxy.

Of course, such a *degeneracy* will be solved by observing other quantities, such as luminosity function, cold gas content, and so on, because the dependences of these quantities on the feedback process, the star formation time scale, and the UV background are different. This will be done in future work.

5.4.4 Metal recycling

In our model based on the hierarchical clustering scenario, the metals released to hot gas return to cold gas later. We must evaluate whether this metal recycling affects the luminosity-metallicity relation.

When $t \gg \tau_*$, the reheated gas mass and newly formed stellar mass fractions are

$$\frac{M_{reheat}}{M_* + M_{reheat}} = \frac{\beta + Rf}{1 + \beta - R(1 - f)}, \quad (5.7)$$

$$\frac{M_*}{M_* + M_{reheat}} = \frac{1 - R}{1 + \beta - R(1 - f)}. \quad (5.8)$$

When considering small galaxies, which have a strong feedback efficiency ($\beta \gg 1$), most of cold gas are transformed to hot gas. So it is difficult for such small galaxies to form high metallicity stars. It means that the amount of metals formed in the galaxies is small. Therefore the hot gas does not evolve chemically. Thus the effect of metal recycling from hot gas to cold gas is

slight. In order to confirm this, we calculate the CMR by using the model in which the metals returned from hot gas to cold gas are removed by hand. We find that the difference between the results of considering such metals and removing metals is small, about 0.2 mag lower in $V - K$ and that the difference between the slopes is negligible. Therefore the effect of the metal recycling is negligible

5.5 CONCLUSIONS

We investigate the physical mechanisms determining the properties of the CMRs. We show that the feedback efficiency, the star formation timescale, and the yield are the key parameters to determine the properties of the CMRs.

The metallicity-luminosity relations, which are directly reflected to the CMRs, are formed as follows. At high luminosity, massive galaxies are dominated, whose feedback strength is weak. Because the feedback strength decreases as growing the mass of galaxies, the number of high metallicity stars increases. In this case, the mean stellar metallicity is determined by the yield mainly.

On the other hand, at low luminosity, we must consider some mechanisms for suppressing the stellar metallicity. The following three parameters determine the mean stellar metallicity of the low luminosity ellipticals: the star formation timescale, the feedback strength, and the intensity of the UV background [see eq.(5.5)]. The final mean stellar metallicity increases when the star formation timescale decreases, because the timescale of metal enrichment is given by the star formation timescale and because the mean stellar metallicity increases as time passes monotonously in the case that a monolithic cloud forms stars. When the feedback and UV background strength increase, the final mean stellar metallicity decreases. The reason for this is that the star formation is suppressed and then the amount of metals ejected into the gas decreases.

Therefore one of the solutions to form the metallicity-luminosity relation is to increase the feedback strength when the star formation timescale decreases. We find that the slope of the CMR given by observation is reproduced in the both cases of $V_{hot} = 280 \text{ km s}^{-1}$ and $\tau_*^0 = 20 \text{ Gyr}$, and $V_{hot} = 600 \text{ km s}^{-1}$ and $\tau_*^0 = 2 \text{ Gyr}$.

Another solution is to consider the effect of the UV background radiation. When including this effect, we can also reproduce the observed CMR even in the case of short star formation timescale, $\tau_*^0 = 2 \text{ Gyr}$. Such a value of star formation timescale is often used for describing star formation in disk galaxies (e.g., Arimoto, Yoshii & Takahara 1991). Moreover, we confirmed the amount of cold gas in ‘Milky Way’-like galaxies, which are galaxies contained in haloes with $V_c = 220 \text{ km s}^{-1}$, is nearly equal to the observed one.

In this Chapter, we show the physical mechanisms forming the CMRs and discuss the possible effects on the CMRs. We find a kind of ‘degeneracy’ among the star formation, the feedback, and the UV background for making the slope of the CMRs. This degeneracy will be solved by comparing other statistical properties of galaxies such as luminosity function and colour distribution in future work. Moreover, we should consider the tightness of CMRs. The tightness may reflect the dispersion of the mean stellar ages. It suggests this that the model G, which has a tight CMR, has a small dispersion of the mean stellar ages, about $7 \sim 11 \text{ Gyr}$

(not shown). This is smaller than the dispersion in the other models, about $5 \sim 11$ Gyr. We guess the reason for this as follows. When the effect of the strong feedback to suppress the star formation of stars is considered, the star formation is suppressed in each galaxy independently. On the other hand, when the effect of the UV background is considered, the star formation is suppressed and resumed at almost the same epoch in galaxies with the same mass. We will investigate the origin of the tightness minutely in future work.

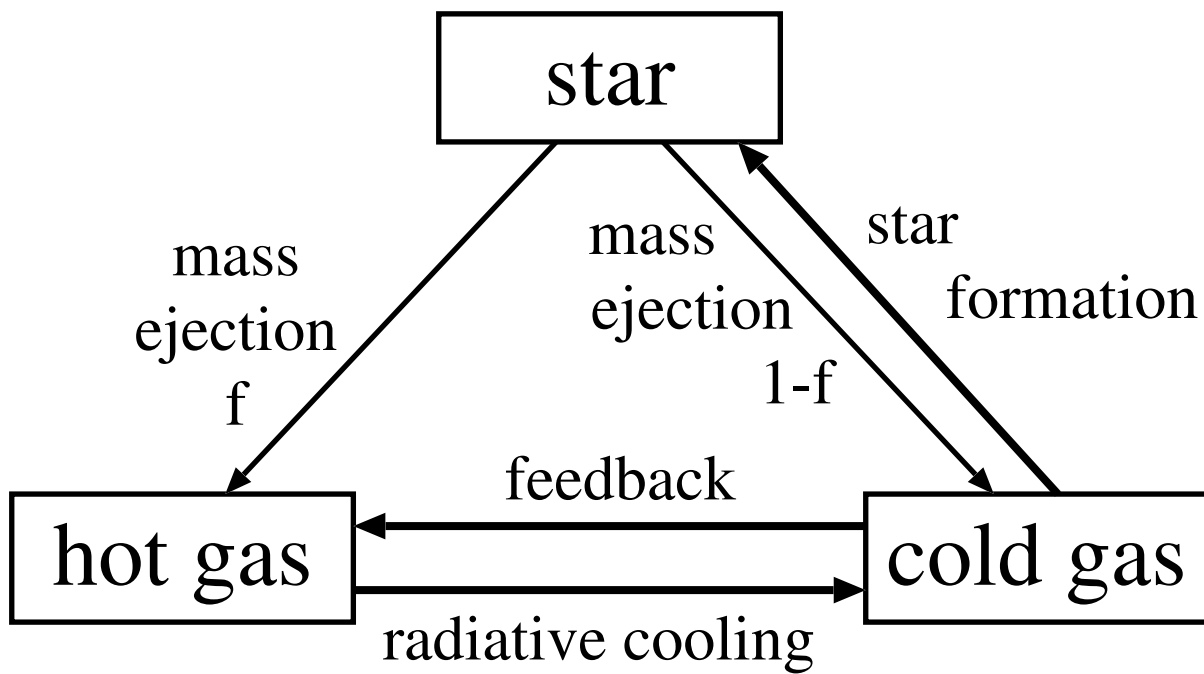


Figure 5.1: Schematic description of gas and metal recycling in star formation. f is a fraction of ejected mass from evolved stars into hot gas directly.

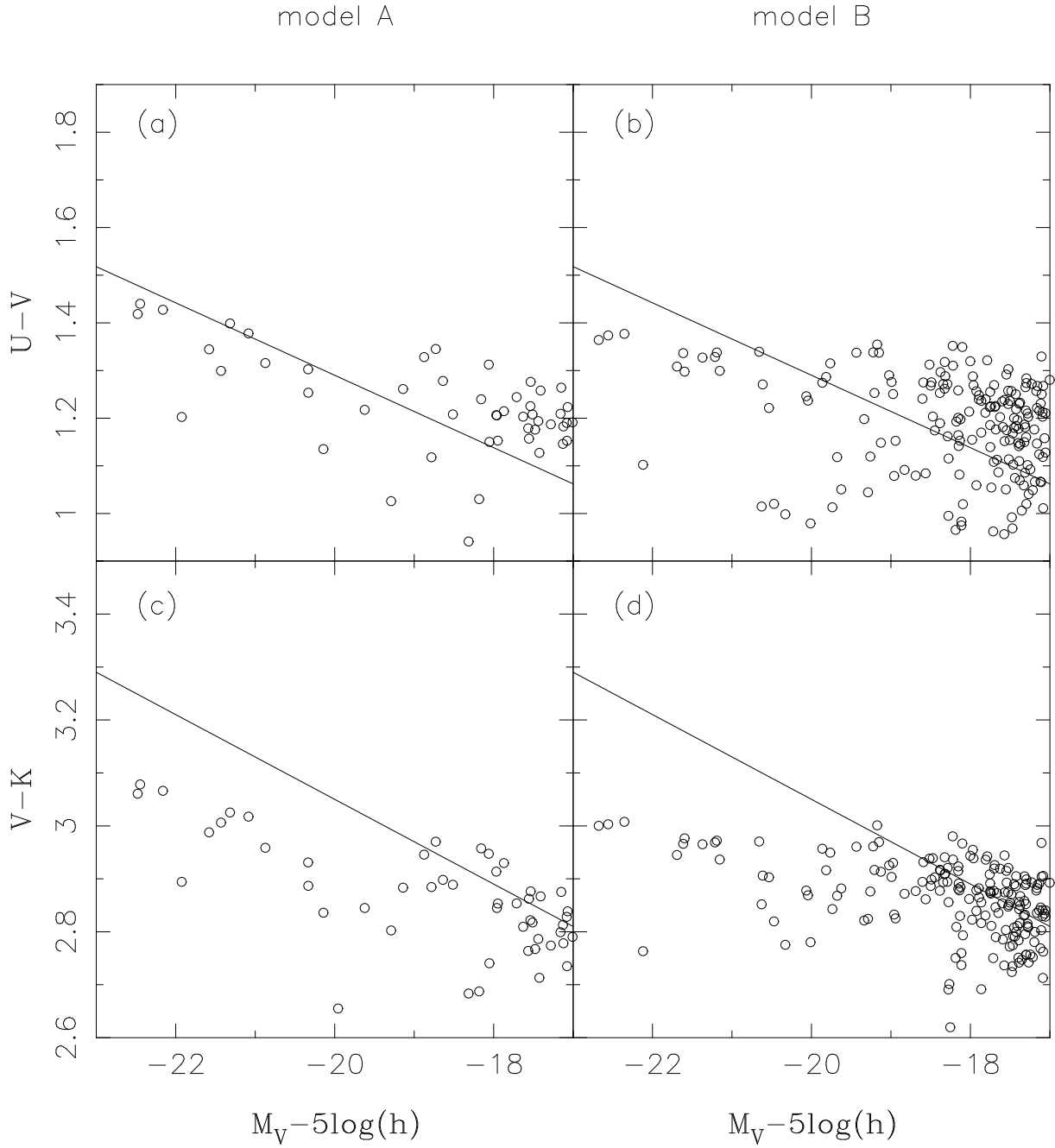


Figure 5.2: Colour-magnitude diagram of model A and B. (a) M_V v.s. $U - V$ in the model A. (b) Same as (a), but for the model B. (c) M_V v.s. $U - V$ in the model A. (d) Same as (c), but for the model B. The models are characterized in Table 1. The open circles denote galaxies identified as ellipticals. The solid lines show the observed CMRs (Bower et al. 1992).

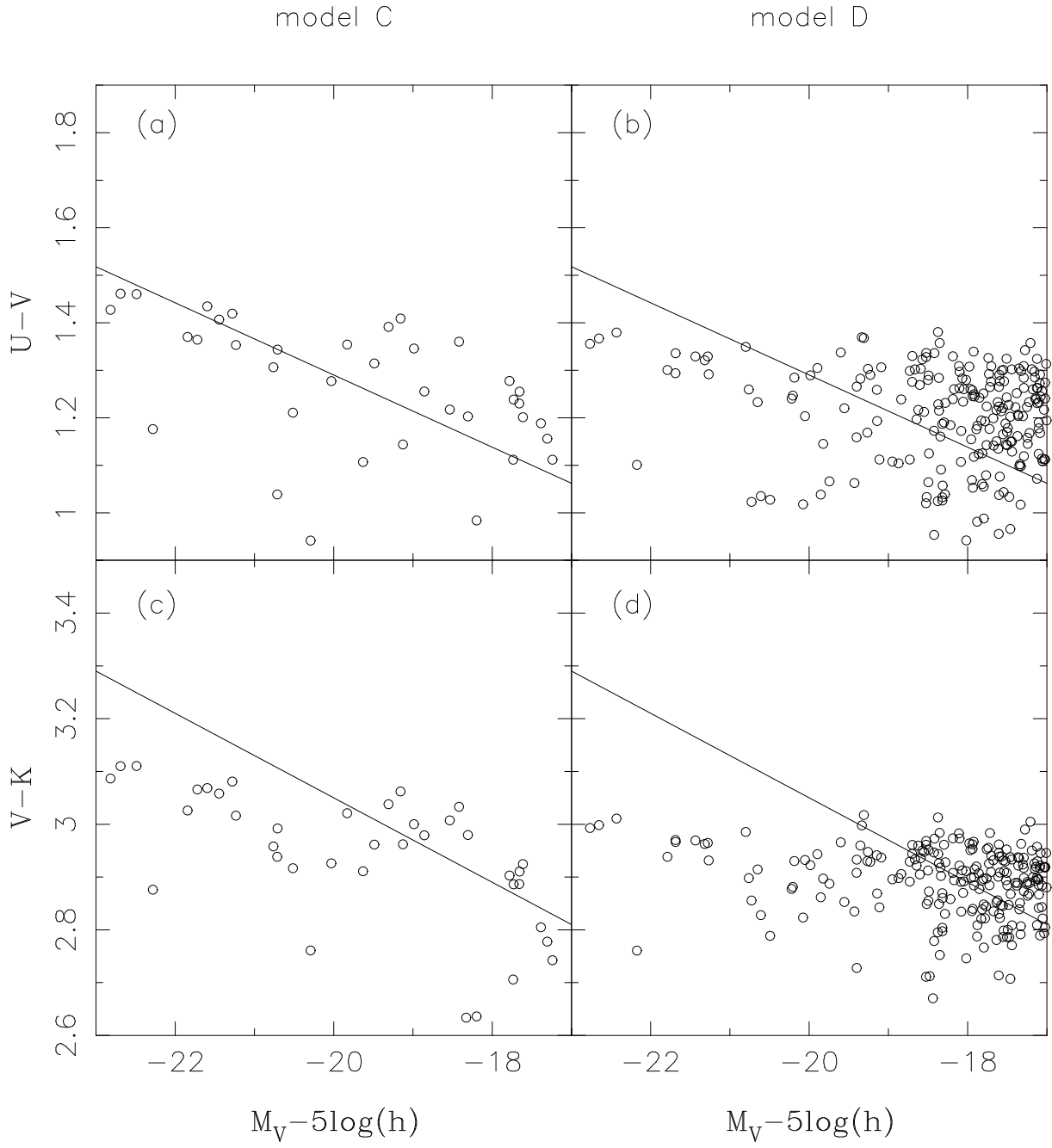


Figure 5.3: Same as Fig.5.2, but for model C and D.

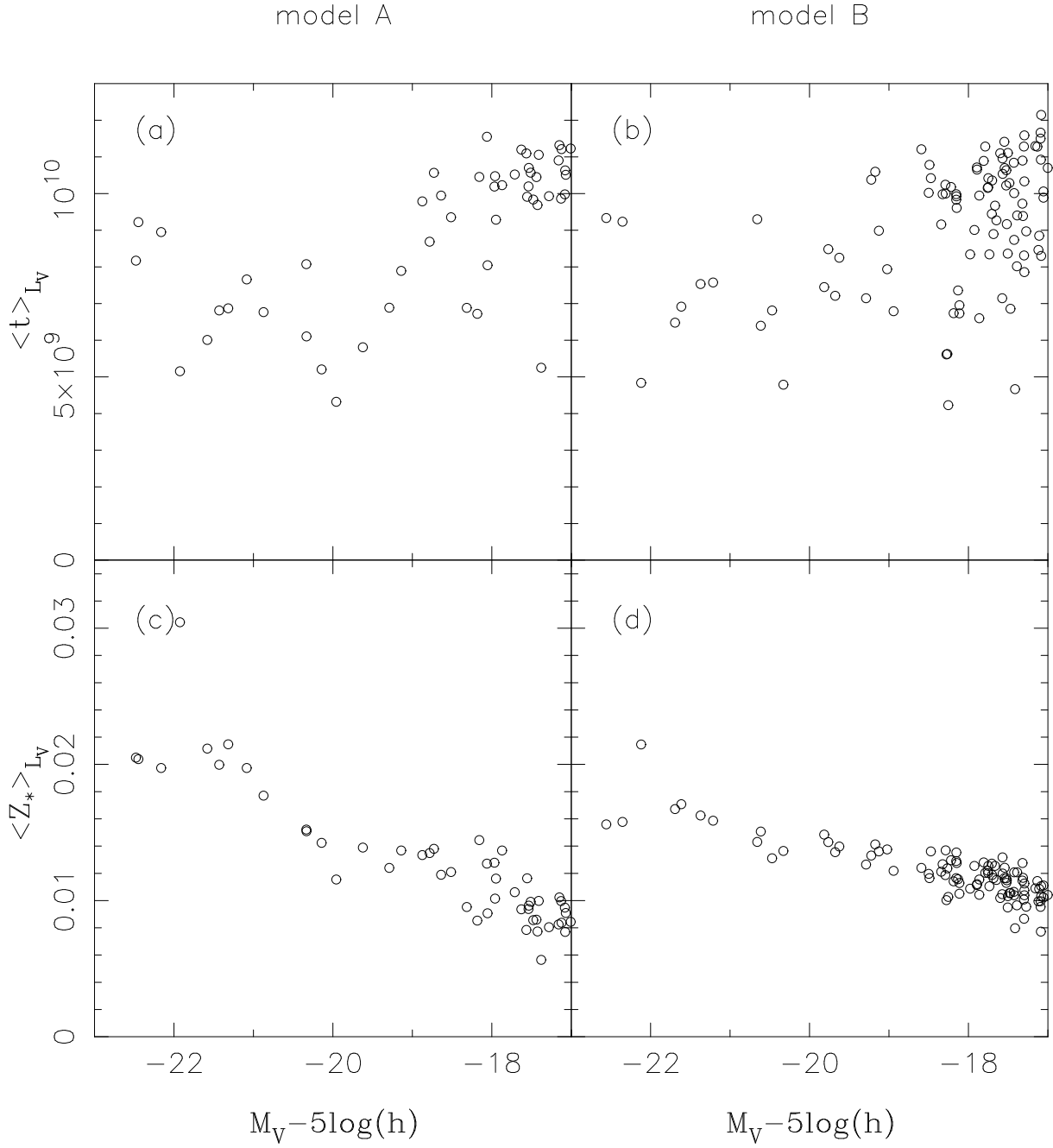


Figure 5.4: Upper panels: age-magnitude diagram. (a) Model A. (b) Model B. Lower panels: metallicity-magnitude diagram. (c) Model A. (d) Model B. The open circles denote elliptical galaxies.

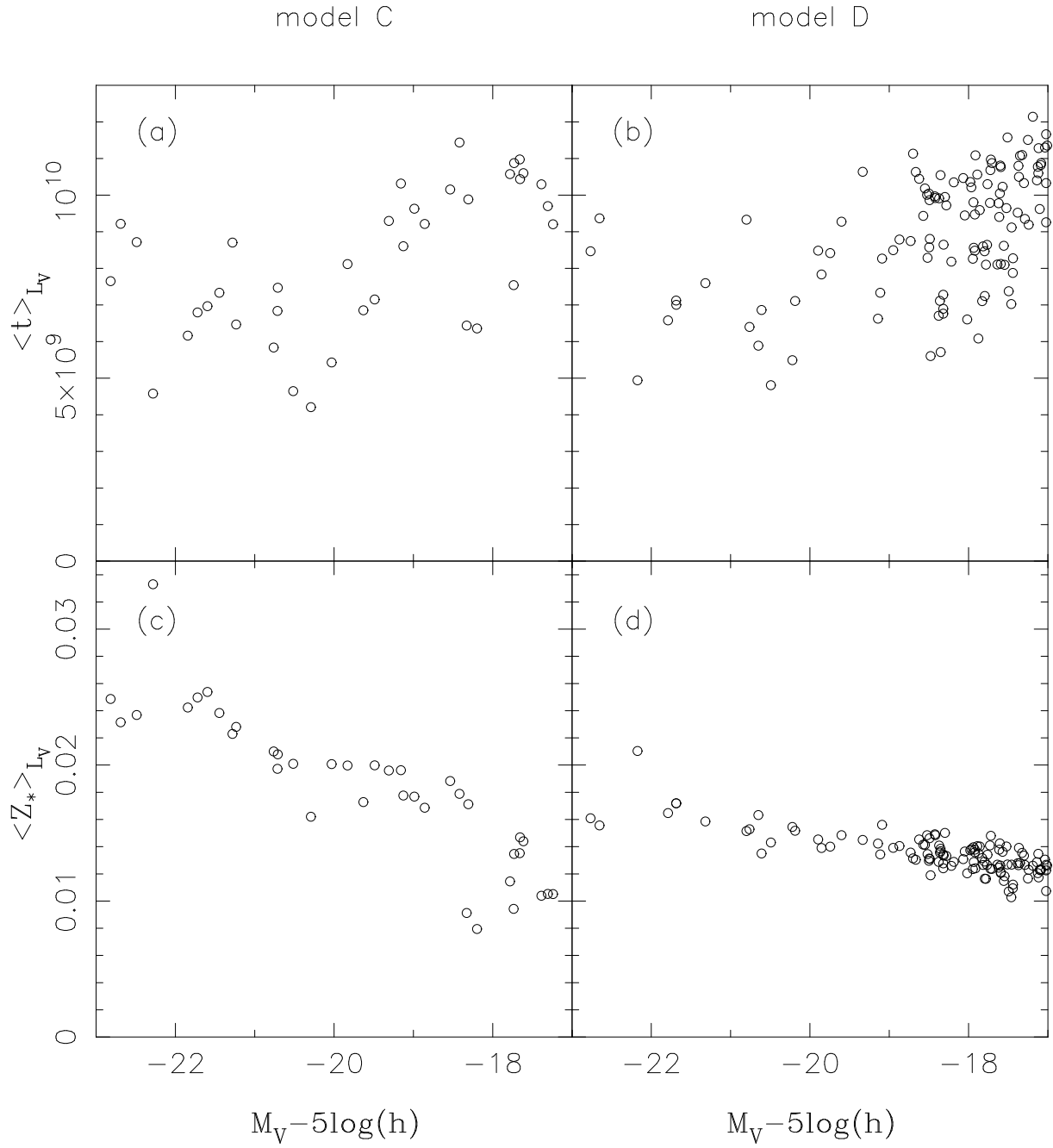


Figure 5.5: Same as Fig.5.4, but for model C and D.

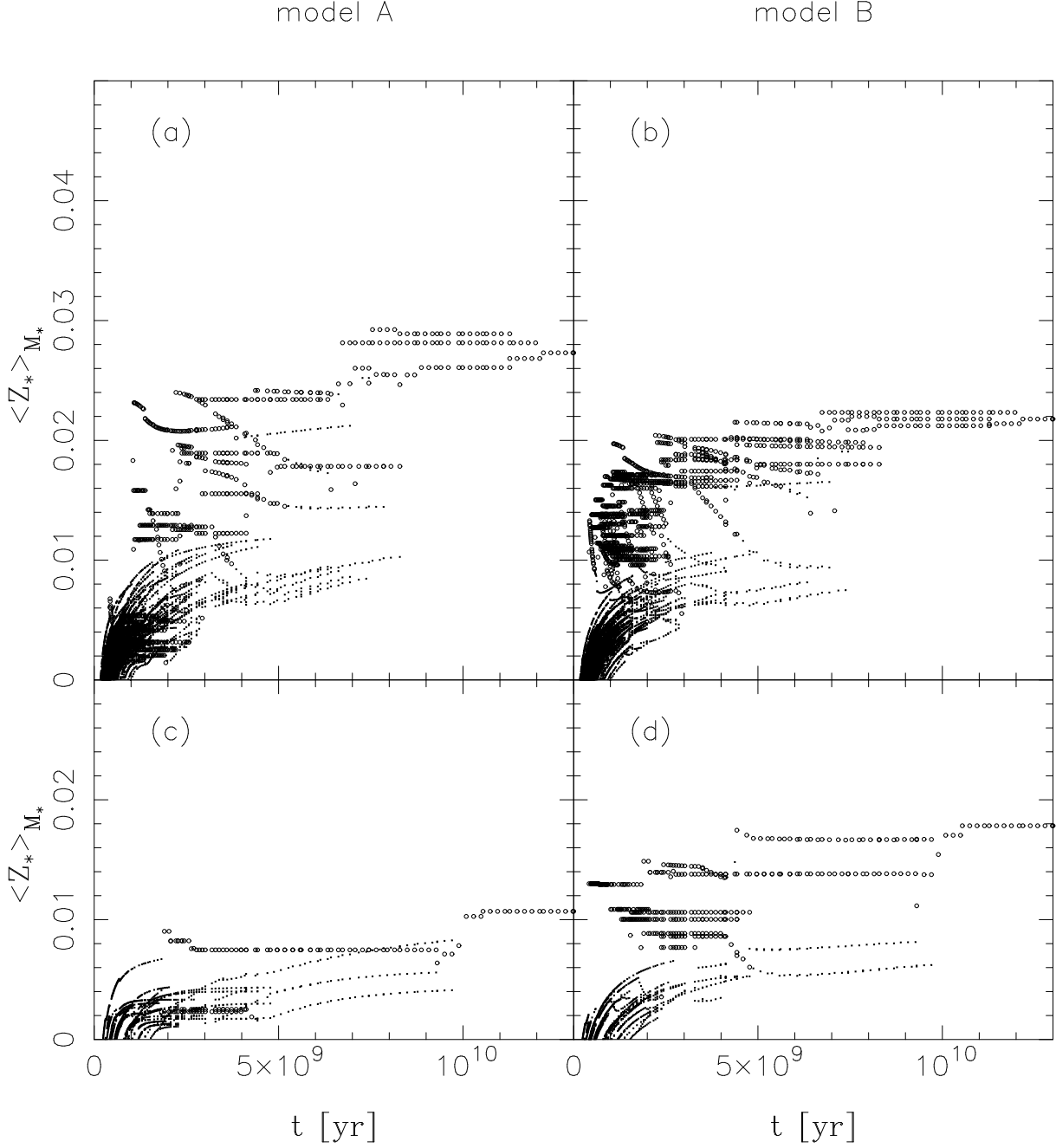


Figure 5.6: Evolution of mass-weighted mean stellar metallicity. Each symbol shows the mean metallicity of a progenitor at the time. The open circles denote progenitors in the *elliptical state*, and the dots the *spiral state*. These states are defined in the text. (a) A luminous elliptical in model A. $M_V = -24.1, U - V = 1.49, V - K = 3.12$. (b) A luminous elliptical in model B. $M_V = -23.9, U - V = 1.61, V - K = 3.23$. (c) A faint elliptical in model A. $M_V = -19.8, U - V = 1.02, V - K = 2.82$. (d) A faint elliptical in model B. $M_V = -20.5, U - V = 1.14, V - K = 3.10$.

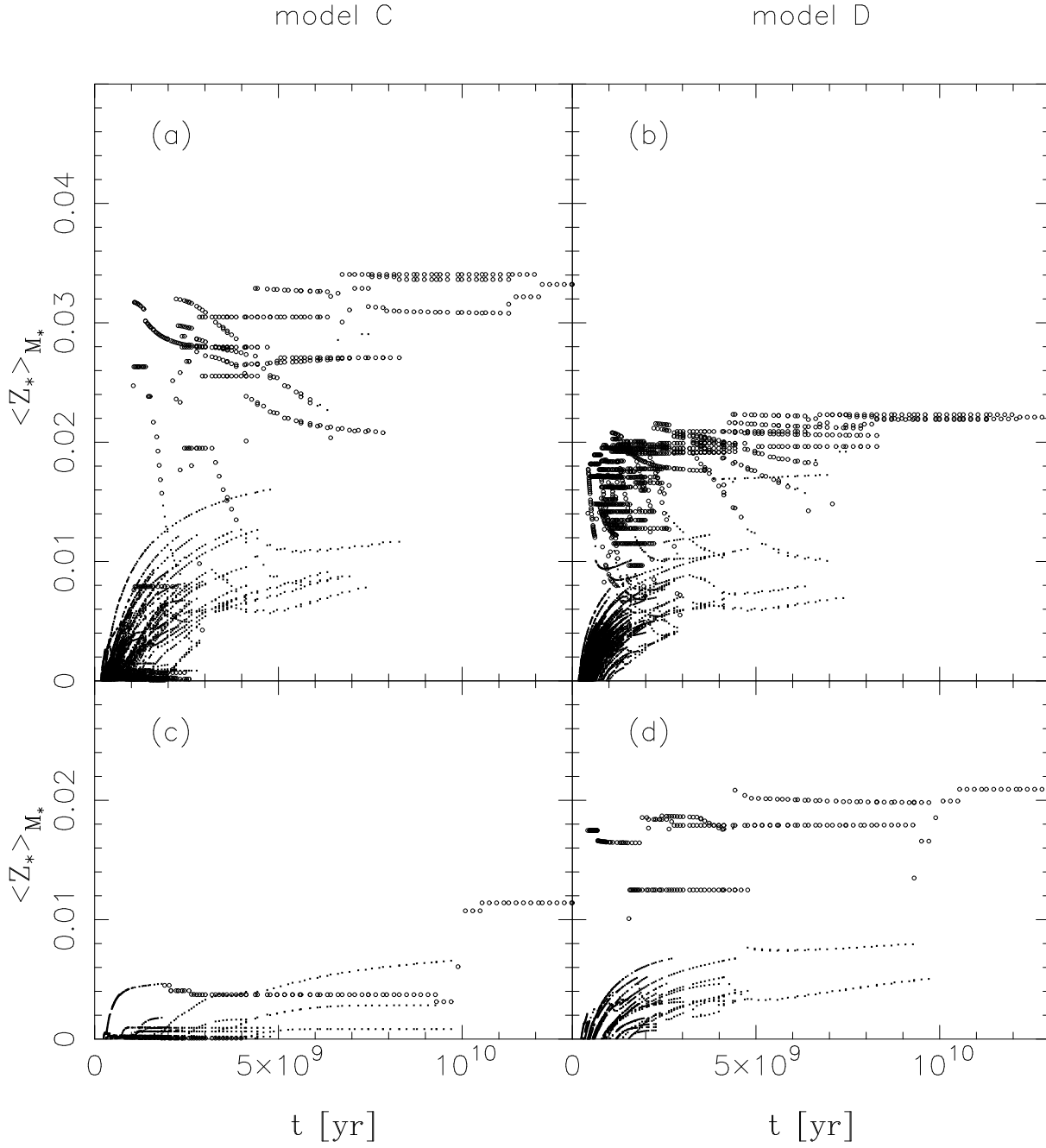


Figure 5.7: Same as Fig.5.6, but for model C and D. (a) $M_V = -24.4, U - V = 1.51, V - K = 3.15$ in model C. (b) $M_V = -24.0, U - V = 1.62, V - K = 3.24$ in model D. (c) $M_V = -19.9, U - V = 0.90, V - K = 2.66$ in model C. (d) $M_V = -20.4, U - V = 1.39, V - K = 3.18$.

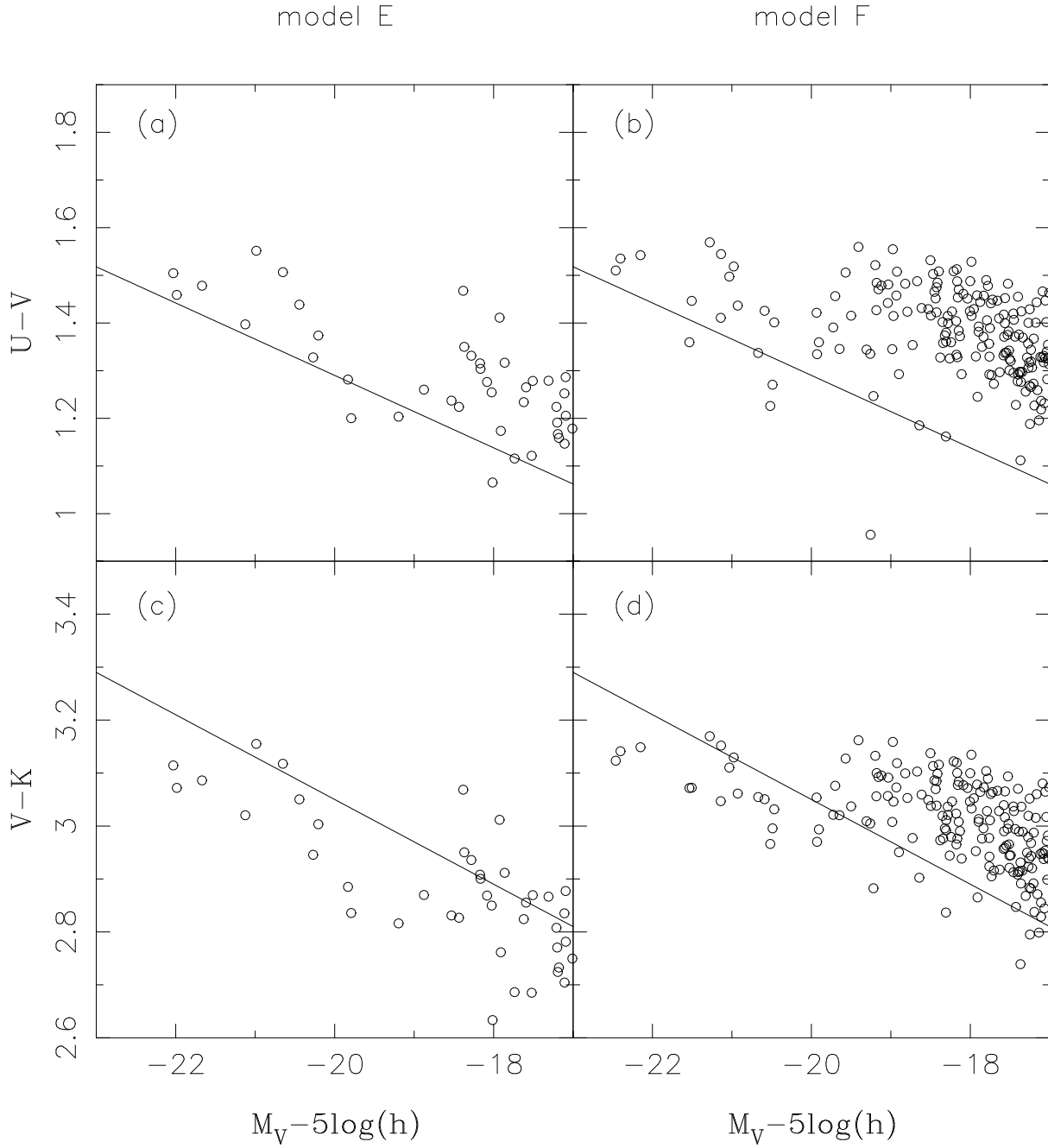


Figure 5.8: Same as Fig.5.2, but for model E and F. Both models have a short star formation timescale, $\tau_*^0 = 2$ Gyr. Model E: $V_{hot} = 600 \text{ km s}^{-1}$. Model F: $V_{hot} = 100 \text{ km s}^{-1}$.

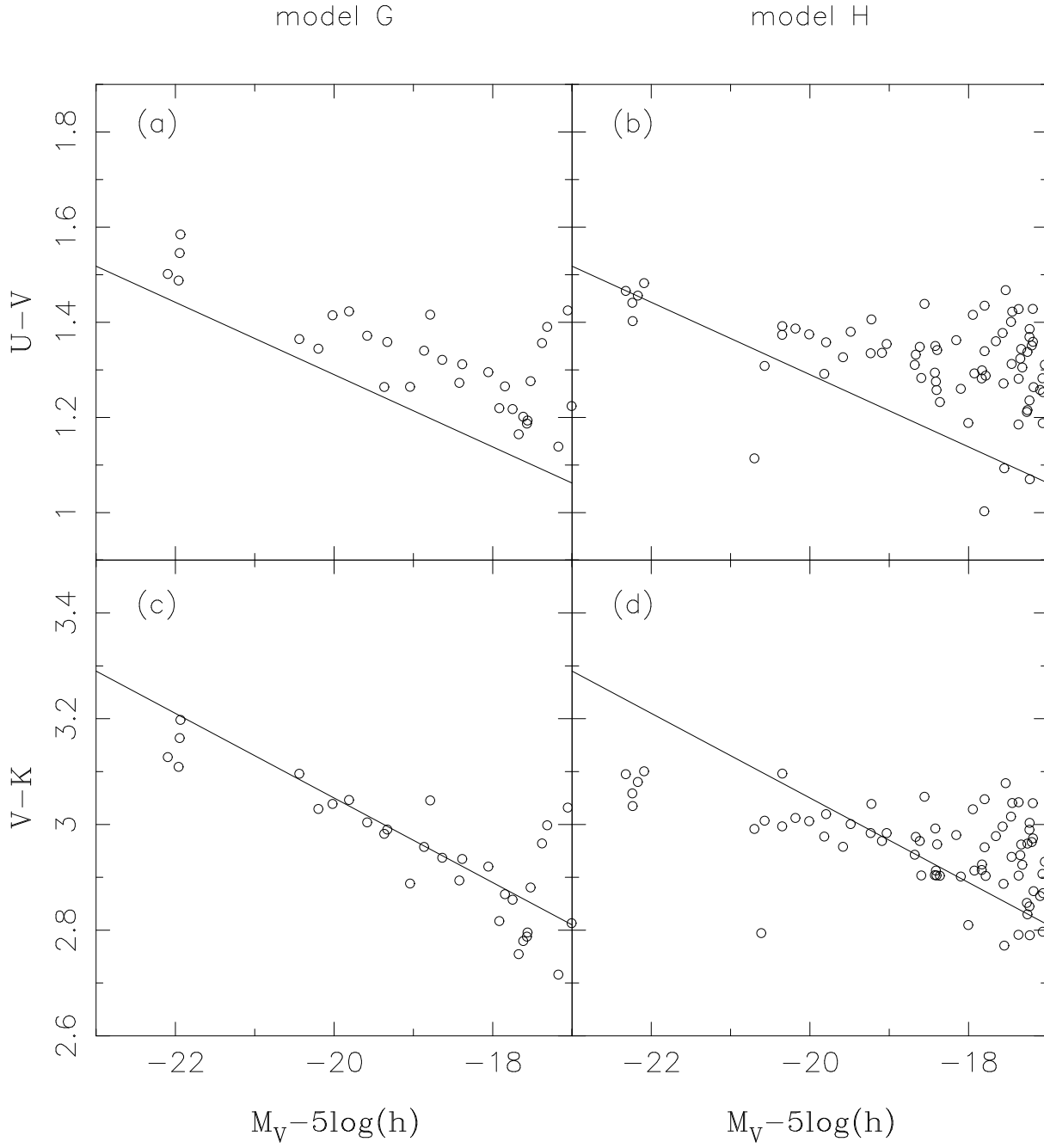


Figure 5.9: Same as Fig.5.2, but for model G and H. The effect of the UV background radiation is considered. Both models have a short star formation timescale, $\tau_*^0 = 2$ Gyr. Model G: $V_{hot} = 280 \text{ km s}^{-1}$. Model H: $V_{hot} = 100 \text{ km s}^{-1}$.

Chapter 6

Summary and prospects

In this thesis, we investigated the galaxy formation and evolution by a semi-analytic model, and the merging histories of dark haloes, on which the semi-analytic model is based.

As for the merging history of dark haloes, we show the role of the spatial correlation of density fluctuations in Chapter 2. We compare mass functions given by the merging cell model, which includes the spatial correlation of density fluctuations, with mass functions given by the Press-Schechter formalism and the block model. We find that the mass function suffers significant changes when the effect of the spatial correlation is considered.

Nevertheless, the Press-Schechter and block model are often used and have some evidence for justifying the models by N-body simulations. The reason why the mass functions given by these models are in rough agreement with those given by N-body simulations is not revealed. Probably one of the causes of this agreement are the ambiguity of the method of the identification of haloes in N-body simulations. There are some methods identifying the haloes, and usually clumps of particles in the box of N-body simulations are identified as haloes. Because of both the restricted resolution and a little ambiguous criterion for the judgment whether each particle belongs to a halo or not, the estimation of mass of haloes has an uncertainty. Another is a theoretical problem that both the spatial correlation and the non-spherical collapse of haloes should be considered simultaneously when we derive the mass function analytically. Through the improvement in the above problems, we will obtain the correct mass function. Moreover, it is not trivial that the methods constructing the merging histories by the extension of the PS formalism and the block model are correct even if the PS mass function is correct. Therefore we need to improve the method constructing the merging histories. However, we have not obtained the merging history model including the effects of the spatial correlation and the non-spherical collapse. So using the block model and an extension of the Press-Schechter model in this thesis, we analyze the effect of the UV background radiation on galaxy formation and the colour-magnitude relation of elliptical galaxies in clusters of galaxies.

In Chapter 4, we estimate the effect of the UV background radiation quantitatively. This effect has been neglected in the previous work by using the semi-analytic models. We find that the observed luminosity function is reproduced better by the model with the effect rather than that without the effect if a redshift evolution model of the UV background suggested by observation is adopted [case (4) in Chapter 4]. Moreover, our result is quite different from the

result given by the model which does not consider the merging histories of galaxies. This shows the importance of the analyses by the semi-analytic model.

Moreover, we suggest that the properties of the UV background will be determined by observing the luminosity function and colour distribution of galaxies. This may affect other studies which are strongly connected with the studies of the UV background, e.g., Ly- α clouds.

In Chapter 5, we investigate the colour-magnitude relation of elliptical galaxies. Varying the free parameters, we see the origin of the colour-magnitude relation, and find that it is essential for the relation to make a difference between stellar metallicities of luminous and faint galaxies. We find some solutions for suppressing the stellar metallicities in faint galaxies. One is the strong supernova feedback in faint galaxies. A few new stars explode and heat up a large quantity of the surrounding interstellar medium, so the stellar metallicity does not increase in the faint galaxies. Another solution is to consider the effect of the UV background. Because the UV photons penetrate more deeply in small clouds than in large clouds, the star formation is suppressed in the faint galaxies. So the faint galaxies do not evolve chemically. Since the degree of the chemical evolution is related to the star formation timescale, we find the relationship between the feedback, the UV background, and the star formation. In other words, we restrict the range of parameters to the hypersurface in the parameter space. This surface will be more restricted by comparing other quantities, e.g., the luminosity function and cold gas content, given by the model and observations.

As future work, we should mainly study about the following. One is to improve the method of constructing the merging histories in order to include the spatial correlation. If we obtain spatial information, we can utilize more observational results, e.g., morphology-density relation (Dressler 1980; Whitmore & Gilmore 1991), for investigating the galaxy formation. Second is to improve the model of star formation. In this thesis, we considered only atomic cooling, so the baryonic gas cools to only $\sim 10^4\text{K}$. In the actual star formation process, the gas should cool to $\sim 10^2\text{K}$ via molecular cooling. When we improve the model of photoionization by the UV background, it will be important to consider this process because the molecules are sensitive to the UV radiation. Third is to consider the satellite-satellite merger in a common halo. When considering the colour-magnitude relation, this effect may be important. For making the results in Chapter 5 more certain, this effect should be considered. Fourth is to include the effect of dust. This is considered by Somerville & Primack (1998) firstly in the semi-analytic model, and they show that the effect of dust is feasible for reproducing observations. Moreover, this effect gives us a clue to obtaining the information about star formation history. For applying the semi-analytic model to this problem, the infrared observations to see the emission from dust must be performed.

In this thesis, we considered only the standard CDM model as the cosmological model. Fixing the cosmological model, we investigate the dependence of observational quantities of galaxies on the baryonic processes such as cooling, star formation, supernova feedback, and so on. We will investigate how the cosmological parameters affect the formation and evolution process of galaxies because recent observations suggest that the Universe has either a negative curvature or a non-zero cosmological constant, rather than the standard CDM model. Furthermore we will investigate how the physical processes connect with various observational quantities as well as the luminosity function, the colour distribution, and the colour-magnitude relation. The galaxy formation will be deeply understood through such a study.

In near future, observations of galaxies will be developed by the SUBARU 8m telescope, several satellites (X-ray, Infrared), and a very large millimeter and submillimeter interferometer (LMSA project) in Japan. We believe that the importance of the semi-analytic method which is able to compare theory with observation will increase for studying the galaxy formation.

Appendix A

Effects of spatial correlations on mass function

A.1 THE PS FORMALISM

In this section, we review briefly the PS formalism. In the standard cosmological models, we assume that initial small density fluctuations are the seeds of cosmic structures such as galaxies and that they obey a random Gaussian distribution. Then the probability distribution function for the Fourier components of density fluctuations $\delta_{\mathbf{k}}$, is given by BBKS(1986)

$$P(|\delta_{\mathbf{k}}|, \phi_{\mathbf{k}}) d|\delta_{\mathbf{k}}| d\phi_{\mathbf{k}} = \frac{2|\delta_{\mathbf{k}}|}{P(k)} \exp\left\{-\frac{|\delta_{\mathbf{k}}|^2}{P(k)}\right\} d|\delta_{\mathbf{k}}| \frac{d\phi_{\mathbf{k}}}{2\pi}, \quad (\text{A.1})$$

where $\phi_{\mathbf{k}}$ is the random phase of $\delta_{\mathbf{k}}$ and $P(k)$ is the power spectrum.

In general, we assume that the density fluctuations associated with objects of mass scale M are given by the filtered density fluctuations defined as follows;

$$\delta_M(\mathbf{x}) = \frac{V}{(2\pi)^3} \int_0^\infty \delta_{\mathbf{k}} e^{i\mathbf{k}\cdot\mathbf{x}} W(k, R(M)) d^3\mathbf{k}, \quad (\text{A.2})$$

$$R(M) = \left(\frac{3M}{4\pi\bar{\rho}}\right)^{1/3}, \quad (\text{A.3})$$

where $W(k, R(M))$ is the window function and $\bar{\rho}$ is the mean density.

We use the window function given by

$$W(k, R(M)) = \begin{cases} 1 & (k \leq k_c(M)) \\ 0 & (k > k_c(M)) \end{cases} \quad (\text{A.4})$$

$$k_c(M) = \frac{\pi}{R(M)}, \quad (\text{A.5})$$

the so-called "sharp k -space filter".

In this Appendix, we consider only this filter for simplicity. If we choose other filters, the results will change quantitatively.

The linear density fluctuation δ_M grows as time increases and it is considered that objects of mass scale M have collapsed and virialised at last when this fluctuation δ_M reaches the critical overdensity δ_c . It is well known that the critical overdensity is $\delta_c \simeq 1.69$ for spherical collapse in a flat universe (Peebles 1993; see Appendix D). Throughout this Appendix, we consider only the spherically symmetric case. In other cases, the critical density has similar values.

As suggested in Peacock & Heavens (1990) and Jedamzik (1995), the probability $f(> \delta_c, M)$ of finding a region of mass scale M , in which the linear density fluctuation δ_M is greater than or equal to the critical overdensity δ_c , is given by an integral over the tail of a Gaussian distribution function,

$$f(> \delta_c, M) = \int_{\delta_c}^{\infty} \frac{1}{\sqrt{2\pi\sigma^2(M)}} \exp\left\{-\frac{\delta^2}{2\sigma^2(M)}\right\} d\delta, \quad (\text{A.6})$$

since linear density fluctuations δ_M are themselves Gaussian random processes. Here the variance $\sigma^2(M)$ is estimated by summing up the variance of each Fourier component in the sharp k -space filter as follows:

$$\sigma^2(M) = \frac{V}{(2\pi)^3} \int_0^{k_c(M)} |\delta_k|^2 4\pi k^2 dk, \quad (\text{A.7})$$

$$k_c(M) = \pi / \left(\frac{3M}{4\pi\bar{\rho}}\right)^{1/3}. \quad (\text{A.8})$$

If we assume a simple power law, $P(k) \propto k^n$, the variance $\sigma^2(M)$ becomes

$$\sigma^2(M) = \left(\frac{M}{M_*}\right)^{-\frac{(n+3)}{3}}, \quad (\text{A.9})$$

where M_* is the characteristic mass scale such that $\sigma^2(M_*) = 1$.

In the PS formalism, $f(> \delta_c, M)$ is considered to be proportional to the probability that collapsed objects of mass scales greater than M appear at a given point. If $\delta_M > \delta_c$ for a given mass M at a point, then it will have $\delta_{M'} = \delta_c$ when filtered on some larger mass scale $M'(> M)$ and so it will be counted as the collapsed object of the larger mass scale M' . In this argument, it is assumed that the *isolated* collapsed objects that exist at a given epoch are those that have just collapsed ($\delta_M = \delta_c$). Thus the mass function $n(M)$ (defined such that $n(M)dM$ is the comoving number density of the collapsed objects in the range dM) is given by

$$\frac{M}{\bar{\rho}} n(M) = \left| \frac{df}{dM} \right| = \frac{\delta_c}{\sqrt{2\pi}\sigma} \frac{1}{M} \left| \frac{d\ln\sigma}{d\ln M} \right| \exp\left(-\frac{1}{2}\delta_c^2/\sigma^2\right), \quad (\text{A.10})$$

where only half the mass of the initial density fluctuations is associated, which is eventually to be collapsed. The problem is that half the mass, which is initially present in underdense regions, remains unaccounted for.

As noted earlier, Press & Schechter *simply* multiply the probability by a factor of 2 without giving clear physical reasons;

$$n(M) = 2 \frac{\bar{\rho}}{M} \left| \frac{df}{dM} \right| \equiv n_{ps}. \quad (\text{A.11})$$

This factor of 2 has long been noted as a weak point in the PS formalism. The problem of counting correctly the underdense regions that are embedded with overdense regions is the "cloud-in-cloud" problem as we mentioned before. Peacock & Heavens(1990) and Bond et al.(1991) proposed a solution to the cloud-in-cloud problem in taking into account the probability, P_{up} , that subsequent filtering with larger scales might at some points result in having $\delta > \delta_c$, even when at smaller filter $\delta < \delta_c$. *Surprisingly*, using the sharp k -space filter, it is found that the factor 2 in the PS formalism is correct. However this factor is incorrect if using other filters.

A.2 JEDAMZIK FORMALISM

Jedamzik(1995) proposed another approach to the cloud-in-cloud problem. We will explain his approach below; the goal is to compute the number density of *isolated* regions. Isolated regions of mass scale M are regions that have collapsed but that are not included in yet larger regions in which the linear density fluctuation is greater than or equal to the critical overdensity δ_c . In particular, a region of mass scale M will be counted only as an eventually virialised object of mass M , if for any larger mass scale the average overdense of the region is below the critical density. Therefore the density fluctuation of an isolated region is just the critical density δ_c because a region with $\delta > \delta_c$ would be counted eventually as an object of larger scale.

Following Jedamzik (1995), let us define the conditional probability $P(M_1, M_2)$ of finding a region of mass scale M_1 in which δ_{M_1} is greater than or equal to δ_c , provided it is included in an isolated overdense region of mass scale M_2 . Then the volume ratio $f(> \delta_c, M_1)$ of finding a region of mass scale M_1 that is overdense by δ_c or more is given by the following integral form:

$$f(> \delta_c, M_1) = \int_0^\infty dM_2 n(M_2) \frac{M_2}{\bar{\rho}} P(M_1, M_2). \quad (\text{A.12})$$

Here $n(M)$ is the number density(*i.e.* the mass function) of isolated objects of mass scale M . If we can calculate $P(M_1, M_2)$ in any case, we can then obtain the mass function $n(M)$ using this formula without worrying about the cloud-in-cloud problem (we call this approach the Jedamzik formalism).

By definition, the conditional probability must satisfy $P(M, M') = 0$ for $M > M'$. If $P(M, M')$ had, in any case, the property $P(M, M') = 1$ for $M \leq M'$, then

$$\left| \frac{df}{dM} \right| = \frac{M}{\bar{\rho}} n(M), \quad (\text{A.13})$$

where we use the relation $dP(M, M')/dM = -\delta(M - M')$. Eventually we obtain

$$n(M) = \frac{\bar{\rho}}{M} \left| \frac{df}{dM} \right|. \quad (\text{A.14})$$

This is the original PS formula without the factor of 2. However this expression does not hold in general.

Now in the sharp k -space filter, we find

$$\begin{aligned}
 P(M, M') &= P(\delta_M \geq \delta_c | \delta_{M'} = \delta_c) \\
 &= \int_{\delta_c}^{\infty} d\delta_M \frac{1}{\sqrt{2\pi}} \frac{1}{\sigma_{sub}} \exp \left\{ -\frac{1}{2} \frac{(\delta_M - \delta_c)^2}{\sigma_{sub}^2} \right\} \\
 &= \frac{1}{2},
 \end{aligned} \tag{A.15}$$

where

$$\begin{aligned}
 \sigma_{sub}^2 &= \sigma^2(M) - \sigma^2(M') \\
 &= \left(\frac{M}{M_*} \right)^{-(\frac{3+n}{3})} - \left(\frac{M'}{M_*} \right)^{-(\frac{3+n}{3})}.
 \end{aligned} \tag{A.16}$$

Here we use the fact that regions with mass M' are isolated ones, *i.e.*, $\delta_{M'} = \delta_c$. It must be noted that eq.(A.15) is satisfied only in the sharp k -space filter (see Section A.4).

Then since $dP(M, M')/dM = -\frac{1}{2}\delta(M - M')$, from eq.(A.12), we have

$$\left| \frac{df}{dM} \right| = \frac{1}{2} \frac{M}{\bar{\rho}} n(M) \tag{A.17}$$

and so

$$n(M) = 2 \frac{\bar{\rho}}{M} \left| \frac{df}{dM} \right|. \tag{A.18}$$

This is just the PS mass function including the factor of 2. In conclusion, we show that the Jedamzik formalism could also give the factor of 2 provided that the conditional probability has, as derived by using the sharp k -space filter, the form of eq.(A.15). Because Jedamzik(1995) used a different conditional probability from ours in the case of the sharp k -space filter, he derived a different result in which the factor of 2 was incorrect. As mentioned before, δ_M should be just δ_c in the isolated region, where δ_M means the smoothed density field with mass scale M . It is the same condition as in Peacock & Heavens(1990) and Bond et al.(1991). If an object has $\delta_M > \delta_c$, the object will collapse with a larger mass $M'(> M)$, for which $\delta_{M'} = \delta_c$. Therefore the object is not isolated by definition and then it is reasonable to consider that the condition of the isolated object is $\delta_M = \delta_c$. But, Jedamzik claims that the condition $\delta_M \geq \delta_c$ might be allowable even in an *isolated* region of mass scale M . The reason for which he uses this specific condition is that an isolated region may have $\delta_M > \delta_c$ in the real world. He believes that in both the results of N-body simulations and the real world, virialised objects identified to have mass M may be associated with primordial perturbations covering a range of initial density fluctuations $\delta_M \geq \delta_c$. However, we do not think that this reason is *mathematically* reasonable and that this condition is consistent with the definition of the *isolated* region although his results are almost consistent with the numerical results. Moreover he also has recognized in his paper that the result of Peacock and Heavens or that of Bond et al. would be recovered by using our definition of the conditional probability [eq.(A.15)], which is mathematically consistent with the definition of the isolated regions when we analyze the mass function by the above approach (using the conditional probability). We believe rather that when we follow the same procedure as that of Press and Schechter, making the assumptions of random Gaussian fields,

the spherically symmetric collapse and the same definition of the isolated collapsed object, the isolated collapsed object should have $\delta_M = \delta_c$, which is mathematically correct and consistent with the definition of *isolated* regions.

However the Jedamzik formula eq.(A.12) is very useful for the analysis of the mass function including the spatial correlations for the cloud-in-cloud problem. If we can obtain the conditional probability $P(M, M')$ taking into account the spatial correlations, we can estimate the mass function by solving the integral equation [eqs.(A.12) and (A.13)].

A.3 SPATIAL CORRELATION

Authors of previous works have considered the probability of density fluctuations without considering explicitly the spatial two-point correlations of these fluctuations. In reality, however, an object of mass scale M will have a finite size and will include other objects in this finite region. So we have to consider the two-point correlation function in order to analyze whether the objects of smaller mass scale M_1 are included in the region of the object of a larger mass scale M_2 . We believe that it is necessary to consider spatial correlations in order to solve the cloud-in-cloud problem correctly.

At first, we consider the following conditional probability for simplicity in order to analyze only the effect of the spatial correlations on the PS formalism. In this section we neglect the condition that an isolated object should have a maximum peak of density fluctuations in estimating the conditional probability. In the next section, however, the conditional probability with the additional condition of having the maximum peak will be considered for estimating the *correct* mass function, though the form of the probability is complicated. In estimating the conditional probability $P(M_1, M_2)$, we consider, at first, the conditional probability, $P(r, M_1, M_2)$, of finding a region of mass scale M_1 that is overdense by δ_c or more at a distance r from the center ($r = 0$) of an isolated object of mass scale M_2 , provided that the object of mass scale M_1 is included in the object of mass scale $M_2 (> M_1)$ with a finite size and $\delta_{M_2} = \delta_c$ at $r = 0$. As we will show below, this conditional probability is adequate to analyze the effects of spatial correlations although the condition that δ_{M_2} has the maximum peak density is neglected (see Section A.5).

We found that $P(r, M_1, M_2)$ is equivalent to the constrained probability defined as follows (BBKS: this corresponds to the Gaussian distribution for two-variables $(\delta_{M_1}(r), \delta_{M_2})$). The general form for m -variables is shown in the Appendix A; the covariance matrix \mathbf{M} is

$$\mathbf{M} = \begin{pmatrix} \sigma_1^2 & \sigma_c^2(r) \\ \sigma_c^2(r) & \sigma_2^2 \end{pmatrix}, \quad (\text{A.19})$$

so,

$$\begin{aligned} P(r, M_1, M_2) &= P(\delta_{M_1}(r) > \delta_c | \delta_{M_2} = \delta_c) \\ &= \frac{P(\delta_{M_1}(r) > \delta_c, \delta_{M_2} = \delta_c)}{P(\delta_{M_2} = \delta_c)} \\ &= \frac{1}{\sqrt{2\pi(1 - \varepsilon^2(r))}} \int_{\nu_{1c}}^{\infty} \exp\left[-\frac{(\nu_1 - \varepsilon(r)\nu_{2c})^2}{2(1 - \varepsilon^2(r))}\right] d\nu_1 \end{aligned} \quad (\text{A.20})$$

where ν_1 and ν_2 are defined by

$$\nu_1 \equiv \frac{\delta_1}{\sigma_1}, \nu_2 \equiv \frac{\delta_2}{\sigma_2}, \sigma_1 \equiv \sigma(M_1), \sigma_2 \equiv \sigma(M_2), \nu_{1c} = \frac{\delta_c}{\sigma_1}, \nu_{2c} = \frac{\delta_c}{\sigma_2} \quad (\text{A.21})$$

and $\varepsilon(r)$ is defined by

$$\varepsilon(r) \equiv \frac{\sigma_c^2(r)}{\sigma_1 \sigma_2}, \quad (\text{A.22})$$

$$\begin{aligned} \sigma_c^2(r) &= \langle \delta_{M_2}(\mathbf{r}_0) \delta_{M_1}(\mathbf{r}_0 + \mathbf{r}) \rangle \\ &= \frac{V}{(2\pi)^3} \int_0^{k_c(M_2)} |\delta_k|^2 \frac{\sin(kr)}{kr} 4\pi k^2 dk, \end{aligned} \quad (\text{A.23})$$

which corresponds to the two-point correlation function. For convenience, we define $\alpha(r)$ as

$$\alpha(r) \equiv \frac{\varepsilon(r)}{\varepsilon(0)}. \quad (\text{A.24})$$

Here $\sigma_c^2(0)$ is then the cross-correlation of the density fluctuations on the mass scale M_1 and on the mass scale M_2 at the same point. Since we use a sharp k -space filter, the cross-correlation is the same as the variance of the density fluctuation filtered with the larger mass scale. Therefore, $\sigma_c^2(0)$ is equal to the variance σ_2^2 . Then, in the case of the sharp k -space filter, $\varepsilon(0) = \sigma_2/\sigma_1$. Inserting this relation into eq.(A.20) and putting $r = 0$ at eq.(A.20), we can obtain the conditional probability $P(M_1, M_2)$ at one point as follows;

$$\begin{aligned} P(r=0, M_1, M_2) &= \frac{1}{\sqrt{2\pi(1-\varepsilon^2(0))}} \int_{\nu_{1c}}^{\infty} \exp\left[-\frac{(\nu_1 - \varepsilon(0)\nu_{2c})^2}{2(1-\varepsilon^2(0))}\right] d\nu_1 \\ &= \frac{1}{\sqrt{2\pi(\sigma_1^2 - \sigma_2^2)}} \int_{\delta_{1c}}^{\infty} \exp\left[-\frac{(\delta_1 - \delta_{2c})^2}{2(\sigma_1^2 - \sigma_2^2)}\right] d\delta_1 \\ &= \frac{1}{2}. \end{aligned} \quad (\text{A.25})$$

This equation is the same as eq.(A.15), which is correct only in the case of the sharp k -space filter and in neglecting the spatial correlations.

The conditional probability eq.(A.20) is rewritten by

$$P(r, M_1, M_2) = \frac{1}{\sqrt{2\pi}} \int_{\beta(r)}^{\infty} e^{-\frac{y^2}{2}} dy, \quad (\text{A.26})$$

where

$$\beta(r) \equiv \frac{\nu_{1c} - \varepsilon(r)\nu_{2c}}{\sqrt{1-\varepsilon^2(r)}} = \frac{\delta_c}{\sigma_1} \frac{1-\alpha(r)}{\sqrt{1-\varepsilon^2(0)\alpha^2(r)}}, \quad (\text{A.27})$$

$$y \equiv \frac{\nu_1 - \varepsilon(0)\alpha(r)\nu_{2c}}{\sqrt{1-\varepsilon^2(0)\alpha^2(r)}}. \quad (\text{A.28})$$

Now we consider the spatial averaged conditional probability $P(M_1, M_2)$ defined as

$$\begin{aligned} P(M_1, M_2) &\equiv \int_0^R P(r, M_1, M_2) 4\pi r^2 dr / \int_0^R 4\pi r^2 dr \\ &\equiv \frac{1}{\sqrt{2\pi}} \int_{\bar{\beta}}^{\infty} e^{-\frac{y^2}{2}} dy, \end{aligned} \quad (\text{A.29})$$

where $R = R_2 = (3M_2/4\pi\bar{\rho})^{1/3}$ and

$$\bar{\beta} \equiv \frac{1}{\sqrt{1 - \varepsilon^2(0)\bar{\alpha}^2}} \frac{\delta_c}{\sigma_1} (1 - \bar{\alpha}) = \frac{1}{\sqrt{1 - (\frac{M_2}{M_1})^{-\frac{n+3}{3}} \bar{\alpha}^2}} \left(\frac{\delta_c}{\sigma_1}\right) (1 - \bar{\alpha}). \quad (\text{A.30})$$

Eqs.(A.28) and (A.29) give the definitions of the constant values, $\bar{\beta}$ and $\bar{\alpha}$, respectively. Then after the calculation of this conditional probability in any case, we can solve the mass function by substituting this probability into the integral equations (A.12) and (A.13). If we neglect the spatial correlation, then $\alpha(r) = \alpha(0) = 1, \beta(r) = 0$ and so $\bar{\beta} = 0, P(M_1, M_2) = 1/2$. Hence, we can again obtain the PS mass function.

Fig.A.1 shows the mass function that is estimated numerically following the above procedure for $n = 0$; also shown is the PS mass function. Fig.A.2 is the same as Fig.A.1, but for $n = -2$. We can clearly see the difference between both mass functions on some scales.

Here we show also the approximately estimated mass function in the extreme cases such as very small mass or very large mass scales in order to clarify analytically the difference with the PS mass function; Although $\bar{\alpha}$ is between 0 and 1 and its value depends on the power spectrum, we find that $\bar{\alpha}$ is in general approximately equal to 0.5 (for $-2 \lesssim n \lesssim 2$). When the mass scale M_1 is much less than the mass scale M_2 , $(\frac{M_2}{M_1})^{-\frac{n+3}{3}} \bar{\alpha}^2$ is much less than unity (for hierarchical clustering $n > -3$). In these cases, we can approximate that

$$\bar{\beta} \sim \frac{\delta_c}{\sigma_1} (1 - \bar{\alpha}). \quad (\text{A.31})$$

Even when the mass scale M_1 is nearly equal to the mass scale M_2 , the error of $\bar{\beta}$ is at most 10%. It will be shown below that this approximation is good.

Then we obtain the following conditional probability with good accuracy:

$$P(M, M') \begin{cases} \equiv g(M) = \frac{1}{\sqrt{2\pi}} \int_{\bar{\beta}}^{\infty} e^{-\frac{y^2}{2}} dy & (M \leq M') \\ = 0 & (M > M') \end{cases} \quad (\text{A.32})$$

where $\bar{\beta} = \frac{\delta_c}{\sigma(M)} (1 - \bar{\alpha})$.

Using the Jedamzik formalism [eq.(A.12)],

$$\frac{f(> \delta_c, M)}{g(M)} = \frac{1}{\bar{\rho}} \int_0^{\infty} dM' M' n(M') \frac{P(M, M')}{g(M)}. \quad (\text{A.33})$$

with

$$\frac{P(M, M')}{g(M)} = \begin{cases} 1 & (M \leq M') \\ 0 & (M > M') \end{cases} \quad (\text{A.34})$$

We can then obtain the following equation,

$$\left| \frac{d}{dM} \left\{ \frac{f}{g} \right\} \right| = \frac{1}{\bar{\rho}} M n(M), \quad (\text{A.35})$$

since $d\{\frac{P}{g}\}/dM = -\delta(M - M')$.

Now we estimate the mass function in two extreme cases. First, we consider the small mass scale ranges of the mass function ($M \ll M_*$; $\sigma(M_*) = 1$). In this case, we can use the relation such as $\delta_c/\sigma(M) \ll 1$ (for the hierarchical clustering $n > -3$). Then

$$f = \frac{1}{\sqrt{2\pi}} \int_{\frac{\delta_c}{\sigma(M)}}^{\infty} e^{-\frac{y^2}{2}} dy \sim \frac{1}{2} - \frac{1}{\sqrt{2\pi}} \frac{\delta_c}{\sigma(M)} \quad (\text{A.36})$$

$$g = \frac{1}{\sqrt{2\pi}} \int_{\frac{\delta_c}{\sigma(M)}(1-\bar{\alpha})}^{\infty} e^{-\frac{y^2}{2}} dy \sim \frac{1}{2} - \frac{1}{\sqrt{2\pi}} \frac{\delta_c}{\sigma(M)} (1-\bar{\alpha}). \quad (\text{A.37})$$

In order to see the difference between the modified mass function and the PS mass function n_{ps} , we examine the following ratio,

$$\begin{aligned} \frac{d}{dM} \left\{ \frac{f}{g} \right\} / \frac{2df}{dM} \Big|_{f=1/2} &= \frac{d(\frac{f}{g})}{2df} \Big|_{f=1/2} \\ &= \frac{\bar{\alpha}/2}{2\{(1-\bar{\alpha})f + \bar{\alpha}/2\}^2} \Big|_{f=1/2} = \bar{\alpha}. \end{aligned} \quad (\text{A.38})$$

Next, we consider larger mass scale ranges of the mass function ($M \gg M_*$). In this case, $\delta_c/\sigma(M) \gg 1$. We can use the next approximate expression,

$$\frac{1}{\sqrt{2\pi}} \int_{\bar{\beta}}^{\infty} e^{-\frac{x^2}{2}} dx \sim \frac{1}{\sqrt{2\pi}} e^{-\frac{\bar{\beta}^2}{2}} \frac{1}{\bar{\beta}} \quad (\text{A.39})$$

So, the ratio becomes

$$\begin{aligned} \frac{d}{dM} \left\{ \frac{f}{g} \right\} / \frac{2df}{dM} &= \frac{d}{d\nu} \left\{ \frac{f}{g} \right\} / \frac{2df}{d\nu} \\ &= \frac{1}{2} \sqrt{2\pi} (1-\bar{\alpha}) \{1 - (1-\bar{\alpha})^2\} \nu \exp\left\{ \frac{1}{2} \nu^2 (1-\bar{\alpha})^2 \right\}, \end{aligned} \quad (\text{A.40})$$

where $\nu \equiv \delta_c/\sigma = (M/M_*)^{\frac{(3+n)}{6}} \delta_c$.

from the above equations (37) and (39), the modified mass function is given as follows:

$$\begin{aligned} n(M) &= \frac{\bar{\rho}}{M} \left| \frac{d}{dM} \left\{ \frac{f}{g} \right\} \right| \\ &\sim \begin{cases} \bar{\alpha} n_{ps}. & (M \ll M_*) \\ \frac{\sqrt{2\pi}}{2} \bar{\alpha} (1-\bar{\alpha}) (2-\bar{\alpha}) \left(\frac{M}{M_*} \right)^{\frac{3+n}{6}} \delta_c \exp\left\{ \frac{1}{2} \left(\frac{M}{M_*} \right)^{\frac{3+n}{3}} \delta_c^2 (1-\bar{\alpha})^2 \right\} n_{ps}. & (M \gg M_*) \end{cases} \end{aligned} \quad (\text{A.41})$$

As we can see, the deviation from the PS mass function n_{ps} is no more than a factor $\bar{\alpha}$ on smaller mass scales $M \ll M_*$. However, on larger mass scale ranges in which mass function $M \gg M_*$, we find large deviations from the PS mass function. This estimated mass

function is in agreement with the numerically estimated one shown in Fig.A.1 and Fig.A.2. Therefore we can conclude that the above procedure of the approximation is good. However the condition that $\bar{\alpha}$ is independent of mass scale M in deriving eq.(A.40) is broken for very large mass scales ($M > 100M_*$). In this case, it is found that the mass function approaches the Press-Schechter mass function.

Here it must be noted that the characteristic mass M_* increases with time. At the present epoch M_* is around $10^{14}M_\odot$.

A.4 PEAK CONDITION

In the previous section, we showed how the effect of the spatial correlation alters the PS mass function. Strictly speaking, the conditional probability $P(M_1, M_2)$ shown in Section A.4 is not sufficient to obtain the *exact* mass function. Indeed, an *isolated* object of mass scale M_2 must have the *maximum peak density* with $\delta_{M_2} = \delta_c$ at $r = 0$. So we need to consider the conditional probability of finding a region of mass scale M_1 that is overdense by δ_c , or more, at distance r , provided that the object of mass scale M_1 is included in an *isolated* object of mass scale M_2 with the *maximum peak density* of $\delta_{M_2} = \delta_c$ at $r = 0$. Then we must use the following constrained probability,

$$\begin{aligned} P(r, M_1, M_2|\text{peak}) &= P(\delta_{M_1} > \delta_c | \delta_{M_2}, \text{peak}) \\ &= \sqrt{\frac{1 - \gamma^2}{2\pi(1 - \varepsilon^2 - \mu^2 - \gamma^2 + 2\varepsilon\mu\gamma)}} \frac{\int_0^\infty dx f(x) \int_{\nu_{1c}}^\infty d\nu_1 e^{-\frac{(Q_a + Q_b)}{2}}}{\int_0^\infty dx f(x) e^{-\frac{Q_b}{2}}}. \end{aligned} \quad (\text{A.42})$$

The detailed derivation of the above probability and notations are explained in Appendix A. Thus, we obtain the conditional probability $P(M_1, M_2|\text{peak})$ after averaging spatially the above probability,

$$P(M_1, M_2|\text{peak}) = \int_0^R P(r, M_1, M_2|\text{peak}) 4\pi r^2 dr / \int_0^R 4\pi r^2 dr. \quad (\text{A.43})$$

This is the new procedure to determine the mass function taking into consideration the more exact condition that an *isolated* object has a maximum peak density.

In Fig.A.3 and Fig.A.4, we show the mass function estimated numerically from eq.(A.42) for $n = 0$ and $n = -2$, respectively. For comparison, the PS mass function is shown also in both figures. We can clearly see the difference between both mass functions on small and large scales. We find that the deviation is within a factor of a few on smaller mass scales (e.g., a factor of 7 on $10^{-4}M_*$), and very large on larger mass scales. The deviation is almost similar to that shown in Section A.4 [eq.(A.40)] on large scales although on small scales the slopes of the mass functions are different from each other.

Now we investigate the probability that collapsed objects would overlap. If the overlap occurs, we can not account for the real number of the objects because we can not determine whether the overlapped objects merge to one larger mass object or fragment into two small objects in our statistical argument. In this case it is necessary to analyze dynamically the effect of the overlap. As shown in Appendix B, we find that the probability of the overlap can be neglected on very small mass scales ($M \ll M_*$) and very large ones ($M \gg M_*$) while it can not

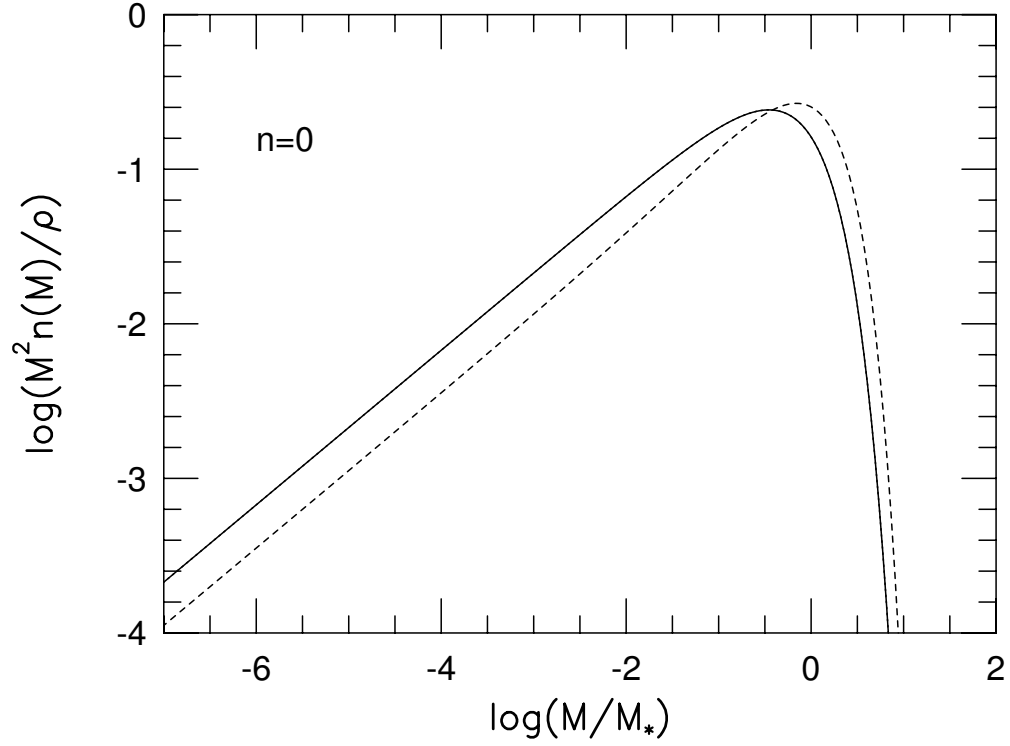


Fig.1

Figure A.1: The normalized mass function, which is estimated numerically including the effect of the spatial correlation, is shown by the solid line in the case of the power index $n = 0$. Dotted line represents the PS mass function.

be neglected on the medium mass scales. For example, the probability of an effective overlap is greater than 0.1 on the mass range between $0.1M_*$ and $10M_*$, when the power spectrum index n is 0.

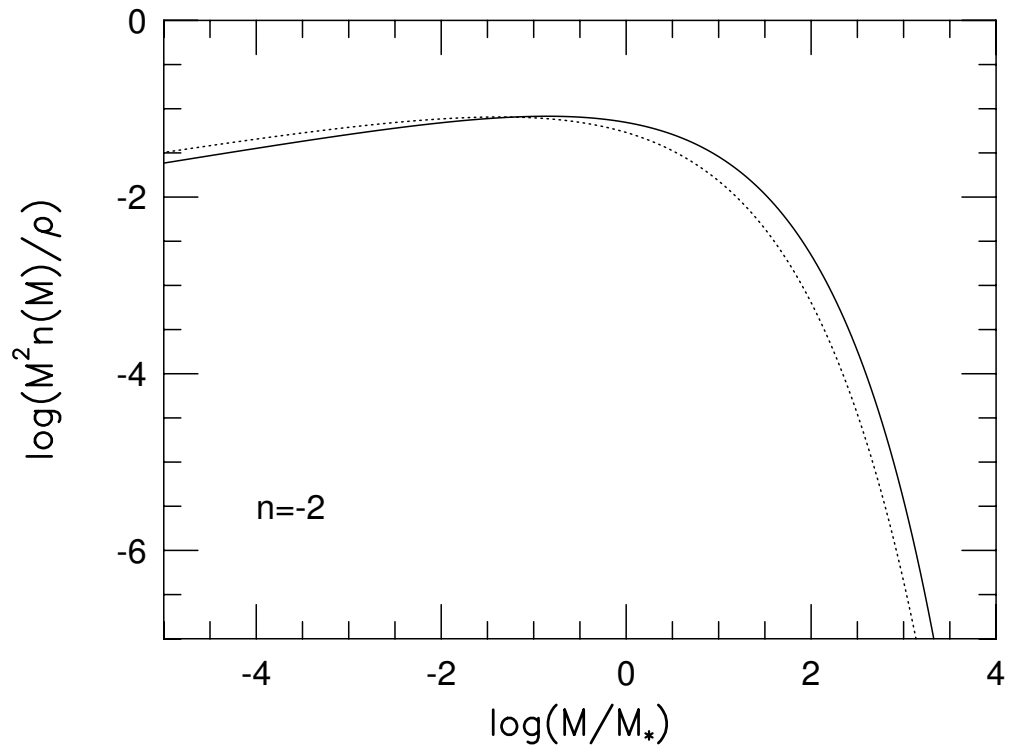


Fig.2

Figure A.2: Same as Fig.A.1, but for $n = -2$.

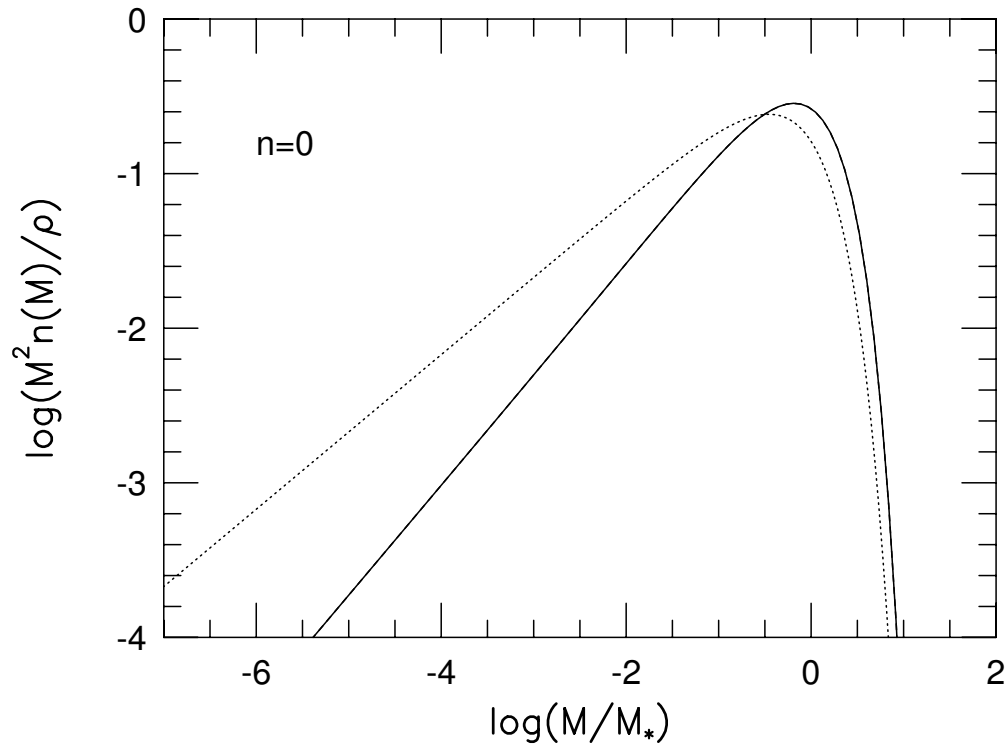


Fig.3

Figure A.3: The normalized mass function, which is estimated numerically by taking into account the additional necessary condition that *isolated* objects should have maximum peak density, is shown by the solid line in the case of the power index $n = 0$. Dotted line represents the PS mass function.

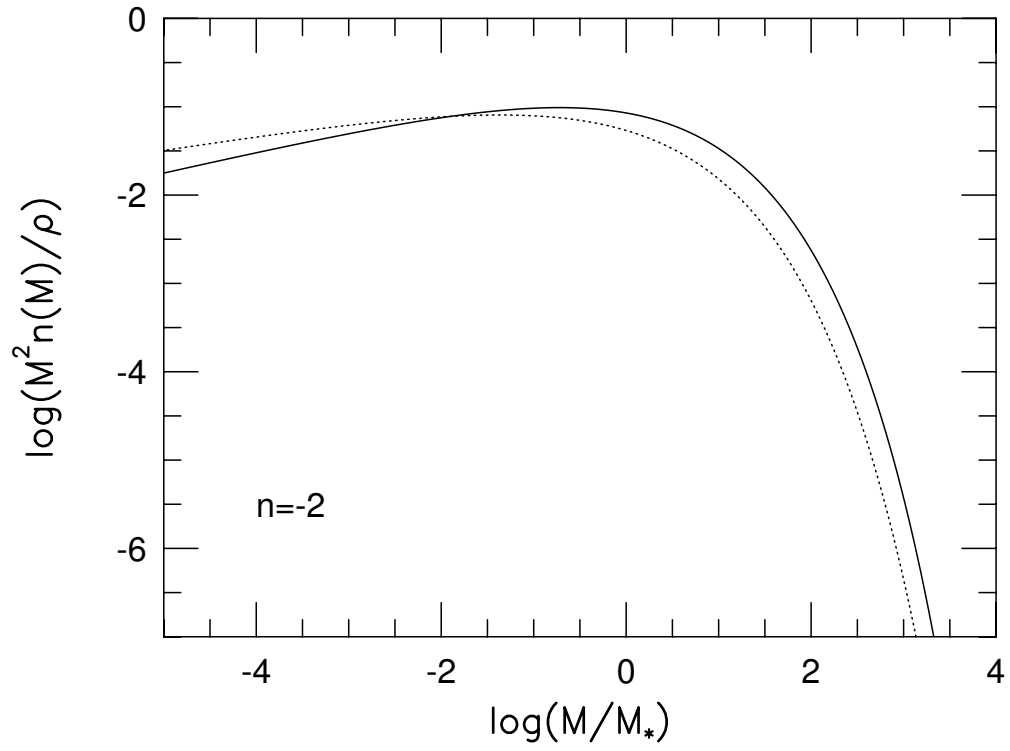


Fig.4

Figure A.4: Same as Fig.A.3, but for $n = -2$.

Appendix B

Mass function of block model

As mentioned in Section 2.3, we show the analytic formula which reproduces the mass functions given by the Block model.

The analytic formula is approximately expressed as follows. In YNG and PS, it is assumed that the density contrast δ_{M_2} of the isolated object which has collapsed with mass M_2 is just $\delta_c = 1.69$ (see eq.(2.13)). In the Block model, however, this condition should be changed to $\delta_{M_2} \geq \delta_c$ because in general we can not see the block which has just collapsed and its density contrast is just δ_c due to the discreteness of the mass scales of the blocks with $M_{i+1} = M_i/2$ in the Block model.

So the probability should be changed as follows:

$$\begin{aligned} P(M_1, M_2) &= p(\delta_{M_1} \geq \delta_c | \delta_{M_2} \geq \delta_c) \\ &= \frac{p(\delta_{M_1} \geq \delta_c, \delta_{M_2} \geq \delta_c)}{p(\delta_{M_2} \geq \delta_c)}. \end{aligned} \quad (\text{B.1})$$

In order to estimate the probability on the right hand side of eq.(B.1), we have to consider the two-variables Gaussian distribution function. The probability of m -variables Gaussian is generally (see BBKS)

$$p(\mathbf{V})d\mathbf{V} = \frac{\exp(-Q/2)}{\sqrt{(2\pi)^m \det(\mathbf{M})}} d\mathbf{V}, \quad (\text{B.2})$$

where

$$Q = \mathbf{V}\mathbf{M}^{-1}\mathbf{V}^T, \quad (\text{B.3})$$

$$\mathbf{V} = (y_1, y_2, \dots, y_m), \quad (\text{B.4})$$

$$M_{ij} = \langle (y_i - \langle y_i \rangle)(y_j - \langle y_j \rangle) \rangle \quad (\text{B.5})$$

and $y_i (i = 1, 2, \dots, m)$ is the Gaussian random variables. We use the angle brackets $\langle \rangle$ as the ensemble average of the universe, but in practice, assuming homogeneity and ergodicity in space, we can take it as the spatial average. So $\langle y_i \rangle$ corresponds to the spatial average of y_i , and M_{ij} is covariance between y_i and y_j . In this case, we may consider the two variables, δ_{M_1} and δ_{M_2} , so the covariance matrix \mathbf{M} is written as follows:

$$\mathbf{M} = \begin{pmatrix} \langle \delta_{M_1}^2 \rangle & \langle \delta_{M_1} \delta_{M_2} \rangle \\ \langle \delta_{M_1} \delta_{M_2} \rangle & \langle \delta_{M_2}^2 \rangle \end{pmatrix}. \quad (\text{B.6})$$

Note that $\langle \delta_{M_1}^2 \rangle$ and $\langle \delta_{M_2}^2 \rangle$ are variances, $\sigma^2(M_1)$ and $\sigma^2(M_2)$, respectively, and $\langle \delta_{M_1} \delta_{M_2} \rangle$ is a cross correlation at the same point.

Here, we normalize the density contrast and the cross correlation,

$$\nu_i \equiv \frac{\delta_{M_i}}{\sigma(M_i)}, \quad \epsilon \equiv \frac{\sigma_h^2}{\sigma(M_1)\sigma(M_2)}, \quad \sigma_h^2 \equiv \langle \delta_{M_1} \delta_{M_2} \rangle. \quad (\text{B.7})$$

Using the above notation, we obtain the two variables Gaussian distribution function,

$$p(\nu_1, \nu_2) d\nu_1 d\nu_2 = \frac{1}{2\pi\sqrt{1-\epsilon^2}} \exp\left(-\frac{(\nu_1 - \epsilon\nu_2)^2}{2(1-\epsilon^2)} - \frac{\nu_2^2}{2}\right) d\nu_1 d\nu_2. \quad (\text{B.8})$$

So we obtain

$$\begin{aligned} p(\delta_{M_1} \geq \delta_c, \delta_{M_2} \geq \delta_c) &= p(\nu_1 \geq \nu_{1c}, \nu_2 \geq \nu_{2c}) \\ &= \frac{1}{2\pi\sqrt{1-\epsilon^2}} \\ &\quad \times \int_{\nu_{1c}}^{\infty} \int_{\nu_{2c}}^{\infty} \exp\left(-\frac{(\nu_1 - \epsilon\nu_2)^2}{2(1-\epsilon^2)} - \frac{\nu_2^2}{2}\right) d\nu_1 d\nu_2, \end{aligned} \quad (\text{B.9})$$

where ν_{ic} is $\delta_c/\sigma(M_i)$. Furthermore, dividing the above equation by the integration of one variable Gaussian distribution,

$$\begin{aligned} p(\delta_{M_2} \geq \delta_c) &= p(\nu_2 \geq \nu_{2c}) \\ &= \frac{1}{\sqrt{2\pi}} \int_{\nu_{2c}}^{\infty} \exp\left(-\frac{\nu_2^2}{2}\right) d\nu_2, \end{aligned} \quad (\text{B.10})$$

we obtain the $P(M_1, M_2)$.

Next, we estimate the normalized cross correlation function ϵ . In eqs.(2.12) and (2.14), the variance σ_i with the mass M_i is given by

$$\sigma_i^2 = \frac{4\pi V}{(2\pi)^3} \int_0^{\infty} W_i^2(k) P(k) k^2 dk, \quad (\text{B.11})$$

and the variance of the additional density contrast Σ is given by

$$\Sigma_i^2 = \sigma_i^2 - \sigma_{i-1}^2, \quad i \geq 1. \quad (\text{B.12})$$

Because we give the additional density contrast independently of another density contrast with the other mass scale, the variance of the additional density contrast must depend on the power spectrum only at the interval of the wavenumber $[k_{i+1}, k_i]$, corresponding to the mass scales $[M_i, M_{i+1}]$. So we should adopt the sharp- k space filter as the window function $W_i(k)$ defined by,

$$W_i(k) = \begin{cases} 1, & k \leq k_c(M_i) \\ 0, & k > k_c(M_i), \end{cases} \quad (\text{B.13})$$

In this case, the variance and the cross correlation are

$$\sigma_i^2 = \frac{4\pi V}{(2\pi)^3} \int_0^{k_i} P(k) k^2 dk, \quad (\text{B.14})$$

$$\begin{aligned} \sigma_h^2 &= \frac{4\pi V}{(2\pi)^3} \int_0^\infty W_1(k) W_2(k) P(k) k^2 dk \\ &= \frac{4\pi V}{(2\pi)^3} \int_0^{k_2} P(k) k^2 dk \\ &= \sigma_2^2 \end{aligned} \quad (\text{B.15})$$

where $i = 1, 2$ and $M_1 \leq M_2$, *i.e.*, $k_1 \geq k_2$. So the normalized cross correlation function ϵ is

$$\epsilon = \frac{\sigma_h^2}{\sigma_1 \sigma_2} = \frac{\sigma_2}{\sigma_1}. \quad (\text{B.16})$$

Substituting the above eq.(B.16) into eq.(B.9), we obtain

$$\begin{aligned} p(\delta_{M_1} \geq \delta_c, \delta_{M_2} \geq \delta_c) &= \frac{1}{2\pi\sigma_2\sigma_{\text{sub}}} \\ &\times \int_{\delta_c}^\infty \int_{\delta_c}^\infty \exp\left(-\frac{(\delta_1 - \delta_2)^2}{2\sigma_{\text{sub}}^2} - \frac{\delta_2^2}{2\sigma_2^2}\right) d\delta_1 d\delta_2, \end{aligned} \quad (\text{B.17})$$

where

$$\sigma_{\text{sub}}^2 = \sigma_1^2 - \sigma_2^2. \quad (\text{B.18})$$

Therefore the conditional probability $P(M_1, M_2)$ is

$$\begin{aligned} P(M_1, M_2) &= N^{-1} \frac{1}{2\pi\sigma_2\sigma_{\text{sub}}} \\ &\times \int_{\delta_c}^\infty \int_{\delta_c}^\infty \exp\left(-\frac{(\delta_1 - \delta_2)^2}{2\sigma_{\text{sub}}^2} - \frac{\delta_2^2}{2\sigma_2^2}\right) d\delta_1 d\delta_2, \end{aligned} \quad (\text{B.19})$$

where

$$N = \frac{1}{\sqrt{2\pi}\sigma_2} \int_{\delta_c}^\infty \exp\left(-\frac{\delta_2^2}{2\sigma_2^2}\right) d\delta_2. \quad (\text{B.20})$$

Note that this probability is the same as eq.(8) in Jedamzik (1995).

Appendix C

Formalism of mass function

C.1 CONDITIONAL PROBABILITY DISTRIBUTION FUNCTION

In Section A.5, we mentioned a new formula for the mass function. Here, we express the conditional probability on which the formula is based.

To determine the probability that an object of mass scale M_2 is isolated and includes objects of mass scale M_1 which have collapsed, the following necessary conditions have to be taken into account;

- 1) The density contrast of mass scale M_2 , δ_2 , should be equal to $\delta_c = 1.69$ at the center of the object.
- 2) Objects of mass scale M_2 must have a maximum peak of the density field, *i.e.*, the first derivative of the density contrast $\nabla\delta_2$ must equal 0 and each diagonal component of the diagonalized Hessian matrix ζ of the second derivatives must be less than 0 at the center of the object.
- 3) The density contrast of mass scale $M_1 (\leq M_2)$ which collapsed and is included in an object of mass scale M_2 must satisfy the condition $\delta_1 \geq \delta_c$ at distance r from the center of the larger object.

Therefore, the desired probability is expressed in terms of Bayes's theorem,

$$P(\delta_1(r) \geq \delta_c | \delta_2 = \delta_c, \text{peak}) = \frac{P(\delta_1(r) \geq \delta_c, \delta_2 = \delta_c, \text{peak})}{P(\delta_2 = \delta_c, \text{peak})} \quad (\text{C.1})$$

In order to estimate the probabilities on right hand side of eq.(C.1), we have to consider the multivariate Gaussian distribution function composed of variables $\mathbf{V}_1 \equiv (\delta_1(r), \delta_2, \eta_i, \zeta_{ij})$ and $\mathbf{V}_2 \equiv (\delta_2, \eta_i, \zeta_{ij})$ where $\eta_i \equiv \nabla_i \delta_2$, $\zeta_{ij} \equiv \nabla_i \nabla_j \delta_2$, ∇ meaning the spatial derivative and $i, j = 1, 2, 3$. The *maximum peak* means that the first derivative of the density contrast $\nabla\delta_2$ equals 0 and each diagonal component of the diagonalized Hessian matrix ζ composed of the second derivatives is less than 0 at the center of the object. The Gaussian distribution for m -variables is in general (see BBKS)

$$P(\mathbf{V})d\mathbf{V} = \frac{e^{(-\frac{Q}{2})}}{\sqrt{(2\pi)^m \det(\mathbf{M})}} d\mathbf{V}, \quad (\text{C.2})$$

where

$$Q = \mathbf{V}\mathbf{M}^{-1}\mathbf{V}^T \quad (\text{C.3})$$

$$\mathbf{V} = (y_1, \dots, y_m) \quad (\text{C.4})$$

$$M_{ij} = \langle (y_i - \langle y_i \rangle)(y_j - \langle y_j \rangle) \rangle. \quad (\text{C.5})$$

where $y_i (i = 1, 2, \dots, m)$ are the Gaussian random variables. We use the angle brackets $\langle \rangle$ as the ensemble mean of the universe, but in practice, assuming homogeneity and ergodicity in space, we take it as the spatial mean, so $\langle y_i \rangle$ corresponds to the spatial mean of y_i and M_{ij} is the covariance between y_i and y_j . The correlations between the variables are

$$\begin{aligned} \langle \delta_1(r)\delta_1(r) \rangle &= \sigma_r^2, & \langle \delta_2\delta_2 \rangle &= \sigma_0^2, & \langle \delta_1(r)\delta_2 \rangle &= \sigma_{0r}^2, \\ \langle \eta_i\eta_j \rangle &= \frac{\sigma_1^2}{3}\delta_{ij}, & \langle \zeta_{ij}\zeta_{kl} \rangle &= \frac{\sigma_2^2}{15}(\delta_{ij}\delta_{kl} + \delta_{ik}\delta_{jl} + \delta_{il}\delta_{jk}), \\ \langle \delta_2\zeta_{ij} \rangle &= -\frac{\sigma_1^2}{3}\delta_{ij}, & \langle \delta_1(r)\zeta_{ij} \rangle &= -\frac{\sigma_{1r}^2}{3}\delta_{ij}, \end{aligned} \quad (\text{C.6})$$

where

$$\begin{aligned} \sigma_l^2 &= \frac{4\pi V}{(2\pi)^3} \int_0^\infty W^2(k, R_2) |\delta_k|^2 k^{(2l+2)} dk \\ \sigma_{lr}^2 &= \frac{4\pi V}{(2\pi)^3} \int_0^\infty W(k, R_1) W(k, R_2) |\delta_k|^2 k^{(2l+2)} \frac{\sin(kr)}{kr} dk \\ \sigma_r^2 &= \frac{4\pi V}{(2\pi)^3} \int_0^\infty W^2(k, R_1) |\delta_k|^2 k^2 dk, \end{aligned} \quad (\text{C.7})$$

and $W(k, R)$ is a window function. Throughout this paper, we use the sharp k -space filter;

$$W(k, R) = \begin{cases} 1 & [k \leq k_c(R)] \\ 0 & [k > k_c(R)], \end{cases} \quad (\text{C.8})$$

Here, we diagonalize the second derivatives ζ_{ij} for convenience. The Hesse matrix ζ_{ij} is diagonalized by introducing the eigenvalues $(-\lambda_1, -\lambda_2, -\lambda_3)$, using a rotation (*see* the Appendixes A and B in BBKS). Therefore, the volume element becomes

$$d\text{vol} = \prod_{\substack{i,j=1,2,3 \\ i \leq j}} d\zeta_{ij} = |(\lambda_1 - \lambda_2)(\lambda_2 - \lambda_3)(\lambda_1 - \lambda_3)| d\lambda_1 d\lambda_2 d\lambda_3 d\text{vol}[SO(3)], \quad (\text{C.9})$$

where

$$d\text{vol}[SO(3)] = \sin \beta' d\beta' d\alpha' d\gamma', \quad (\text{C.10})$$

and α', β' , and γ' are the Euler angles.

Next, we normalize the variables:

$$\begin{aligned} \nu_1 &= \delta_1(r)/\sigma_r, & \nu_2 &= \delta_2/\sigma_0, \\ x &= (\lambda_1 + \lambda_2 + \lambda_3)/\sigma_2, & y &= (\lambda_1 - \lambda_3)/2\sigma_2, & z &= (\lambda_1 - 2\lambda_2 + \lambda_3)/2\sigma_2. \end{aligned} \quad (\text{C.11})$$

Note that the peak condition is equivalent to $\vec{\eta} = 0$ and $\lambda_1, \lambda_2, \lambda_3 \geq 0$. So the correlations are transformed to

$$\begin{aligned} \langle \nu_1 \nu_1 \rangle &= 1, & \langle \nu_2 \nu_2 \rangle &= 1, & \langle x \nu_2 \rangle &= \gamma, \\ \langle \nu_1 \nu_2 \rangle &= \varepsilon(r), & \langle x \nu_1 \rangle &= \mu(r), & \langle x^2 \rangle &= 1, \\ \langle y^2 \rangle &= 1/15, & \langle z^2 \rangle &= 1/5. \end{aligned} \quad (\text{C.12})$$

Here we define the following variables;

$$\begin{aligned} Q_a &= \frac{1 - \gamma^2}{1 - \varepsilon^2 - \mu^2 - \gamma^2 + 2\varepsilon\mu\gamma} \left[\nu_1 + \frac{\mu\gamma - \varepsilon}{1 - \gamma^2} \nu_2 + \frac{\varepsilon\gamma - \mu}{1 - \gamma^2} x \right]^2, \\ Q_b &= \frac{(x - \gamma\nu_2)^2}{1 - \gamma^2}, \quad Q_c = \nu_2^2 + 15y^2 + 5z^2 + 3 \sum_{i=1}^3 \frac{\eta_i^2}{\sigma_1^2} \\ Q_d &= \frac{15}{\sigma_2^2} (\zeta_{12} + \zeta_{23} + \zeta_{31}). \end{aligned} \quad (C.13)$$

Then we obtain

$$P(\nu_2, \eta, x, y, z) d\nu_2 d^3\eta dx dy dz = \frac{3(15)^{5/2} |y(y^2 - z^2)|}{8\pi^3 \sigma_1^3 \sqrt{1 - \gamma^2}} e^{-\frac{(Q_b + Q_c)}{2}} d\nu_2 d^3\eta dx dy dz, \quad (C.14)$$

$$\begin{aligned} &P(\nu_1, \nu_2, \eta, x, y, z) d\nu_1 d\nu_2 d^3\eta dx dy dz \\ &= \frac{3(15)^{5/2} |y(y^2 - z^2)| e^{-\frac{(Q_a + Q_b + Q_c)}{2}}}{8\sqrt{2}\pi^{7/2} \sigma_1^3 \sqrt{1 - \varepsilon^2 - \mu^2 - \gamma^2 + 2\varepsilon\mu\gamma}} d\nu_1 d\nu_2 d^3\eta dx dy dz. \end{aligned} \quad (C.15)$$

And we can impose the order $\lambda_1 \geq \lambda_2 \geq \lambda_3$, then $-y \leq z \leq y, y \geq 0$. So we obtain the conditional probability from the Bayes's theorem as follows;

$$\begin{aligned} &P(r, M_1, M_2 | \text{peak}) \\ &= \frac{\int_{\nu_{1c}}^{\infty} d\nu_1 \int_0^{\infty} dx \{ \int_0^{x/4} dy \int_{-y}^y dz |y(y^2 - z^2)| \exp(-\frac{15}{2}y^2 - \frac{5}{2}z^2) \\ &\quad + \int_{x/4}^{x/2} dy \int_{3y-x}^y dz |y(y^2 - z^2)| \exp(-\frac{15}{2}y^2 - \frac{5}{2}z^2) \} P(\nu_1, \nu_2 = \nu_{2c}, \vec{\eta} = 0, x, y, z)}{\int_0^{\infty} dx \{ \int_0^{x/4} dy \int_{-y}^y dz |y(y^2 - z^2)| \exp(-\frac{15}{2}y^2 - \frac{5}{2}z^2) \\ &\quad + \int_{x/4}^{x/2} dy \int_{3y-x}^y dz |y(y^2 - z^2)| \exp(-\frac{15}{2}y^2 - \frac{5}{2}z^2) \} P(\nu_2 = \nu_{2c}, \vec{\eta} = 0, x, y, z)} \\ &= \sqrt{\frac{1 - \gamma^2}{2\pi(1 - \varepsilon^2 - \mu^2 - \gamma^2 + 2\varepsilon\mu\gamma)}} \frac{\int_0^{\infty} dx f(x) \int_{\nu_{1c}}^{\infty} d\nu_1 e^{-\frac{(Q_a + Q_b)}{2}}}{\int_0^{\infty} dx f(x) e^{-\frac{Q_b}{2}}}. \end{aligned} \quad (C.16)$$

Here

$$\begin{aligned} f(x) &\equiv \int_0^{x/4} dy \int_{-y}^y dz |y(y^2 - z^2)| \exp(-\frac{15}{2}y^2 - \frac{5}{2}z^2) \\ &\quad + \int_{x/4}^{x/2} dy \int_{3y-x}^y dz |y(y^2 - z^2)| \exp(-\frac{15}{2}y^2 - \frac{5}{2}z^2). \end{aligned} \quad (C.17)$$

Thus, we determine $P(M_1, M_2 | \text{peak})$ using the eq.(A.29):

$$P(M_1, M_2 | \text{peak}) = \int_0^R P(r, M_1, M_2 | \text{peak}) 4\pi r^2 dr / \int_0^R 4\pi r^2 dr. \quad (C.18)$$

Strictly speaking, we have to consider the additional condition that an isolated object of mass M_2 is not included in an object of larger mass $M_3 (> M_2)$ in the neighborhood. This probability is written, using Bayes's theorem,

$$\begin{aligned} &P(\nu_1 \geq \nu_{1c} | \nu_2 = \nu_{2c}, \vec{\eta} = 0, \lambda_1 \geq \lambda_2 \geq \lambda_3 \geq 0, \nu_{M_3 \geq M_2}(r \leq R_3) < \nu_{3c}) \\ &= \frac{P(\nu_1 \geq \nu_{1c}, \nu_2 = \nu_{2c}, \vec{\eta} = 0, \lambda_1 \geq \lambda_2 \geq \lambda_3 \geq 0, \nu_{M_3 \geq M_2}(r \leq R_3) < \nu_{3c})}{P(\nu_2 = \nu_{2c}, \vec{\eta} = 0, \lambda_1 \geq \lambda_2 \geq \lambda_3 \geq 0, \nu_{M_3 \geq M_2}(r \leq R_3) < \nu_{3c})}. \end{aligned} \quad (C.19)$$

In this case, however, it is very difficult to compute the mass function numerically.

C.2 OVERLAPPING EFFECT

In this section, we consider the effect of the overlap between collapsed objects.

As we said before, the deviation of the mass function, which is estimated by taking into consideration the more restricted probability that the isolated object has the maximum peak density, from the PS mass function, has almost the same feature as in the case in which we consider only the effect of the spatial correlation. Then here for simplicity we roughly analyze the overlap probability by considering only the effect of the spatial correlation.

Let us assume that there is an isolated collapsed object of mass scale M_2 that is overdense by just δ_c . If an isolated object of the mass scale $M_1 (\leq M_2)$ is located at $R_2 - R_1 \lesssim r \lesssim R_2 + R_1$, the overlap between the objects of mass M_2 and M_1 would occur.

Now we consider the condition that the object of mass scale M_1 , whose scale is between mass scale 0 and M_2 , has the critical overdensity at $R_2 - R_1 \lesssim r \lesssim R_2 + R_1$, in other words, we imagine an object of mass scale M_1 overlapping the object of mass scale M_2 . So we consider the following conditional probability of finding a region of mass scale between 0 and M_2 that is overdense by just δ_c at $R_2 - R_1 \lesssim r \lesssim R_2 + R_1$, which is the distance from the center of the isolated object of mass scale M_2 .

$$\begin{aligned}
 P_{\text{overlap}}(r, \delta = \delta_c, 0 < M < M_2) \\
 &= \{P(R_2 - R_1 \lesssim r \lesssim R_2 + R_1, 0, M_2) - P(R_2 - R_1 \lesssim r \lesssim R_2 + R_1, M_2, M_2)\} \\
 &\quad / \{1 - P(R_2 - R_1 \lesssim r \lesssim R_2 + R_1, M_2, M_2)\} \\
 &\sim \frac{\int_0^{\beta(M_2, r)} e^{-\frac{y^2}{2}} dy}{\int_{-\infty}^{\beta(M_2, r)} e^{-\frac{y^2}{2}} dy},
 \end{aligned} \tag{C.20}$$

where

$$P(R_2 - R_1 \lesssim r \lesssim R_2 + R_1, M_1, M_2) = \int_{\beta(M_1, r)}^{\infty} e^{-\frac{y^2}{2}} dy, \tag{C.21}$$

$$\beta(M_1, r) \equiv \frac{\delta_c}{\sigma(M_1)}(1 - \alpha(r)), \tag{C.22}$$

$$R_2 - R_1 < r < R_2 + R_1. \tag{C.23}$$

When the mass scale M_2 is much smaller than the characteristic mass scale M_* , both conditional probability $P(R_2 - R_1 \lesssim r \lesssim R_2 + R_1, 0, M_2)$ and $P(R_2 - R_1 \lesssim r \lesssim R_2 + R_1, M_2, M_2)$ can be nearly equal to $\frac{1}{2}$ because both $\sigma(M_1)$ and $\sigma(M_2)$ are much larger than unity (for the hierarchical clustering $n > -3$) and then $\beta(M_1, r)$ and $\beta(M_2, r)$ are nearly equal to 0 in each case. So the probability $P_{\text{overlap}}(r, \delta_c, 0 < M < M_2)$ can be neglected for very small mass scales. For example, the probability is less than 0.1 for the case in which M is less than $0.1M_*$ and the power spectrum index n is 0.

On the other hand, as for the mass scale such that M_2 is not much smaller than M_* , the probability of overlap might not be neglected. However, objects of much smaller mass $M_1 (\ll M_2)$ contribute dominantly to the overlap with the object of mass M_2 as we can see from the above probability. So the mass of the object of mass scale $M_2 (\gg M_*)$ is not changed so much by the overlap with objects of such small mass scales. Hence, as for the very large

mass scale M_2 , the mass function of M_2 itself might not be affected much by the effect of overlap. For example, the probability that the mass function is effectively changed by taking into account the effect of the overlap is less than 0.1 for cases in which M_2 is larger than $10M_*$ and the power index n is 0. Then we can conclude that the effect of the overlap might create a serious problem for estimating the mass function on medium mass ($0.1M_* \lesssim M \lesssim 10M_*$) scales.

Bibliography

- [1] Arimoto N., Yoshii Y., 1986, A&A, 164, 260
- [2] Arimoto N., Yoshii Y., 1987, A&A, 173, 23
- [3] Arimoto N., Yoshii Y., Takahara F., 1991, A&A, 253, 21
- [4] Babul A., Rees, M.J., 1992, MNRAS, 255, 346
- [5] Bajtlik S., Duncan R.C., Ostriker J.P., 1988, ApJ, 327, 570
- [6] Bardeen J.M., Bond J.R., Kaiser N., Szalay A.S., 1986, ApJ, 304, 15(BBKS)
- [7] Baugh C.M., Cole S., Frenk C.S., 1996, MNRAS, 283, 1361
- [8] Bechtold J., 1994, ApJS, 91, 1
- [9] Binney J., Tremaine S., 1987, Galactic Dynamics, Princeton Univ. Press, Princeton, NJ
- [10] Bond J.R., Cole S., Efstathiou G., Kaiser N., 1991, ApJ, 379, 440
- [11] Bower R.G., 1991, MNRAS, 248, 332
- [12] Bower R.G., Lucey J.R., Ellis R.S., 1992, MNRAS, 254, 601
- [13] Bruzual G., Charlot S., 1996, in preparation
- [14] Carswell R.F., Morton D.C., Smith M.G., Stockton A.N., Turnshek D.A., Weymann R.J., 1984, ApJ, 278, 486
- [15] Chiba M., Nath B.B., 1994, ApJ, 436, 618
- [16] Cole S., 1991, ApJ, 367, 45
- [17] Cole S., Kaiser N., 1988, MNRAS, 233, 637
- [18] Cole S., Aragon-Salamanca A., Frenk C.S., Navarro J.F., Zepf S.E., 1994, MNRAS, 271, 781
- [19] Dekel A., Rees M.J., 1987, Nat, 326, 455
- [20] Dressler A., 1980, ApJ, 236, 351

- [21] Efstathiou G., 1992, MNRAS, 256, 43P
- [22] Ellis, R.S., 1997, ARA&A, 35, 389
- [23] Epstein R.I., 1983, MNRAS, 205, 207
- [24] Fabian A.C., 1994, ARA&A, 32, 227
- [25] Fujita Y., 1998, ApJ, in press
- [26] Fujita Y., Nagashima M., 1998, ApJ, in press
- [27] Giallongo E., Cristiani S., D’Odorico S., Fontana A., Savaglio S., 1996, ApJ, 466, 46
- [28] Gunn J.E., Gott J.R., 1972, ApJ, 176, 1
- [29] Gunn J.E., Peterson B.A., 1965, ApJ, 142, 1633
- [30] Gurbatov S.N., Saichev A.I., Shandarin S.F., 1989, MNRAS, 236, 385
- [31] Jeans J.H., 1922, MNRAS, 82, 122
- [32] Jedamzik K., 1995, ApJ, 448, 1
- [33] Kang H., Ostriker J.P., Cen R., Ryu D., Hernquist L., Evrard A.E., Bryan G.L., Norman M.L., 1994, ApJ, 430, 83
- [34] Kauffmann G., White S.D.M., 1993, MNRAS, 261, 921
- [35] Kauffmann G., White S.D.M., Guiderdoni, 1993, MNRAS, 264, 201
- [36] Kauffmann G., Charlot S., 1998, MNRAS, 294, 705(KC)
- [37] Kodama T., Arimoto N., 1997, A&A, 320, 41
- [38] Kulkarni V.P., Fall S.M., 1993, ApJ, 413, L63
- [39] Lacey C.G., Cole S., 1993, MNRAS, 262, 627
- [40] Lacey C.G., Silk J., 1991, ApJ, 381, 14
- [41] Lacey C.G., Silk J., 1993, ApJ, 402, 15
- [42] Larson R.B., 1974, MNRAS, 166, 585
- [43] Loveday J., Peterson B.A., Efstathiou G., Maddox S.J., 1992, ApJ, 90, 338
- [44] Lu L., Sargent W.L.W., Womble D.S., Takada-Hidai M., 1996, ApJ, 472, 509
- [45] Miller G.E., Scalo J.M., 1979, ApJS, 41, 513
- [46] Mobasher B., Ellis R.S., Sharples R.M., 1986, MNRAS, 223, 11

- [47] Mobasher B., Sharples R.M., Ellis R.S., 1993, MNRAS, 263, 560
- [48] Monaco P., 1998, Fundam. Cosmic Phys., in press
- [49] Nagashima M., Gouda N., 1997, MNRAS, 287, 515
- [50] Nagashima M., Gouda N., 1998, MNRAS, in press
- [51] Nagashima M., Gouda N., Sugiura N., preprint, astro-ph/9804153
- [52] Navarro J.F., White S.D.M., 1993, MNRAS, 265, 271
- [53] Peacock J.A., Heavens A.F., 1985, MNRAS, 217, 805
- [54] Peacock J.A., Heavens A.F., 1990, MNRAS, 243, 133
- [55] Peebles P.J.E., 1993, The Principles of Physical Cosmology. Princeton Univ. Press, Princeton
- [56] Pei Y.C., 1995, ApJ, 438, 623
- [57] Porciani C., Matarrese S., Lucchin F., Catelan P., 1998, MNRAS, 298, 1097
- [58] Press W.H., Schechter P., 1974, ApJ, 387, 47(PS)
- [59] Rees M.J., Ostriker J.P., 1977, MNRAS, 267, 1020
- [60] Rodrigues D.D.C., Thomas P.A., 1996, MNRAS, 282, 631
- [61] Roukema B.F., Peterson B.A., Quinn P.J., Rocca-Volmerange B., 1997, MNRAS, 292, 835
- [62] Salpeter E.E., 1955, ApJ, 121, 161
- [63] Scalo J.M., 1986, Fundam. Cosmic Phys., 11, 1
- [64] Simien F., de Vaucouleurs G., 1986, ApJ, 302, 564
- [65] Somerville R.S., Kolatt T., preprint, astro-ph/9711080
- [66] Somerville R.S., Primack J.R., preprint, astro-ph/9802268
- [67] Sutherland R., Dopita M.A., 1993, ApJS, 88, 253
- [68] Tajiri Y., Umemura M., 1998, ApJ, 502, 59
- [69] Tinsley B.M., 1980, Fundam. Cosmic Phys., 5, 287
- [70] Vergassola M., Dubrulle B., Frisch U., Noullez A., 1994, A&A, 289, 325
- [71] White S.D.M., Frenk C.S., 1991, ApJ, 379, 25
- [72] White S.D.M., Rees M.J., 1978, MNRAS, 183, 341

- [73] Whitmore B.C., Gilmore D.M., 1991, ApJ, 367, 64
- [74] Williger G.M., Baldwin J.A., Carswell R.F., Cooke A.J., Hazard C., Irwin M.J., McMahon R.G., Storrie-Lombardi L.J., 1994, ApJ, 428, 574
- [75] Yano T., Nagashima M., Gouda N., 1996, ApJ, 466, 1(YNG)